

Accretion Regimes of Neutrino-Cooled Flows onto Black Holes

JAVIERA HERNÁNDEZ-MORALES ¹ AND DANIEL M. SIEGEL ^{1,2}

¹*Institute of Physics, University of Greifswald, D-17489 Greifswald, Germany*

²*Department of Physics, University of Guelph, Guelph, ON, N1G 2W1, Canada*

ABSTRACT

Neutrino-cooled accretion disks can form in the aftermath of neutron-star mergers as well as during the collapse of rapidly rotating massive stars (collapsars) and the accretion-induced collapse of rapidly rotating white dwarfs. Due to Pauli blocking as electrons become degenerate at sufficiently high accretion rates \dot{M} , the resulting ‘self-neutronization’ of the dissociated accreting plasma makes these astrophysical systems promising sources of rapid neutron capture nucleosynthesis (the *r*-process). We present a one-dimensional general-relativistic, viscous-hydrodynamic model of neutrino-cooled accretion disks around black holes. With collapsars, super-collapsars and very massive star collapse in mind, we chart the composition of the accretion flow and systematically explore different radiatively efficient and inefficient accretion regimes with increasing \dot{M} , across a vast parameter space of $\dot{M} \sim 10^{-6} - 10^6 M_{\odot} \text{ s}^{-1}$, black hole masses of $M_{\bullet} \sim 1 - 10^4 M_{\odot}$ and dimensionless spins of $\chi_{\bullet} \in [0, 1)$, as well as α -viscosity values of $\alpha \sim 10^{-3} - 1$. We show that these accretion regimes are separated by characteristic thresholds \dot{M}_{char} that follow power laws $\dot{M}_{\text{char}} \propto M_{\bullet}^{\alpha} \alpha^{\beta}$ and that can be understood based on analytic approximations we derive. We find that outflows from such disks are promising sites of *r*-process nucleosynthesis up to $M_{\bullet} \lesssim 3000 M_{\odot}$. These give rise to lanthanide-bearing ‘red’ super-kilonovae transients mostly for $M_{\bullet} \lesssim 200 - 500 M_{\odot}$ and lanthanide suppressed ‘blue’ super-kilonovae for larger M_{\bullet} . Proton-rich outflows can develop specifically for large black hole masses ($M_{\bullet} \gtrsim 100 M_{\odot}$) in certain accretion regimes, which may give rise to proton-rich isotopes via the νp -process.

Keywords: Black holes (162) — Compact objects (288) — Nucleosynthesis (1131) — R-process (1324) — Stellar accretion disks (1579)

1. INTRODUCTION

The astrophysical origin of roughly half of the heavy elements heavier than iron, those synthesized by the rapid neutron-capture process (the *r*-process; A. G. W. Cameron 1957; E. M. Burbidge et al. 1957), represents an open, fundamental question in astrophysics and a topic of intense debate (see, e.g., C. J. Horowitz et al. 2019; J. J. Cowan et al. 2021; D. M. Siegel 2022; A. Arcones & F.-K. Thielemann 2022 for recent reviews). The detection of kilonovae (L.-X. Li & B. Paczyński 1998; B. D. Metzger et al. 2010; J. Barnes & D. Kasen 2013; B. D. Metzger 2020) from the gravitational-wave event GW170817 (B. P. Abbott et al. 2017) as well as from several gamma-ray bursts (GRBs; E. Berger et al. 2013; N. R. Tanvir et al. 2013; J. C. Rastinejad et al. 2025) establish neutron star mergers as a major if not dominant source of *r*-process elements in the Universe.

Observations of *r*-process enhanced metal-poor stars in ultra-faint dwarf galaxies and isotopic analyses of me-

teorites as well as of sediments in the deep sea crust show that the main *r*-process must originate in rare events relative to core-collapse supernovae with large *r*-process yields per event both in early (i.e. at low metallicity) and recent Galactic history (A. P. Ji et al. 2016; T. T. Hansen et al. 2017; T. Tsujimoto et al. 2017; P. Beniamini et al. 2016; A. Wallner et al. 2015; K. Hotokezaka et al. 2015). Systemic kicks of neutron star binaries, their (on average) large delay times relative to star formation with which they enrich the surrounding interstellar medium with nucleosynthesis products, as well as strong iron co-production of at least two supernovae per binary cast doubt on whether these are the dominant sources of *r*-process elements in low-metallicity environments, including (ultra-faint) dwarf galaxies and globular clusters (M. Bonetti et al. 2019; M. Zevin et al. 2019; Á. Skúladóttir et al. 2019; R. P. Naidu et al. 2022; J. D. Simon et al. 2023; E. N. Kirby et al. 2023). In particular, chemical evolution studies indicate that a high-rate, low-yield *r*-process source other than neutron-star

mergers must exist³, which acts at low metallicities at a major if not dominant level (F. Matteucci et al. 2014; B. Wehmeyer et al. 2015; D. M. Siegel 2019; B. Côté et al. 2019; F. van de Voort et al. 2020; C. Kobayashi et al. 2023; H.-Y. Chen et al. 2025), such as magnetorotational supernovae (T. A. Thompson et al. 2004; C. Winteler et al. 2012) or collapsars (D. M. Siegel et al. 2019; J. M. Miller et al. 2020; O. Just et al. 2022; D. Issa et al. 2025).

Accretion flows onto compact objects can reach sufficiently high temperatures $k_B T \gtrsim \text{MeV}$ at which nuclei become dissociated and electron or positron capture onto individual protons and neutrons become fast compared to the accretion timescale; thus, neutrino emission is ‘ignited’. Furthermore, at sufficiently high accretion rates (rest-mass densities of the flow), electrons and positrons become degenerate and positron capture onto neutrons is suppressed by Pauli blocking. Consequently, the flow self-neutronizes, leading to an electron/proton-fraction $Y_e < 0.5$ (A. M. Beloborodov 2003), a minimal requirement for r -process nucleosynthesis. Once in the degenerate regime, the flow maintains a high neutron richness ($Y_e \sim 0.1 - 0.2$) in a self-regulated process that maintains mild degeneracy $\eta_e = \mu_e/k_B T \sim 1$, where μ_e is the electron chemical potential (W.-X. Chen & A. M. Beloborodov 2007; D. M. Siegel & B. D. Metzger 2017). The minimum accretion rate \dot{M} for neutrino emission to balance viscous heating and the onset of degeneracy (the ‘ignition threshold’ \dot{M}_{ign}) is estimated to be $\sim 10^{-3} - 0.1 M_\odot \text{s}^{-1}$ for stellar-mass black holes, depending on the effective viscosity of the accretion flow and the black hole mass and spin (W.-X. Chen & A. M. Beloborodov 2007; S. De & D. M. Siegel 2021). A similar value of $\gtrsim 10^{-4} M_\odot \text{s}^{-1}$ has been recently obtained for magnetized accretion onto a neutron star (L. Combi et al. 2025). Once the accretion flow establishes full degeneracy, the accretion rate is typically large enough for the flow to become opaque to neutrinos (the opaque threshold \dot{M}_ν). At even larger accretion rates and disk densities the accretion timescale becomes short compared to the vertical neutrino diffusion timescale, and neutrinos become trapped in the flow and get advected into the black hole (the ‘trapping threshold’ $\dot{M}_{\nu-\text{trap}}$).

Conditions for neutrino-cooled accretion can be realized in a number of astrophysical systems. The core-collapse of rapidly rotating, massive stars leading to a rapidly spinning black hole can give rise to an accretion disk that self-neutronizes (B. D. Metzger et al. 2008b; D. M. Siegel et al. 2019; A. Agarwal et al. 2025).

Circularizing debris in neutron-star mergers forms a post-merger accretion disk around a remnant neutron star or black hole that can self-neutronize over viscous timescales (B. D. Metzger et al. 2008a; D. M. Siegel & B. D. Metzger 2017; R. Fernández et al. 2019; L. Combi & D. M. Siegel 2023). r -process elements synthesized in the outflows from post-merger accretion disks around a final black hole remnant represent the most natural explanation for the dominant ejecta source and red kilonova emission in GW170817 (D. M. Siegel & B. D. Metzger 2018; R. Fernández et al. 2019; I. M. Christie et al. 2019; S. Fujibayashi et al. 2020), and earlier outflows from an accretion disk around a remnant neutron star likely generated the blue kilonova emission following GW170817 (V. Nedora et al. 2019; L. Combi & D. M. Siegel 2023). It has been conjectured that outflows from post-merger accretion disks also dominate the total ejecta of neutron-star mergers as a population (D. M. Siegel 2022). Finally, conditions conducive for self-neutronization may be realized in the accretion-induced collapse (AIC) of rapidly rotating white dwarfs that yield a proto-neutron star surrounded by an accretion disk (L. Dessart et al. 2006; B. D. Metzger et al. 2009; E. Batziou et al. 2024; P. C.-K. Cheong et al. 2025).

Though similarities exist, super-critical accretion onto neutron stars is fundamentally different from the black hole case due to non-absorbing inner boundary conditions at the stellar surface that alter energy and angular-momentum transport (L. Combi et al. 2025). Additionally, if the neutron star is hot, as in neutron-star merger and AIC events, strong neutrino emission from the neutron star irradiates the accretion disk and its outflows and strongly impacts r -process nucleosynthesis (J. Lippuner et al. 2017; S. Fujibayashi et al. 2018; L. Combi & D. M. Siegel 2023). Here, we focus on neutrino-cooled accretion onto black holes, with a primary focus on collapsars, as we are interested in exploring the entire parameter space of black hole masses up to $\sim 100 - 1000 M_\odot$.

Collapsars represent the leading model for the central engine of long GRBs (S. E. Woosley 1993; A. I. MacFadyen & S. E. Woosley 1999). Both theoretical arguments (A. Heger et al. 2005; O. Gottlieb et al. 2024) and observed ejecta properties of GRB-accompanying Type Ic-BL supernovae (S. E. Woosley & J. S. Bloom 2006) suggest that typical long GRBs result from the core collapse of progenitor stars with zero-age main sequence masses $M_{\text{ZAMS}} \lesssim 40 M_\odot$ and helium cores at core-collapse of $\lesssim 10 M_\odot$. The collapsing core may undergo a potentially brief phase of proto-neutron star formation that via luminous neutrino radiation and strong

³ See F.-K. Thielemann et al. (2020) for a compilation of caveats to this conclusion.

magnetic fields might power a (partial) prompt explosion, leading to the synthesis of ^{56}Ni and the generation of a Type Ic-BL supernova. The collapsing stellar layers with $Y_e \simeq 0.5$ circularize in the equatorial plane at increasing radii with time (Y. Zenati et al. 2020), determined by angular momentum conservation. They feed an accretion disk that can maintain self-neutronization at $\dot{M} > \dot{M}_{\text{ign}}$ during much of the early epoch in which the GRB jet is powered by a stellar-mass black hole of typically a few solar masses (D. M. Siegel et al. 2019, 2022). Magnetized accretion is likely required to enable an r -process in the disk outflows during this phase (D. M. Siegel & B. D. Metzger 2018; R. Fernández et al. 2019; C. Dean & R. Fernández 2024; D. Issa et al. 2025; M. Shibata et al. 2025). The detailed abundance distribution depends on the neutrinos’ irradiation of the outflows, which increases Y_e (J. M. Miller et al. 2020; X. Li & D. M. Siegel 2021), and on the occurrence of neutrino fast flavor conversions, which tend to decrease Y_e (X. Li & D. M. Siegel 2021). Depending on the degree of mixing of the outflows with the infalling stellar material (J. Barnes & P. C. Duffell 2023), the high line expansion opacities of the lanthanide and actinide elements (D. Kasen et al. 2013; M. Tanaka & K. Hotokezaka 2013) trap photons in the expanding ejecta and thus redden the supernova emission; the synthesized heavy elements also contribute additional heating and thus excess emission, which eventually dominates on long timescales ~ 100 days after the explosion, likely when the supernova has reached the nebular phase (D. M. Siegel et al. 2019; J. Barnes & B. D. Metzger 2022). First observational searches for such signatures based on photospheric emission are inconclusive (S. Anand et al. 2024; J. C. Rastinejad et al. 2024; P. K. Blanchard et al. 2024).

Very massive stars $M_{\text{ZAMS}} \gtrsim 40$ end their lives in pair-instability driven explosive oxygen burning (pair instability supernovae; PISNe) prior to reaching iron-core collapse, leaving no black hole remnant behind (Z. Barkat et al. 1967; S. E. Woosley et al. 2002; H. Umeda & K. Nomoto 2002; S. E. Woosley & W. Zhang 2007; M. Renzo et al. 2020; R. Farmer et al. 2019; S. E. Woosley & A. Heger 2021). At low metallicity, even more massive stars with $M_{\text{ZAMS}} \gtrsim 250 M_{\odot}$ are predicted to evolve to helium core masses $\gtrsim 130 M_{\odot}$ above this black hole pair-instability mass gap at core collapse. Strong photoionization losses at the onset of explosive oxygen burning in such stars (M. Renzo et al. 2020) or a radial gravitational instability (S. Chandrasekhar 1964) for super massive stars $\sim 10^4 - 10^5 M_{\odot}$ can drive very massive to super massive stars to collapse into black holes (J. R. Bond et al. 1984; C. L. Fryer et al. 2001; C. Nagele et al. 2022). If such stars are rapidly rotat-

ing at collapse (P. Marchant & T. J. Moriya 2020; L. Haemmerlé et al. 2018; K. Kimura et al. 2023), e.g. due to continuous gas accretion throughout their lifetime (e.g. M. Cantiello et al. 2021; A. S. Jermyn et al. 2021; A. J. Dittmann et al. 2021) or due to tidal locking in close binaries, they can give rise to collapsar-like accretion disks. Owing to the much larger helium core masses such collapsars can, in principle, synthesize much larger quantities of $\sim 1 - 100 M_{\odot}$ of r -process material per event relative to ordinary collapsars and, following disk wind mass loss, give birth to massive black holes $M_{\bullet} \sim 10^2 - 10^4 M_{\odot}$. The lower end of this mass distribution can populate the PISN black hole mass gap ‘from above’, with rates compatible with recent detections by the gravitational-wave observatories LIGO-Virgo-Kagra (GW190521, GW231123; R. Abbott et al. 2020; The LIGO Scientific Collaboration et al. 2025; D. M. Siegel et al. 2022; A. Agarwal et al. 2025). Estimating from an initial mass function, such events should be rare compared to ordinary collapsars, but they may represent a prolific source of r -process elements at low metallicity, as early as the first generation of stars (Population III stars).

Such “super-collapsars” may give rise to exceptionally energetic ($\sim 10^{54}$ erg) GRBs (S. S. Komissarov & M. V. Barkov 2010; P. Mészáros & M. J. Rees 2010; Y. Suwa & K. Ioka 2010; S.-C. Yoon et al. 2015). Since the binding energies of the progenitor envelopes by far exceed both the rotational energy of a proto-neutron star and its binding energy available to neutrino emission, they are unlikely associated with typical Type Ic-BL supernovae, yet ^{56}Ni can be produced via jet-envelope interaction (J. Barnes et al. 2018), an α -process in disk outflows once self-neutronization ceases (B. D. Metzger et al. 2008b; D. M. Siegel et al. 2019), and nuclear burning of light nuclei in the accretion disk at later accretion epochs (Y. Zenati et al. 2020). Likely unaccompanied by promptly generated Ic-BL supernovae, the much larger quantities of neutron-rich disk winds compared to ordinary collapsars may give rise to “super-kilonovae” (D. M. Siegel et al. 2022), kilonova-like emission on timescales of weeks to months that can be detected by targeted follow-up of particularly energetic GRBs and by infrared surveys such as those planned for the Roman Space Telescope (D. M. Siegel et al. 2022).

Due to computational cost, recent multidimensional simulations in viscous hydrodynamics and magnetohydrodynamics of both isolated collapsar accretion disks (D. M. Siegel et al. 2019; J. M. Miller et al. 2020; A. Agarwal et al. 2025) and the global collapse process (O. Just et al. 2022; C. Dean & R. Fernández 2024; D. Issa et al. 2025; M. Shibata et al. 2025) can only fo-

cus on at most a few models (parameter values) at a given time and have (with the exception of [A. Agarwal et al. \(2025\)](#)) thus far focused on accretion onto stellar-mass black holes and ordinary collapsars. [A. Agarwal et al. \(2025\)](#) find using three-dimensional, general-relativistic magnetohydrodynamic simulations of collapsar accretion disks with weak interactions that ignition of weak interactions and the onset of degeneracy as well as self-neutronization occurs for accretion onto black holes with an ignition accretion rate $\dot{M}_{\text{ign}} \propto M_{\bullet}^{4/3} \alpha^{5/3}$ up to $M_{\bullet} \lesssim 3000 M_{\odot}$, where the disk temperature at \dot{M}_{ign} decreases below the proton-neutron mass difference such that electron and positron capture reactions are suppressed and the composition freezes. Yet self-neutronization can, in principle, still occur at higher accretion rates.

In this paper, we present a one-dimensional, stationary, general-relativistic viscous hydrodynamic model of neutrino-cooled accretion disks. With this computationally inexpensive framework, we explore and map out the entire parameter space of neutrino-cooled accretion onto black holes of mass $M_{\bullet} \sim 1 - 10^4 M_{\odot}$, dimensionless spin $\chi_{\bullet} \in [0, 1)$, and effective α -viscosity of $\alpha \sim 10^{-3} - 1$. We focus on the general physical processes that regulate the disk composition, with emphasis on neutronization as a necessary requirement for r -process nucleosynthesis in disk outflows. We identify various accretion regimes and provide analytic modeling to approximately delineate these regimes. At sufficiently high accretion rates and sufficiently large radii, the accretion disks become gravitationally unstable ([A. Toomre 1964](#); [B. Paczynski 1978](#)) and fragmentation together with sufficient cooling ([C. F. Gammie 2001](#)) may lead to the formation of small, bound, neutron star like objects that can give rise to GRB variability, gravitational-wave emission, and additional electromagnetic transients ([A. L. Piro & E. Pfahl 2007](#); [B. D. Metzger et al. 2024](#); [Y. Lerner et al. 2025](#)). Since the stationary, non-self-gravitating model formally breaks down in this limit, here we focus on the gravitationally stable part of the parameter space. Parameter space exploration with this one-dimensional model, together with the analytic insight gained, can direct current and future sophisticated multi-dimensional simulations of collapsar and super-collapsar accretion processes and their observational signatures, nucleosynthesis analyses, and provides as a basis for interpreting simulation results.

This paper is structured as follows. In [Section 2](#) and [Appendix A](#) we describe the black hole-accretion disk model. We define characteristic accretion regimes and derive approximate analytical scaling relations for the characteristic accretion rates that delineate these

regimes in [Section 3](#). [Section 4](#) discusses the numerical method used to solve the coupled set of disk equations. In [Section 5](#), we present numerical results from a parameter space survey for the physics of the accretion flow, with a focus on disk composition, as well as numerical results for the characteristic accretion rates that delineate qualitatively different accretion regimes. In [Section 6](#), we discuss our results in comparison to three-dimensional GRMHD simulations of collapsar accretion disks and comment on implications for “super-kilonovae” from collapsars that populate the PISN mass-gap as well as for exceptionally bright GRB events such as GRB221009A. [Section 7](#) summarizes our conclusions. In most of this work, we use geometric units $G = c = 1$, unless these constants explicitly appear.

2. ACCRETION DISK MODEL

Accreting matter around a black hole is modeled using a variant of the one-dimensional, general-relativistic Novikov-Thorne model ([I. D. Novikov & K. S. Thorne 1973](#)), which has been extended and applied in many subsequent works (e.g. [A. M. Beloborodov et al. 1997](#); [A. M. Beloborodov 1999](#); [W.-X. Chen & A. M. Beloborodov 2007](#); [N. Kawanaka & S. Mineshige 2007](#); [A. Janiuk 2014](#); [S. De & D. M. Siegel 2021](#)). The basic underlying assumptions include (1) spacetime is given by a Kerr black hole and it is not affected by the mass of the disk nor by the mass accreted into the black hole, (2) the accretion process is steady, with a constant accretion rate (radially, and in time), (3) the disk is axisymmetric, located in the equatorial plane of the Kerr spacetime, and (4) the vertical extent is small compared to the radial extent ($z/r \ll 1$). Disk quantities thus become time-independent, they can be azimuthally and vertically averaged and are thus only a function of radius r .

Here, we closely follow the formulation by [I. D. Novikov & K. S. Thorne \(1973\)](#) and [D. N. Page & K. S. Thorne \(1974\)](#) with corrections to zero order in z/r regarding vertical pressure balance by [H. Riffert & H. Herold \(1995\)](#), resulting in a model nearly identical to [W.-X. Chen & A. M. Beloborodov \(2007\)](#), albeit with some modifications and additions. For completeness and reference, this section together with [Appendix A](#) summarize the disk model in a self-consistent derivation. We start by defining the spacetime and deriving the structural equations of the disk from conservation laws ([Section 2.1](#)). [Sections 2.2, 2.3, and 2.4](#) discuss the local microphysical state of the disk and neutrino cooling.

2.1. Disk structure equations

We assume a non-self-gravitating disk and fix the spacetime to a Kerr black hole of mass M_{\bullet} , spin pa-

parameter $a_\bullet \in [0, M_\bullet)$ and dimensionless spin parameter $\chi_\bullet = a_\bullet/M_\bullet \in [0, 1)$. We transform the metric $g_{\mu\nu}$ in Boyer-Lindquist coordinates $x^\mu = (t, r, \theta, \phi)$ with line element

$$ds^2 = -dt^2 + \varrho^2 \left(\frac{dr^2}{\Delta} + d\theta^2 \right) + (r^2 + a_\bullet^2) \sin^2\theta d\phi^2 + \frac{2M_\bullet r}{\varrho^2} (a_\bullet \sin^2\theta d\phi - dt)^2, \quad (1)$$

with $\Delta(r) = r^2 - 2M_\bullet r + a_\bullet^2$ and $\varrho^2(r, \theta) = r^2 + a_\bullet^2 \cos^2\theta$, into cylindrical coordinates $x^\mu = (t, r, \phi, z)$, where $z = r \cos\theta$, and expand the metric coefficients up to second order $\mathcal{O}((z/r)^2)$ in height z , as required by the structure equation of vertical balance (Appendix A).

The accreting material inside the disk is characterized by its four-velocity $u^\alpha = (u^t, u^r, u^\phi, u^z)$. We henceforth exclusively refer to time-averaged quantities, assuming that local fluctuations due to fluid turbulence in the disk are adequately averaged over. According to the above model assumptions, we can then assume $u^\alpha = (u^t, u^r, u^\phi, 0)$ with nearly geodesic fluid motion, $|u^r| \ll |u^\phi|, |u^t|$. The local (proper) half-thickness of the disk is denoted by

$$H(r) = \int_0^{z_d(r)} \sqrt{g_{zz}} dz, \quad (2)$$

where $z_d(r)$ denotes the local disk coordinate height. The thin-disk approximation translates into $H/r \ll 1$, which is motivated in our case by the fact that we are interested in neutrino-dominated accretion flows (NDAFs), for which the accretion disk becomes geometrically thin ($H/r \lesssim 0.1$) as a result of neutrino cooling. The assumption is less well justified in the advection-dominated case, in which viscous heating is not balanced by neutrino cooling and the accretion disk remains geometrically thick ($H/r \gtrsim 0.4$).

The disk structure equations follow from the conservation laws of baryon number,

$$\nabla_\mu(\rho u^\mu) = 0, \quad (3)$$

lepton number,

$$\nabla_\mu(n_{\text{lep}} u^\mu) = R, \quad (4)$$

and energy-momentum,

$$\nabla_\mu T^{\mu\nu} = 0. \quad (5)$$

Here, $\rho = m_p n_b$ is the rest-mass density, with m_p the proton mass and n_b the baryon number density.⁴ Furthermore, $n_{\text{lep}} = n_{e^-} - n_{e^+} + n_\nu - n_{\bar{\nu}}$ denotes the lepton

number, with n_{e^-} , n_{e^+} , n_ν and $n_{\bar{\nu}}$ being the number densities of electrons, positrons, electron neutrinos, and electron antineutrinos, respectively. The sink term

$$R = -\frac{1}{H}(\dot{n}_{\nu_e} - \dot{n}_{\bar{\nu}_e}) \quad (6)$$

represents the lepton number per unit volume per unit time in the rest frame of the fluid radiated away from the accretion disk in the form of electron neutrinos and antineutrinos; \dot{n}_ν and $\dot{n}_{\bar{\nu}}$ represent the number *emission* rates per unit area of electron neutrinos and antineutrinos, respectively, hence the minus sign in Equation (6) (see Section 2.4 for details). The energy-momentum tensor $T^{\mu\nu}$ is given by

$$T^{\mu\nu} = \rho h u^\mu u^\nu + p g^{\mu\nu} + t^{\mu\nu} + q^\mu u^\nu + q^\nu u^\mu, \quad (7)$$

with $h = 1 + (e + p)/\rho$ the relativistic specific enthalpy, p the pressure, e the internal energy density, $t^{\mu\nu}$ the viscous stress tensor, and q^μ the neutrino energy flux vector.

Integrating Equation (3) over a spacetime volume between r and $r + \Delta r$ and t and $t + \Delta t$ yields

$$\dot{M} = -4\pi\sqrt{-g}\rho H u^r = \text{const.}, \quad (8)$$

i.e. a constant accretion rate \dot{M} as a function of radius.

With the help of Equation (3), the conservation of lepton number (Equation (4)), height-integrated according to Equation (2), implies (cf. Appendix A)

$$H u^r \left[\frac{\rho}{m_p} \frac{dY_e}{dr} - \frac{n_{\nu_e} - n_{\bar{\nu}_e}}{\rho} \frac{d\rho}{dr} + \frac{d(n_{\nu_e} - n_{\bar{\nu}_e})}{dr} \right] = \dot{n}_{\bar{\nu}_e} - \dot{n}_{\nu_e}, \quad (9)$$

where $Y_e = n_p/n_b$ is the electron or, more precisely, the proton-fraction. This expression is identical to Equation (9) of W.-X. Chen & A. M. Beloborodov (2007), except for a term proportional to the density gradient, which is absent in the formulation of W.-X. Chen & A. M. Beloborodov (2007). In contrast to, e.g., radial pressure gradients, this term is, in principle, non-negligible given the set of assumptions made here. We find that it can lead to changes of individual disk quantities at the tens-of-percent level.

By projecting Equation (5) onto u^μ and orthogonal to u^μ using the projection tensor $\mathcal{P}^{\alpha\beta} = u^\alpha u^\beta + g^{\alpha\beta}$, one obtains expressions for energy and momentum conservation, respectively. From the radial component ($i = 1$) of $\mathcal{P}^{i\nu} \nabla_\mu T^\mu_\nu = 0$ (radial momentum balance), we obtain to lowest order in small quantities (cf. Appendix A)

$$\Omega \equiv \frac{u^\phi}{u^t} = \frac{M_\bullet^{1/2}}{r^{3/2}} \frac{1}{\mathcal{B}} = \left(\frac{r^{3/2}}{M_\bullet^{1/2}} + \chi_\bullet M_\bullet \right)^{-1}, \quad (10)$$

⁴ We choose the baryon mass to be the proton mass and neglect the proton-neutron rest-mass difference for purposes of computing the rest-mass density of baryonic material.

i.e. the geodesic motion of fluid elements. In particular, radial pressure gradients have been neglected here. For the definition of the auxiliary functions \mathcal{A} , \mathcal{B} , \mathcal{C} , \mathcal{D} , J , S , we refer to Appendix A.

From the z -component ($i = 3$) of $\mathcal{P}^{i\nu}\nabla_\mu T^\mu_\nu = 0$ integrated over height (vertical momentum balance), we obtain to lowest order in small quantities (cf. Appendix A)

$$\left(\frac{H}{r}\right)^2 = \frac{p}{\rho} \frac{r}{JM_\bullet}, \quad (11)$$

which differs from the expression of I. D. Novikov & K. S. Thorne (1973) and contains the full relativistic corrections to the tidal force in general relativity to zero order in z/r as pointed out by H. Riffert & H. Herold (1995) (and used by A. M. Beloborodov 1999; W.-X. Chen & A. M. Beloborodov 2007).

From the equation of energy conservation, $u^\nu\nabla_\mu T^\mu_\nu = 0$, integrated over height, we obtain to lowest order (cf. Appendix A)

$$u^r \left(\frac{d(eH)}{dr} - \frac{e+p}{\rho} \frac{d(\rho H)}{dr} \right) = F^+ - F^-. \quad (12)$$

Here,

$$F^- \equiv q^z(z=H) = F_\nu + F_{\bar{\nu}} \quad (13)$$

is the z -component of the radiation flux q^μ in the rest frame of the fluid leaving the disk at $z = H$. The electron neutrino and antineutrino cooling (emission) fluxes F_ν and $F_{\bar{\nu}}$ depend directly on the microphysical state of the disk plasma. neutrino cooling is discussed in Section 2.4. Together with the equation of azimuthal momentum balance (see below), one obtains for the viscous heating rate to lowest order (Appendix A)

$$F^+ \equiv - \int_0^H t^{\mu\nu} \sigma_{\mu\nu} \sqrt{g_{zz}} dz = \frac{3\dot{M}M_\bullet}{8\pi r^3} \frac{\mathcal{D}^2}{\mathcal{C}^2} S, \quad (14)$$

where $\sigma_{\mu\nu}$ denotes the shear tensor. We note that the latter expression is identical to the expressions used by, e.g., A. M. Beloborodov et al. (1997), A. M. Beloborodov (1999), and differs from that of W.-X. Chen & A. M. Beloborodov (2007) only by a factor of $h \simeq 1$ (see Appendix A). However, introducing the additional factor of the specific enthalpy renders the heating rate inconsistent with both the height-integrated energy balance and the height-integrated azimuthal momentum balance.

The ϕ -component ($i = 2$) of $\mathcal{P}^{i\nu}\nabla_\mu T^\mu_\nu = 0$ (azimuthal momentum balance) yields to lowest order in small quantities (cf. Appendix A) the identity

$$t_{\hat{r}\hat{\phi}} = -r\rho u^r \frac{M_\bullet^{1/2}}{r^{3/2}} \frac{\mathcal{C}^{1/2}\mathcal{D}}{\mathcal{B}\mathcal{D}}, \quad (15)$$

where $t_{\hat{r}\hat{\phi}}$ denotes the r - ϕ component of $t^{\mu\nu}$ in the co-moving tetrad frame of the orbiting fluid.

We adopt the α -viscosity ansatz (N. I. Shakura & R. A. Sunyaev 1973), i.e. we assume that accretion is driven by viscous stress with a kinematic viscosity given by $\nu = \frac{2}{3}\alpha c_s H$, where $c_s \equiv \sqrt{p/\rho}$ is the isothermal sound speed and $\alpha \in (0, 1)$ specifies the typical turbulent eddy velocity as a fraction of the local sound speed. Viscous stress in astrophysical accretion disks is generated by magnetohydrodynamic turbulence driven by the magnetorotational instability. Numerical simulations suggest typical effective values of α of $\alpha \approx 0.005 - 0.1$ (e.g., S. A. Balbus & J. F. Hawley 1998; J. F. Hawley & S. A. Balbus 2002; R. F. Penna et al. 2013; S. De & D. M. Siegel 2021; A. Agarwal et al. 2025). This α -viscosity ansatz leads to an expression of the r - ϕ component of the stress tensor in the co-moving tetrad, which is proportional to pressure (Appendix A),

$$t_{\hat{r}\hat{\phi}} = \alpha p \frac{\mathcal{D}}{\mathcal{C} J^{1/2}}. \quad (16)$$

The factor $\mathcal{D}/(\mathcal{C} J^{1/2})$ represents a relativistic correction relative to the Newtonian ansatz pointed out by H. Riffert & H. Herold (1995), which makes the resulting expression consistent with relativistic vertical momentum balance.

Inserting the ansatz (16) into Equation (15) results in

$$u^r = -\frac{H}{r} \alpha c_s S^{-1}. \quad (17)$$

This relation is identical to Equation (3) of W.-X. Chen & A. M. Beloborodov (2007).

2.2. Chemical composition

The plasma inside the disk is modeled as a mixture of electrons, positrons, protons, neutrons, α -particles, neutrinos and antineutrinos in thermal equilibrium. Electrons and positrons are modeled as ideal Fermi gases and thus follow a Fermi-Dirac distribution. Their number densities are given by (cf. Equation (B61))

$$n_{e^\pm} = \frac{(m_e c)^3}{\pi^2 \hbar^3} \int_0^\infty f(\sqrt{\xi^2 + 1}, \mp \eta_e, \theta) \xi^2 d\xi, \quad (18)$$

with

$$f(E, \eta, \theta) = \frac{1}{\exp(E/\theta - \eta) + 1}, \quad (19)$$

where E denotes energy in units of $m_e c^2$, $\eta_e = \mu_{e^-}/k_B T$ is the normalized chemical potential, and $\theta = k_B T/m_e c^2$ is the normalized temperature, $\hbar = h/2\pi$ the reduced Planck constant, k_B the Boltzmann constant, and m_e the electron mass. Furthermore, $\eta_{e^+} = -\eta_{e^-}$, which follows from the assumption that creation of pairs is in thermal equilibrium inside the disk, $e^- + e^+ \leftrightarrow 2\gamma$. This yields for the chemical potentials $\mu_{e^-} + \mu_{e^+} = 2\mu_\gamma = 0$.

Charge neutrality of the disk plasma then dictates the proton number density to follow

$$n_p = n_{e^-} - n_{e^+}, \quad (20)$$

and the neutron number density can be expressed as

$$n_n = \left(\frac{1 - Y_e}{Y_e} \right) n_p. \quad (21)$$

The number density of α -particles is given by

$$n_\alpha = \frac{1}{4}(n_p + n_n)(1 - X_f). \quad (22)$$

Here, X_f is the free-nucleon mass fraction, which, assuming nuclear statistical equilibrium, is given by (e.g., B. S. Meyer 1994),

$$\frac{3.780 \times 10^{16}}{(1.027 \times 10^{12})^{1/\theta}} \frac{\theta^{9/4}}{\rho^{3/2}} = \left(Y_e - \frac{1 - X_f}{2} \right) \left(1 - Y_e - \frac{1 - X_f}{2} \right) \frac{1}{\sqrt{1 - X_f}}. \quad (23)$$

Consistent with the assumption in Section 2.1, we set the baryon mass m_b to the proton mass and express the plasma density as

$$\rho = m_b n_b = \frac{m_p n_p}{Y_e}. \quad (24)$$

Where the disk plasma becomes optically thick to electron neutrinos and antineutrinos, we assume thermodynamic equilibrium is established via

$$e^- + p \rightleftharpoons n + \nu, \quad (25)$$

$$e^+ + n \rightleftharpoons p + \bar{\nu}, \quad (26)$$

such that they form an ideal Fermi gas with number densities given by (see Equation (B66))

$$n_{\nu_e, \bar{\nu}_e} = \frac{(k_B T)^3}{2\pi^2 (\hbar c)^3} \int_0^\infty d\xi \frac{\xi^2}{\exp(\xi \mp \eta_\nu) + 1}. \quad (27)$$

The degeneracy parameter of electron neutrinos $\eta_\nu \equiv \eta_{\nu_e} = -\eta_{\bar{\nu}_e}$ follows from chemical equilibrium of Equations (25)–(26), $\mu_{e^-} - \mu_{e^+} = \mu_n - \mu_p$, $-\mu_{e^+} + \mu_{\bar{\nu}_e} = \mu_n - \mu_p$. Further assuming that n_n and n_p follow Maxwellian distributions, one obtains (cf. also A. M. Beloborodov 2003)

$$\eta_e - \eta_\nu = \ln \left(\frac{1 - Y_e}{Y_e} \right) + \frac{Q}{\theta}, \quad (28)$$

where $Q \equiv (m_n - m_p)/m_e \approx 2.531$.

2.3. Equation of state & thermodynamic quantities

We construct the equation of state in the independent thermodynamic variables ρ , T , and Y_e based on the Helmholtz free energy,

$$\mathcal{F} = \mathcal{F}_b + \mathcal{F}_\gamma + \mathcal{F}_{e^+} + \mathcal{F}_{e^-} + \mathcal{F}_\nu + \mathcal{F}_{\bar{\nu}}, \quad (29)$$

considering contributions from baryonic plasma (b), radiation (γ), electrons and positrons (e^\pm), and (electron) neutrinos and antineutrinos (ν , $\bar{\nu}$). All dependent thermodynamic variables such as pressure p , internal energy density e , and specific entropy s with their partial components are consistently computed as partial derivatives of the free energy. We derive these expressions in Appendix B.

2.4. Plasma cooling via neutrino emission

The disk plasma cools through the fluxes of free-streaming neutrinos and antineutrinos, which, for one half disk, we define as

$$F_{\nu, \bar{\nu}} = (1 - x_{\nu, \bar{\nu}}) F_{\nu, \bar{\nu}}^{\text{transp}} + x_{\nu, \bar{\nu}} F_{\nu, \bar{\nu}}^{\text{opaque}}. \quad (30)$$

The transition parameters

$$x_{\nu, \bar{\nu}} = \exp \left(- \frac{e_{\nu, \bar{\nu}}^{\text{opaque}}}{e_{\nu, \bar{\nu}}^{\text{transp}}} \right) \quad (31)$$

smoothly interpolate between the optically thin and optically thick limits using their respective energy densities, defined in Equations (33) and (B65).

In the optically thick limit, the fluxes can be written as

$$F_{\nu_e, \bar{\nu}_e}^{\text{opaque}} = \frac{c}{\exp(\tau_{\nu_e, \bar{\nu}_e})} e_{\nu_e, \bar{\nu}_e}^{\text{opaque}}. \quad (32)$$

Here, $\tau_{\nu_e, \bar{\nu}_e}$ denote the total optical depths of electron neutrinos and electron antineutrinos, which we compute as described by W.-X. Chen & A. M. Beloborodov (2007), considering the processes of neutrino absorption by nucleons, elastic neutrino-baryon scattering, and scattering of neutrinos off electrons and positrons.

In the free-streaming regime, the energy densities of the radiation fluxes are given by

$$e_{\nu, \bar{\nu}}^{\text{transp}} = \frac{1}{c} F_{\nu_e, \bar{\nu}_e}^{\text{transp}} + \frac{1}{c} F_{\nu_\mu, \bar{\nu}_\mu}^{\text{transp}} + \frac{1}{c} F_{\nu_\tau, \bar{\nu}_\tau}^{\text{transp}}. \quad (33)$$

Here, F_ν^{transp} and $F_{\bar{\nu}}^{\text{transp}}$ denote the vertically integrated, free-streaming neutrino fluxes.

The main source of optically thin cooling of the disk is via emission of electron neutrinos and antineutrinos as a result of electron and positron captures into nucleons (Equations (25) and (26)). The free-streaming neutrino

and antineutrino fluxes for these processes read (S. L. Shapiro & S. A. Teukolsky 1983)

$$F_{\nu_e(e^- \text{ capture})} = H(n_p - 2n_\alpha)K_{e^\pm N}m_e c^2 \times \int_0^\infty f(E+Q, \eta_e, \theta)(E+Q)^2 \sqrt{1 - \frac{1}{(E+Q)^2}} E^3 dE \quad (34)$$

and

$$F_{\bar{\nu}_e(e^+ \text{ capture})} = H(n_n - 2n_\alpha)K_{e^\pm N}m_e c^2 \times \int_{Q+1}^\infty f(E-Q, -\eta_e, \theta)(E-Q)^2 \sqrt{1 - \frac{1}{(E-Q)^2}} E^3 dE, \quad (35)$$

where $K_{e^\pm N} = 6.5 \times 10^{-4} \text{s}^{-1}$, and $n_p - 2n_\alpha$ and $n_n - 2n_\alpha$ denote the free proton and neutron number densities, respectively.

A secondary source of neutrino cooling is e^\pm -pair annihilation into all neutrino flavors,

$$e^- + e^+ \longrightarrow \nu + \bar{\nu}. \quad (36)$$

This process is most relevant in conditions of dominant radiation and/or relativistic e^\pm pressure (Equations (34), (35) and (38)):

$$\frac{F_{\nu(e^\pm \text{ annihilation})}}{F_{\nu(e^\pm \text{ capture})}} \propto \frac{T^9}{\rho T^6} \propto \frac{p_{\gamma, e^\pm}}{p_b}. \quad (37)$$

As we discuss in Section 5.6, radiation pressure can account for ~ 30 - 60% of the total pressure in the inner part of accretion disks at accretion rates when weak interactions become energetically significant (Figs. 6 and 7), suggesting that this process could be relevant for at least part of the parameter space probed here. The total vertically integrated free-streaming neutrino flux of one half-disk for this process reads (A. Burrows et al. 2006)

$$F_{\nu(e^\pm \text{ annihilation})} = HK_{e^\pm \nu} \frac{m_e^7 c^8}{\hbar^6} \times \int_0^\infty f(E, \eta_e, \theta) E^4 dE \int_0^\infty f(E, -\eta_e, \theta) E^3 dE, \quad (38)$$

where $K_{e^\pm \nu} = K_{e^\pm \nu_e} \approx 3.4256 \times 10^{-37} \text{cm}^3 \text{s}^{-1}$ for the production of electron neutrinos, and $K_{e^\pm \nu} = K_{e^\pm \nu_{\tau, \mu}} \approx 0.73564 \times 10^{-37} \text{cm}^3 \text{s}^{-1}$ for the production of muon or tau neutrinos. The definition of $F_{\bar{\nu}(e^\pm \text{ annihilation})}$ is analogous, with the replacement $\eta_e \rightarrow -\eta_e$.

The total flux in the transparent regime is given by

$$F_\nu^{\text{transp}} = \frac{F_{\nu_e(e^- \text{ capture})}}{\exp(\tau_{\nu_e})} + \frac{F_{\nu_e, \nu_\tau, \nu_\mu(e^\pm \text{ annihilation})}}{\exp(\tau_{\nu_e, \nu_\tau, \nu_\mu})}, \quad (39)$$

with an analogous expression for $F_{\bar{\nu}}^{\text{transp}}$. We consider effective total optical depths $\tau_{\nu_\tau} = \tau_{\nu_\mu} = 0$ for the muon and tau neutrino flavors.

While this concludes the calculation of the cooling terms for the disk structure equations (Section 2.1), we compute two additional quantities of interest—the number flux of electron neutrinos and antineutrinos and their mean energies.

In the transparent regime, the number fluxes of neutrinos and antineutrinos produced by electron and positron capture are computed in an analogous way to the fluxes discussed above,

$$\dot{n}_{\nu_e(e^- \text{ capture})} = H(n_p - 2n_\alpha)K_{e^\pm N} \times \int_0^\infty f(E+Q, \eta_e, \theta)(E+Q)^2 \sqrt{1 - \frac{1}{(E+Q)^2}} E^2 dE, \quad (40)$$

$$\dot{n}_{\bar{\nu}_e(e^+ \text{ capture})} = H(n_n - 2n_\alpha)K_{e^\pm N} \times \int_{Q+1}^\infty f(E-Q, -\eta_e, \theta)(E-Q)^2 \sqrt{1 - \frac{1}{(E-Q)^2}} E^2 dE. \quad (41)$$

The mean energies of neutrinos and antineutrinos are then given by

$$\langle E_{\nu_e, \bar{\nu}_e(e^\pm \text{ capture})} \rangle = \frac{F_{\nu_e, \bar{\nu}_e(e^\pm \text{ capture})}}{\dot{n}_{\nu_e, \bar{\nu}_e(e^\pm \text{ capture})}}, \quad (42)$$

where $F_{\nu_e, \bar{\nu}_e(e^\pm \text{ capture})}$ corresponds to the associated flux from Equation (34) or (35). For electron neutrinos emitted due to electron-positron annihilation, the number flux and mean energy of neutrinos are given by

$$\dot{n}_{\nu_e(e^\pm \text{ annihilation})} = HK_{e^\pm \nu_e} \left(\frac{m_e c}{\hbar} \right)^6 \times \int_0^\infty f(E, \eta_e, \theta) E^3 dE \int_0^\infty f(E, -\eta_e, \theta) E^3 dE, \quad (43)$$

and

$$\langle E_{\nu_e(e^\pm \text{ annihilation})} \rangle = \frac{F_{\nu_e(e^\pm \text{ annihilation})}}{\dot{n}_{\nu_e(e^\pm \text{ annihilation})}}, \quad (44)$$

respectively. Analogous expressions hold for antineutrinos, using the replacement $\eta_e \rightarrow -\eta_e$. Employing these definitions, it is straightforward to check that

$$\dot{n}_{\nu_e(e^\pm \text{ annihilation})} = \dot{n}_{\bar{\nu}_e(e^\pm \text{ annihilation})} \quad (45)$$

as expected, since neutrinos and antineutrinos are emitted in pairs.

The total electron neutrino number density in the transparent regime is then given by the sum of the contributions of both processes,

$$\dot{n}_{\nu_e}^{\text{transp}} = \frac{\dot{n}_{\nu_e}(e^- \text{ capture}) + \dot{n}_{\nu_e}(e^\pm \text{ annihilation})}{\exp(\tau_{\nu_e})}. \quad (46)$$

In the opaque regime, we consider the neutrino number densities and average energy given in Equation (B66) to obtain

$$\dot{n}_{\nu_e}^{\text{opaque}} = \frac{c}{\exp(\tau_{\nu_e})} n_{\nu_e}. \quad (47)$$

and

$$\langle E_{\nu_e(\text{thermalized}-\nu_e)} \rangle = \frac{F_{\nu_e}^{\text{opaque}}}{\dot{n}_{\nu_e}^{\text{opaque}}} = \frac{e_{\nu_e}^{\text{opaque}}}{n_{\nu_e}^{\text{opaque}}}. \quad (48)$$

Finally, we ensure a smooth transition between the different regimes by using a formula analogous to Equation (30),

$$\dot{n}_\nu = (1 - x_\nu) \dot{n}_{\nu_e}^{\text{transp}} + x_\nu \dot{n}_{\nu_e}^{\text{opaque}}. \quad (49)$$

Analogous expressions hold for electron antineutrinos.

3. APPROXIMATE ANALYTIC SCALING RELATIONS

Following W.-X. Chen & A. M. Beloborodov (2007), B. D. Metzger et al. (2008b,a), D. M. Siegel et al. (2019), S. De & D. M. Siegel (2021), D. M. Siegel (2022), A. Agarwal et al. (2025), we define various physical regimes of neutrino-cooled accretion. Below we derive approximate scaling relations that prove useful in the analysis of numerical results (Section 5), based on the relativistic disk model laid out in Section 2.

3.1. Ignition threshold

Whereas photons are trapped in the accretion flow across all regimes of interest in this paper, neutrinos may efficiently cool the plasma once it dissociates into individual nucleons and becomes sufficiently dense. We refer to the physical state in which cooling through weak interactions, predominantly electron and positron capture ($e^- + p \rightarrow n + \nu_e$; $e^+ + n \rightarrow p + \bar{\nu}_e$), balance viscous heating of the accretion flow as the “ignition threshold”.

The local disk density is given by (combine Equations (8), (11), and (17))

$$\rho = \frac{S}{4\pi J^{1/2}} \left(\frac{H}{r} \right)^{-3} r^{-\frac{3}{2}} \alpha^{-1} M_\bullet^{-\frac{1}{2}} \dot{M}. \quad (50)$$

Assuming that $p \propto T^4$, the disk temperature is obtained from vertical equilibrium (Equation (11)):

$$T \propto J^{\frac{1}{4}} \left(\frac{H}{r} \right)^{\frac{1}{2}} r^{-\frac{1}{4}} \rho^{\frac{1}{4}} M_\bullet^{\frac{1}{4}}. \quad (51)$$

At the ignition threshold, radiation pressure (Equation (B57)) and relativistic e^\pm pressure (cf. Equation (B64) for the ultra-relativistic case) dominate (Section 5.6), making $p \propto T^4$ a well justified assumption.

Furthermore, we make the assumption that electron and positron capture are the dominant cooling channels at the ignition threshold, and that the flow is still optically thin to neutrinos: $F^- \propto H \rho T^6$ (see Equations (34), (35)). Using Equation (51) to replace the temperature and Equation (50) to replace the density, we obtain

$$F^- \propto J^{\frac{1}{4}} S^{\frac{5}{2}} \left(\frac{H}{r} \right)^{-\frac{7}{2}} r^{-\frac{17}{4}} \alpha^{-\frac{5}{2}} M_\bullet^{\frac{1}{4}} \dot{M}^{\frac{5}{2}}. \quad (52)$$

Combining the last expression with Equation (14) for viscous heating F^+ , we find

$$\frac{F^-}{F^+} \propto J^{\frac{1}{4}} S^{\frac{3}{2}} \frac{\mathcal{C}^2}{\mathcal{D}^2} \left(\frac{H}{r} \right)^{-\frac{7}{2}} r^{-\frac{5}{4}} \alpha^{-\frac{5}{2}} M_\bullet^{-\frac{3}{4}} \dot{M}^{\frac{3}{2}}. \quad (53)$$

We define the ignition threshold by the condition $F^-/F^+ = 0.5 = \text{const.}$, at which $H/r \approx \text{const.}$ (since $H/r \sim \mathcal{O}(1)$ when advective cooling dominates), and find that the radius interior to which neutrino cooling becomes significant (the “ignition radius”) scales as

$$r_{\text{ign}} \propto J^{\frac{1}{5}} S^{\frac{6}{5}} \frac{\mathcal{C}^{\frac{8}{5}}}{\mathcal{D}^{\frac{8}{5}}} \alpha^{-2} M_\bullet^{-\frac{3}{5}} \dot{M}^{\frac{6}{5}}. \quad (54)$$

Neglecting the general-relativistic structure functions and normalizing to the gravitational radius, one approximately has

$$\frac{r_{\text{ign}}}{r_g} \propto \alpha^{-2} M_\bullet^{-\frac{8}{5}} \dot{M}^{\frac{6}{5}}. \quad (55)$$

The neutrino-cooled region of a disk thus decreases in radial size with increasing viscosity or black hole mass, whereas it grows in size with increasing accretion rate.

The requirement for a neutrino-cooled region of the accretion flow to exist ($r_{\text{ign}} \geq r_{\text{ISCO}}$) translates into a minimum accretion rate ($\dot{M} \geq \dot{M}_{\text{ign}}$; the “ignition threshold” accretion rate),

$$\dot{M}_{\text{ign}} \propto \alpha^{\frac{5}{3}} M_\bullet^{\frac{4}{3}}, \quad (56)$$

where we have used $r_{\text{ISCO}} \propto r_g \propto M_\bullet$ in Equation (55). This result has been derived in a similar way by S. De & D. M. Siegel (2021) and agrees with the analogous Newtonian result (D. M. Siegel 2022; A. Agarwal et al. 2025).

The ratio of radiation and/or relativistic e^\pm pressure to baryon pressure at the ignition threshold ($r = r_{\text{ign}}$) increases moderately as a function of black hole mass

and α -viscosity at a given accretion rate \dot{M} (using Equations (50) and (51)):

$$\left. \frac{p_\gamma}{p_b} \right|_{r_{\text{ign}}} \propto \left. \frac{T^3}{\rho} \right|_{r_{\text{ign}}} \propto \alpha M_\bullet^{\frac{11}{10}} \dot{M}^{-\frac{7}{10}}. \quad (57)$$

At $\dot{M} = \dot{M}_{\text{ign}}$, one finds with Equation (56)

$$\left. \frac{p_\gamma}{p_b} \right|_{\dot{M}_{\text{ign}}} \propto \left. \frac{T^3}{\rho} \right|_{\dot{M}_{\text{ign}}} \propto \alpha^{-\frac{1}{6}} M_\bullet^{\frac{1}{6}}. \quad (58)$$

3.2. Neutrino opaque threshold

Above a critical density, the accretion flow becomes opaque to neutrinos and optically thin cooling transitions to optically thick cooling. The vertical optical depth for electron neutrinos or antineutrinos through the disk with opacity κ scales as

$$\tau_\nu \propto \rho \kappa H \propto \rho T^2 H, \quad (59)$$

where we have used that the cross section depends quadratically on temperature, $\sigma \propto T^2$, for all relevant sources of opacity (absorptions by nucleons, elastic scattering off baryons, scattering off electrons and positrons).

As discussed in Secs. 5.6 (Figs. 6 and 7), the pressure at the transition radius r_ν to the optically thick regime is dominated by baryon pressure for sufficiently small black hole masses $M_\bullet \lesssim 100 M_\odot$ and sufficiently small values of the viscosity $\alpha \lesssim 0.1$, in which case $p \propto p_b \propto \rho T$ in Equation (11) leads to

$$T \propto J \left(\frac{H}{r} \right)^2 r^{-1} M_\bullet, \quad (60)$$

in lieu of Equation (51). However, for large black hole masses and values of α , Equation (51) applies. Combining Equations (50), (51), (59), and (60), we obtain

$$\tau_{\nu_e} \propto \begin{cases} J^{\frac{3}{2}} S \left(\frac{H}{r} \right)^2 r^{-\frac{5}{2}} \alpha^{-1} M_\bullet^{\frac{3}{2}} \dot{M}, & p \propto p_b \\ J^{-\frac{1}{4}} S^{\frac{3}{2}} \left(\frac{H}{r} \right)^{-\frac{5}{2}} r^{-\frac{7}{4}} \alpha^{-\frac{3}{2}} M_\bullet^{-\frac{1}{4}} \dot{M}^{\frac{3}{2}}, & p \propto p_{\gamma, e^\pm} \end{cases}. \quad (61)$$

The accretion flow thus becomes opaque ($\tau_{\nu_e} \geq 1$) to neutrinos interior to a radius

$$r_\nu \propto \begin{cases} J^{\frac{3}{2}} S^{\frac{2}{5}} \left(\frac{H}{r} \right)^{\frac{4}{5}} \alpha^{-\frac{2}{5}} M_\bullet^{\frac{3}{5}} \dot{M}^{\frac{2}{5}}, & p \propto p_b \\ J^{-\frac{1}{7}} S^{\frac{6}{7}} \left(\frac{H}{r} \right)^{-\frac{10}{7}} \alpha^{-\frac{6}{7}} M_\bullet^{-\frac{1}{7}} \dot{M}^{\frac{6}{7}}, & p \propto p_{\gamma, e^\pm} \end{cases}, \quad (62)$$

which upon setting $H/r \sim \text{const.}$ as above and neglecting the general-relativistic structure functions J and S , yields the approximate result

$$\frac{r_\nu}{r_g} \propto \begin{cases} \alpha^{-\frac{2}{5}} M_\bullet^{-\frac{2}{5}} \dot{M}^{\frac{2}{5}}, & p \propto p_b \\ \alpha^{-\frac{6}{7}} M_\bullet^{-\frac{8}{7}} \dot{M}^{\frac{6}{7}}, & p \propto p_{\gamma, e^\pm} \end{cases}. \quad (63)$$

For such an optically thick region of the accretion flow to exist ($r_\nu \geq r_{\text{ISCO}}$), the accretion rate must be above the critical value

$$\dot{M}_\nu \propto \begin{cases} \alpha M_\bullet, & p \propto p_b \\ \alpha M_\bullet^{\frac{4}{3}}, & p \propto p_{\gamma, e^\pm} \end{cases}, \quad (64)$$

which one obtains from Equation (63) using $r_{\text{ISCO}} \propto r_g \propto M_\bullet$ as above. Analogous relations $r_{\bar{\nu}}$ and $\dot{M}_{\bar{\nu}}$ hold for electron antineutrinos, which only differ in their absolute normalization.

We expect the transition between the two pressure regimes considered above to be gradual as a function of the free parameters of the problem. Indeed, from the above expressions (Equation (50), (51), (60)), we find that the ratio $p_{\gamma, e^\pm}/p_b$ at the neutrino opaque threshold ($r = r_\nu$) increases moderately as a function of black hole mass and α -viscosity at a given accretion rate \dot{M} :

$$\left. \frac{p_\gamma}{p_b} \right|_{r_\nu} \propto \left. \frac{T^3}{\rho} \right|_{r_\nu} \propto \begin{cases} \alpha^{\frac{8}{5}} M_\bullet^{\frac{13}{5}} \dot{M}^{-\frac{8}{5}}, & p \propto p_b \\ \alpha^{\frac{4}{7}} M_\bullet^{\frac{13}{14}} \dot{M}^{-\frac{4}{7}}, & p \propto p_{\gamma, e^\pm} \end{cases}. \quad (65)$$

At $\dot{M} = \dot{M}_\nu$, one finds with Equation (64)

$$\left. \frac{p_\gamma}{p_b} \right|_{\dot{M}_\nu} \propto \left. \frac{T^3}{\rho} \right|_{\dot{M}_\nu} \propto \begin{cases} \alpha^0 M_\bullet, & p \propto p_b \\ \alpha^0 M_\bullet^{\frac{1}{6}}, & p \propto p_{\gamma, e^\pm} \end{cases}. \quad (66)$$

3.3. Neutrino trapping threshold

Another characteristic accretion regime emerges when neutrinos become trapped in the accretion flow and are advected into the black hole. This occurs when the local vertical diffusion time of neutrinos through the disk, $t_{\text{diff}} \sim (H/c)\tau_{\nu_e}$, becomes greater than the local accretion time

$$t_{\text{acc}} = \int_0^r \frac{dl}{V}, \quad (67)$$

where $dl = \sqrt{g_{rr}} dr$ is the proper radial distance element and $V = \tilde{v}/\sqrt{1 + \tilde{v}^2}$, with $\tilde{v}^2 \equiv u^r u_r = g_{rr} |u^r|^2$, is the radial fluid velocity in a co-rotating frame at radius r . Using $|u^r| \ll |u^\phi| \sim 1$, the above condition translates into

$$\tau_\nu \gtrsim \frac{c}{|u^r|} \left(\frac{H}{r} \right)^{-1}. \quad (68)$$

Making use of Equation (8), we find that trapping occurs within a radius

$$r_{\nu\text{-trap}} \propto \begin{cases} J^{\frac{2}{3}} \left(\frac{H}{r} \right)^{\frac{5}{3}} \alpha^0 M_\bullet^{\frac{2}{3}} \dot{M}^{\frac{1}{3}}, & p \propto p_b \\ J^{\frac{1}{9}} S^{\frac{2}{9}} \left(\frac{H}{r} \right)^{\frac{2}{9}} \alpha^{-\frac{2}{9}} M_\bullet^{\frac{1}{9}} \dot{M}^{\frac{2}{3}}, & p \propto p_{\gamma, e^\pm} \end{cases}. \quad (69)$$

Assuming $H/r \sim \text{const.}$ as before and dropping the general-relativistic structure functions, one finds approximately

$$\frac{r_{\nu\text{-trap}}}{r_g} \propto \begin{cases} \alpha^0 M_\bullet^{-\frac{1}{3}} \dot{M}^{\frac{1}{3}}, & p \propto p_b \\ \alpha^{-\frac{2}{9}} M_\bullet^{-\frac{8}{9}} \dot{M}^{\frac{2}{3}}, & p \propto p_{\gamma, e^\pm} \end{cases}. \quad (70)$$

From this expression we deduce that for a neutrino trapped regime to exist ($r_{\nu\text{-trap}} \geq r_{\text{ISCO}}$), the accretion rate must exceed the critical value

$$\dot{M}_{\nu\text{-trap}} \propto \begin{cases} \alpha^0 M_\bullet, & p \propto p_b \\ \alpha^{\frac{1}{3}} M_\bullet^{\frac{4}{3}}, & p \propto p_{\gamma,e^\pm} \end{cases}, \quad (71)$$

where we have again used the fact that $r_{\text{ISCO}} \propto r_g \propto M_\bullet$. Analogous relations $r_{\bar{\nu}\text{-trap}}$ and $\dot{M}_{\bar{\nu}\text{-trap}}$ hold for electron antineutrinos, which only differ in their absolute normalization.

The ratio of radiation and/or relativistic e^\pm pressure to baryon pressure at the neutrino trapping threshold ($r = r_{\nu\text{-trap}}$) increases moderately as a function of black hole mass and α -viscosity at a given accretion rate \dot{M} (combining Equations (50), (51), (60), and (69)):

$$\left. \frac{p_\gamma}{p_b} \right|_{r_{\nu\text{-trap}}} \propto \left. \frac{T^3}{\rho} \right|_{r_{\nu\text{-trap}}} \propto \begin{cases} \alpha M_\bullet^{\frac{5}{2}} \dot{M}^{-\frac{3}{2}}, & p \propto p_b \\ \alpha^{\frac{1}{3}} M_\bullet^{\frac{5}{6}} \dot{M}^{-\frac{1}{2}}, & p \propto p_{\gamma,e^\pm} \end{cases} \quad (72)$$

At $\dot{M} = \dot{M}_{\nu\text{-trap}}$, we find with Equation (71)

$$\left. \frac{p_\gamma}{p_b} \right|_{\dot{M}_{\nu\text{-trap}}} \propto \left. \frac{T^3}{\rho} \right|_{\dot{M}_{\nu\text{-trap}}} \propto \begin{cases} \alpha M_\bullet, & p \propto p_b \\ \alpha^{\frac{1}{6}} M_\bullet^{\frac{1}{6}}, & p \propto p_{\gamma,e^\pm} \end{cases}. \quad (73)$$

4. NUMERICAL DISK MODEL SOLVER

The structure and thermodynamic state of the accretion disk at a given radius can be entirely determined from the local values of the three independent quantities Y_e , θ and η_e . Employing these as independent variables to integrate the disk structure equations has the benefit that θ and η_e are direct arguments of the Fermi function and that all three quantities are of order unity in the regimes of interest to be explored here numerically.

Due to the complications arising from various Fermi integrals, it is not possible to integrate the disk structure equations explicitly with standard techniques. Instead, similar to but somewhat different from [W.-X. Chen & A. M. Beloborodov \(2007\)](#), we integrate Equations (9) and (12), together with the constraint equation

$$p(r) = \left(\frac{G\dot{M}M_\bullet S(r)J(r)}{4\pi\alpha r^3} \right)^{2/3} \rho(r)^{1/3}, \quad (74)$$

which is obtained by combining Equations (8), (11) and (17).

Choosing suitable boundary conditions at the outermost radius (see below), we discretize the radial domain $[r_{\text{in}}, r_{\text{out}}]$ with $N + 1$ points $\{r_N = r_{\text{ISCO}}, r_{N-1}, \dots, r_1, r_0 = r_{\text{out}}\}$ and integrate the above equations from the outside in, starting at $r_{[0]} = r_{\text{out}}$. At each radial step i , given $Y_{e[i]}$, $\theta_{[i]}$ and $\eta_{e[i]}$, we compute all dependent quantities and find $Y_{e[i+1]}$, $\theta_{[i+1]}$,

and $\eta_{e[i+1]}$ at the next radial step by solving a three-dimensional minimization problem to minimize the error function

$$\mathcal{L}_{\text{Error}}(Y_{e[i+1]}, \theta_{[i+1]}, \eta_{e[i+1]}) = \sqrt{e_1^2 + e_2^2 + e_3^2}. \quad (75)$$

The normalized (relative) error terms correspond to the algebraic,

$$e_1(Y_{e[i+1]}, \theta_{[i+1]}, \eta_{e[i+1]}) = p_{[i]}^{-1} \left[p_{[i+1]} - \left(\frac{G\dot{M}M_\bullet S(r)J(r)}{4\pi\alpha r^3} \right)^{2/3}_{[i+1]} \rho_{[i+1]}^{1/3} \right], \quad (76)$$

and differential equations to be solved,

$$e_2(Y_{e[i+1]}, \theta_{[i+1]}, \eta_{e[i+1]}) = (eH)_{[i]}^{-1} \times \left[(eH)_{[i+1]} - (eH)_{[i]} - (r_{[i+1]} - r_{[i]}) \times \left\{ \left(\frac{F^+ - F^-}{ur} \right)_{[i+1]} + \left(\frac{e+p}{\rho} \right)_{[i+1]} \frac{(\rho H)_{[i+1]} - (\rho H)_{[i]}}{r_{[i+1]} - r_{[i]}} \right\} \right], \quad (77)$$

$$e_3(Y_{e[i+1]}, \theta_{[i+1]}, \eta_{e[i+1]}) = (Y_{e[i]})^{-1} \times \left[Y_{e[i+1]} - Y_{e[i]} - \frac{m_p}{\rho_{[i]}} (r_{[i+1]} - r_{[i]}) \times \left\{ \left(\frac{\dot{n}_{\bar{\nu}_e} - \dot{n}_{\nu_e}}{Hu^r} \right)_{[i]} + (n_{\nu_e} - n_{\bar{\nu}_e})_{[i]} \frac{\log(\rho_{[i+1]}) - \log(\rho_{[i]})}{r_{[i+1]} - r_{[i]}} - \frac{(n_{\nu_e} - n_{\bar{\nu}_e})_{[i+1]} - (n_{\nu_e} - n_{\bar{\nu}_e})_{[i]}}{r_{[i+1]} - r_{[i]}} \right\} \right] \quad (78)$$

Here, we have discretized radial derivatives using first-order forward finite differences. With the resulting parameters $Y_{e[i+1]}$, $\theta_{[i+1]}$, and $\eta_{e[i+1]}$ that minimize Equation (75), all dependent quantities at $r_{[i+1]}$ are computed and the scheme is repeated at the next radial step $r_{[i+1]}$. Our solver makes use of the limited Broyden–Fletcher–Goldfarb–Shanno bounded algorithm routine of `Scipy` ([P. Virtanen et al. 2020](#)) to minimize the error function (75). To ensure stability of the scheme, we implement adaptive brackets that restrict Y_e , θ , and η_e to vary by less than 5% between consecutive radial steps. Our three-dimensional root-finding scheme differs from the approach of [W.-X. Chen & A. M. Beloborodov \(2007\)](#), who only needed to perform two-dimensional root finding in θ and η_e , due to a simplified evolution equation for the electron-fraction.

The boundary conditions are chosen at $r_{\text{out}} = 2000r_g$. This distance from the black hole is sufficient to completely cover the neutrino-cooled region of the disk. In

the outermost region of the numerical solution, the accretion flow is radiatively inefficient, energy transport is advection dominated, and the plasma is predominantly composed of α -particles and only of a small number of free nucleons. Therefore, an initial value for the proton-to-baryon ratio of $Y_e(r_{\text{out}}) = 0.5$ is well justified. In the advective flow, thermal energy is virialized, such that the specific internal energy density approximately equals the specific virial energy,

$$\frac{e}{\rho} = \frac{1}{2} \frac{GM_\bullet}{r}. \quad (79)$$

The initial values $\theta_{[0]}$ and $\eta_{e[0]}$ at $r = r_{\text{out}}$ are computed such that they simultaneously satisfy Equations (79) and (74).

Other boundary conditions characterizing an advective accretion flow, such as a specific ratio of H/r , could be specified instead. The numerical results obtained in the regime of interest here, $r_{\text{ISCO}} < r \sim r_{\text{ign}}$, however, are insensitive to the details of the outer boundary conditions specified in the advective part of the accretion flow.

At sufficiently large radii, the accretion flow becomes gravitationally unstable. For a Keplerian disk in Newtonian gravity, the instability sets in where (A. Toomre 1964; B. Paczynski 1978; C. F. Gammie 2001)

$$Q_{\text{grav}} = \frac{c_s \Omega}{2\pi G H \rho} \simeq \frac{H}{r} \frac{M_\bullet}{M_{\text{disk}}(r)} < 1. \quad (80)$$

Here, $M_{\text{disk}}(r)$ is the cumulative disk mass. We monitor this criterion when computing the numerical disk solutions. Whereas our disk model and numerical algorithm still lead to solutions in this regime, these become physically questionable, since self-gravity of the accretion flow would need to be taken into account and the onset of gravito-turbulence would lead to non-stationary, non-axisymmetric dynamics that also modifies (increases) the effective α -viscosity (C. F. Gammie 2001).

5. NUMERICAL RESULTS

5.1. Survey of parameter space

The one-dimensional disk model described in the previous sections allows us to scan the vast parameter space of steady-state, neutrino-cooled accretion onto black holes from the lightest stellar-mass black holes to intermediate-mass black holes, without the need for detailed, computationally expensive, three-dimensional magnetohydrodynamic simulations. Figures 1 and 2 present exemplary results of a parameter space survey in terms of several characteristic quantities, in the case of an α -viscosity of $\alpha = 0.063$, a value similar to effective α -viscosities arising in general-relativistic magnetohydrodynamic simulations of neutrino-cooled accretion disks

(e.g., D. M. Siegel & B. D. Metzger 2018; R. Fernández et al. 2019; D. M. Siegel et al. 2019; S. De & D. M. Siegel 2021; A. Agarwal et al. 2025). Another reason for the choice of this fiducial value of α is the fact that a wide range of qualitatively different behaviors of disk solutions can be illustrated in this case (see the following subsections).

All panels of Figures 1 and 2 show rest-mass averages of characteristic quantities ψ within the innermost 20 gravitational radii, defined as

$$\langle \psi \rangle = \frac{\int_{r_{\text{ISCO}}}^{20r_g} \psi(r) \rho(r) \sqrt{-g} \, dr}{\int_{r_{\text{ISCO}}}^{20r_g} \rho(r) \sqrt{-g} \, dr}, \quad (81)$$

with $\sqrt{-g} = r$ in our coordinates $x^\mu = (t, r, \phi, z)$. White (unpopulated) space in the figure panels corresponds to regions of the parameter space that are not of interest for the present discussion. The inner region of a few tens of gravitational radii focused on here is most characteristic of the physical state of the accretion flow. Additionally, being deepest in the gravitational potential, this region shows a sharp rise in temperature, which causes an imbalance between viscous heating and neutrino cooling off the midplane, leading to massive disk outflows, in which nucleosynthesis takes place (D. M. Siegel & B. D. Metzger 2018; D. M. Siegel et al. 2019). Such outflows are not considered in the present model. However, the disk composition sets a lower limit of Y_e for the composition of the outflows. As long as reabsorption of neutrinos from the accretion disk by the outflowing plasma winds can be neglected (typically for $\dot{M} \lesssim \dot{M}_\nu$), the disk wind composition is expected to be approximately that of the disk material from which the winds originate. Because of the relevance for nucleosynthesis, here we focus chiefly on the disk composition.

At sufficiently small accretion rates $\dot{M} \ll \dot{M}_{\text{ign}}$, the composition remains unchanged ($Y_e \simeq 0.5$) with respect to the outer boundary condition of the accretion flow. We find a proton-rich regime $Y_e \gtrsim 0.5$ at accretion rates close to the ignition threshold $\dot{M} \lesssim \dot{M}_{\text{ign}}$, at least with increasing black hole mass ($M_\bullet \gtrsim 10M_\odot$). Between $\dot{M}_{\text{ign}} \lesssim \dot{M} \lesssim \dot{M}_{\nu\text{-opaque}}$, a pronounced valley of very neutron-rich composition of $Y_e \lesssim 0.1 - 0.2$ emerges, with an increasing valley floor as M_\bullet increases. At $\dot{M} \gtrsim \dot{M}_{\nu\text{-trap}}$, the valley floor rises to larger values of $Y_e \lesssim 0.3 - 0.5$, which confine the valley floor ‘from above’. In the following subsections, we discuss these main features and qualitatively different regimes of disk composition in more detail.

5.2. The neutron-rich regime

As the accretion rate exceeds the ignition threshold $\dot{M} \gtrsim \dot{M}_{\text{ign}}$, the inner accretion flow starts to neutronize

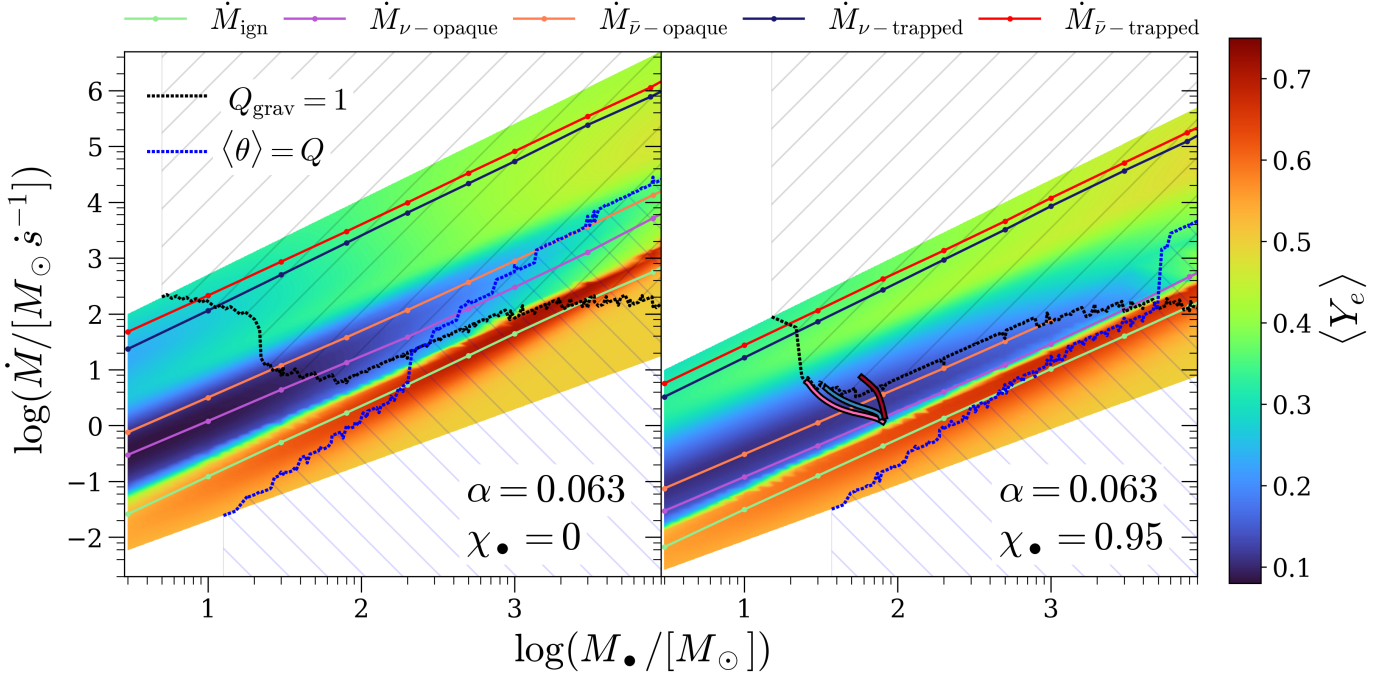


Figure 1. Mass averaged proton-fraction $\langle Y_e \rangle$ in the inner part of the disk ($r \leq 20r_g$) for accretion flows around non-spinning ($\chi_\bullet = 0$; left) and rapidly spinning ($\chi_\bullet = 0.95$; right) black holes with $\alpha = 0.063$ as a function of black hole mass M_\bullet and accretion rate \dot{M} . Dots connected by solid lines delineate the numerically identified accretion regimes (Secs. 3, 5.7). A valley of very neutron-rich disk composition ($Y_e \lesssim 0.1 - 0.2$) is apparent for accretion rates between \dot{M}_{ign} and $\dot{M}_{\bar{\nu}\text{-opaque}}$. The hashed region above the black dotted line corresponds to gravitationally unstable disks ($Q_{\text{grav}}(r = 20r_g) < 1$; Equation (80)). The hashed region below the blue dotted line marks disks that do not reach an average temperature larger than the proton-neutron mass difference ($\langle \theta \rangle(r \leq 20r_g) < Q = 2.531$). The pink, green, and red solid lines in the right panel indicate the approximate time evolution of collapsar accretion processes in super-kilonova events leading to final black holes in the pair instability supernova mass gap (see Section 6.2; D. M. Siegel et al. 2022).

(Figures 1, 4). This is a result of the midplane density (Equation (50)) increasing to a level at which electrons become degenerate, such that $\eta_e \lesssim 1$ (compare, for example, the blue and red lines in Figure 4 (II)). Figure 2 (I) also clearly shows the increase of η_e to order unity at $\dot{M} \gtrsim \dot{M}_{\text{ign}}$. As a result of Pauli-blocking, e^\pm -pair creation is suppressed and electron capture onto protons (Equation (25)) is increasingly favored over positron capture onto neutrons (Equation (26)), driving the accretion flow into a neutron-rich state ($Y_e < 0.5$).

neutrino cooling is indeed typically dominated by electron and positron capture at all characteristic accretion rates (Figure 2 (IV)). Generally, the ratio $F_{\text{annihilation}}^-/F_{e^\pm\text{-capture}}^-$ is expected to scale as (see Equations (58), (66) and (73))

$$\frac{F_{\text{annihilation}}^-}{F_{e^\pm\text{-capture}}^-} \propto \frac{p_{\gamma, e^\pm}}{p_b} \propto \begin{cases} \alpha^{-1/6} M_\bullet^{1/6}, & \dot{M} = \dot{M}_{\text{ign}} \\ \alpha^0 M_\bullet, & \dot{M} = \dot{M}_{\nu, \bar{\nu}} \\ \alpha^{-1/6} M_\bullet^{1/6}, & \dot{M} = \dot{M}_{\nu, \bar{\nu}\text{-trap}} \end{cases} \quad (82)$$

where we have assumed that radiation and relativistic electron-positron (e^\pm) pressure dominate at \dot{M}_{ign} , whereas baryon pressure dominates at all other thresh-

olds (Figure 2 (III) and Section 5.6). This increase of the pressure ratio with M_\bullet can indeed be observed in Figure 2 (III), but the ratio of cooling emissivities only increases to order unity at $\dot{M} \approx \dot{M}_{\text{ign}}$ for large black hole masses $M_\bullet \gtrsim 1000M_\odot$ (lower right corner of Figure 2 (IV)), where this affects the composition (Sec. 5.4). The onset of strong neutrino cooling is also reflected in the entropy per baryon and k_B , which shows a characteristic drop from typically $\langle s \rangle \gtrsim 30 - 100$ at $\dot{M} \lesssim \dot{M}_{\text{ign}}$ to $\langle s \rangle \approx 10 - 20$ at $\dot{M} \gtrsim \dot{M}_{\text{ign}}$ (Figure 2 (V)).

As the accretion rate surpasses \dot{M}_{ign} and approaches \dot{M}_ν , we find that the inner part of the disk regulates itself to a low- Y_e state of $Y_e \approx 0.05 - 0.1$ (Figures 1, 3, and 4). The existence of such a well-defined ‘asymptotic’ value of Y_e across the wide parameter space of accretion flows considered here, which is particularly evident from Figures 3 and 4, is the result of a self-regulation mechanism based on electron degeneracy acting in the accretion flow (W.-X. Chen & A. M. Beloborodov 2007; D. M. Siegel & B. D. Metzger 2018; D. M. Siegel et al. 2019): As η_e rises beyond unity due to increasing midplane densities (Figures 2 (I) and 3 (II)), suppression

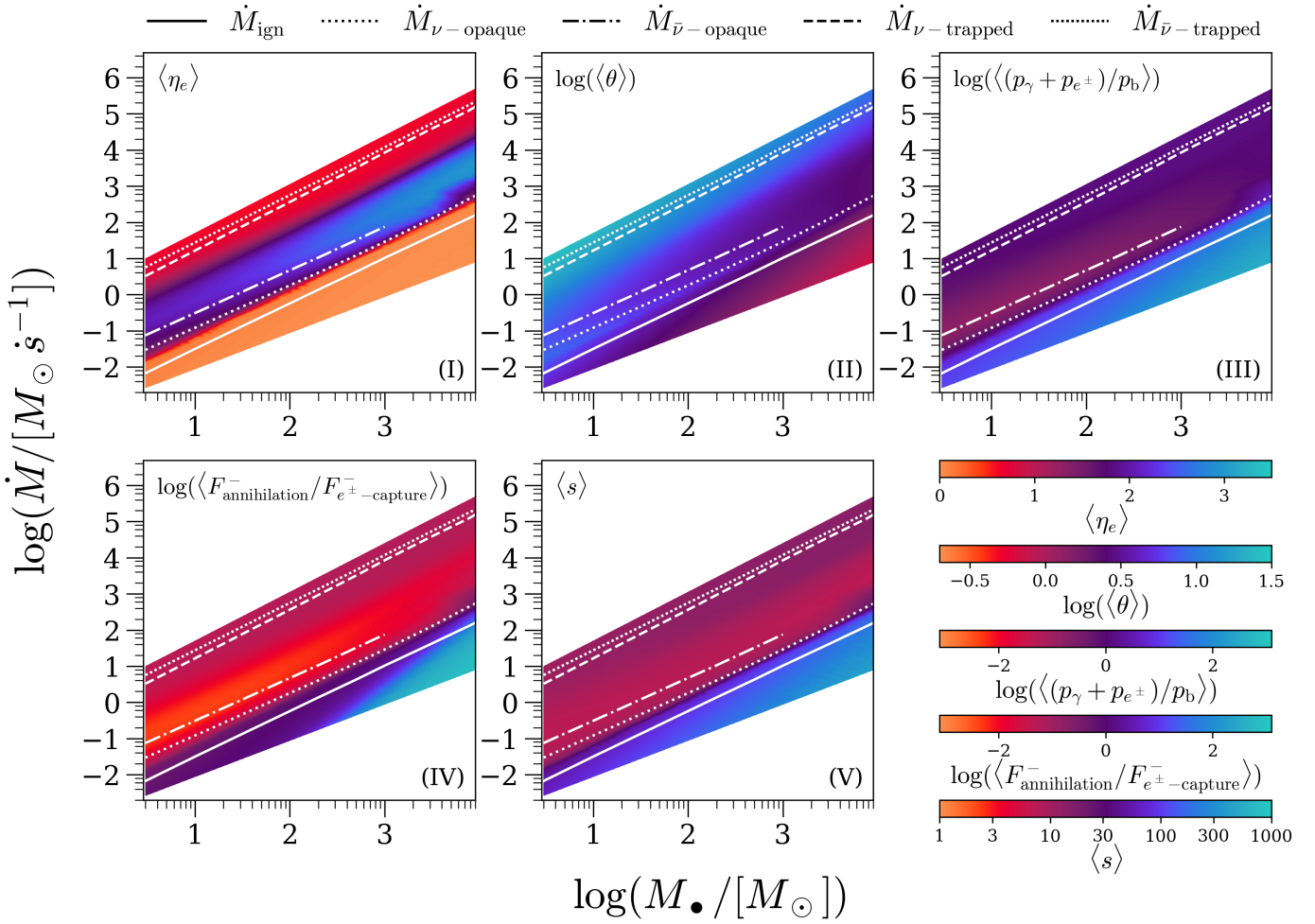


Figure 2. Parameter space results for rest-mass averaged electron degeneracy $\langle \eta_e \rangle$, temperature $\langle \theta \rangle$, radiation pressure to baryon pressure ratio $\langle (p_\gamma + p_{e^\pm})/p_b \rangle$, annihilation cooling to e^\pm -capture cooling ratio $\langle F_{\text{annihilation}}^-/F_{e^\pm\text{-capture}}^- \rangle$ and entropy per baryon in units of k_B , $\langle s \rangle$, for the case of fast-rotating black holes ($\chi_\bullet = 0.95$) with masses in the range $M_\bullet = 3 - 3.000 M_\odot$ and viscosity parameter $\alpha = 0.063$. Averages are taken in the inner part of the disk ($r \leq 20r_g$; Equation (81)). The colorbars are centered around characteristic values to delineate different physical regimes, in particular $\langle \theta \rangle = Q = 2.531$ to differentiate sufficiently hot disks that ignite weak interactions from those that do not strongly cool via neutrinos, as well as dominant regimes of pressure and neutrino cooling.

of e^\pm -pair creation sets in, which reduces the overall neutrino cooling through electron and positron capture (Equations (25) and (26)), leading to higher temperatures, reducing η_e . The result of this negative feedback loop is a regulated degeneracy level of $\eta_e \sim 1$ for $\dot{M} \gtrsim \dot{M}_{\text{ign}}$, as evident from Figures 2, 3 and 4. This self-regulated regime of the accretion flow based on electron degeneracy and temperature involves an intricate balance between neutrino cooling and viscous heating of the flow, which can be identified as a horizontal “plateau” of $F^-/F^+ \simeq 1$ in the radial profiles shown in Figures 3 (IV) and 4 (IV).

At sufficiently high disk densities and temperatures, an estimate for the self-regulated value of Y_e can be ob-

tained from Equation (28), which can be recast as

$$Y_e = \frac{1}{1 + e^{\eta_e - \eta_\nu - \frac{Q}{\theta}}} \approx \frac{1}{1 + e^{\eta_e}} \approx 0.07 - 0.18. \quad (83)$$

In the second step, we have assumed sufficiently high \dot{M} , such that temperatures increase to $Q/\theta \ll \text{few} \sim \eta_e$ (see Figure 2), and we neglected η_ν relative to $\eta_e \sim \text{few}$ (semi-transparent limit). From our numerical results, typically $1.5 \lesssim \eta_e \lesssim 2.6$, which yields $0.07 \lesssim Y_e \lesssim 0.18$. This rough estimate is in good agreement with the actual numerical results obtained in the stellar-mass black hole range. At black hole masses $M_\bullet \sim 100 - 1000 M_\odot$, however, disk temperatures decrease (typically $T \propto M_\bullet^{-1/6}$, see Equation (88) and Figure 2 (II)) and thus Y_e slowly increases with black hole mass until neutronization ceases to occur at $M_\bullet \gtrsim \text{few} \times 10^3 - 10^4 M_\odot$.

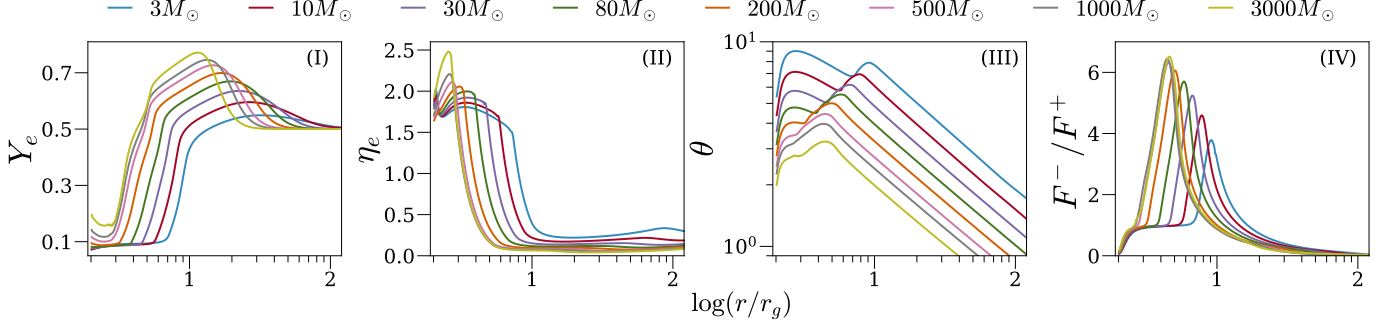


Figure 3. Radial profiles (in units of the gravitational radius r_g) of proton-fraction Y_e , the normalized electron degeneracy parameter $\eta_e = \mu_e/k_B T$, the normalized temperature $\theta = k_B T/m_e c^2$, and the ratio F^-/F^+ of the rate of neutrino cooling to viscous heating for accretion flows with $\alpha = 0.063$ at the neutrino opaque threshold $\dot{M} = \dot{M}_\nu$ around rapidly spinning ($\chi_\bullet = 0.95$) black holes across three orders of magnitude in mass.

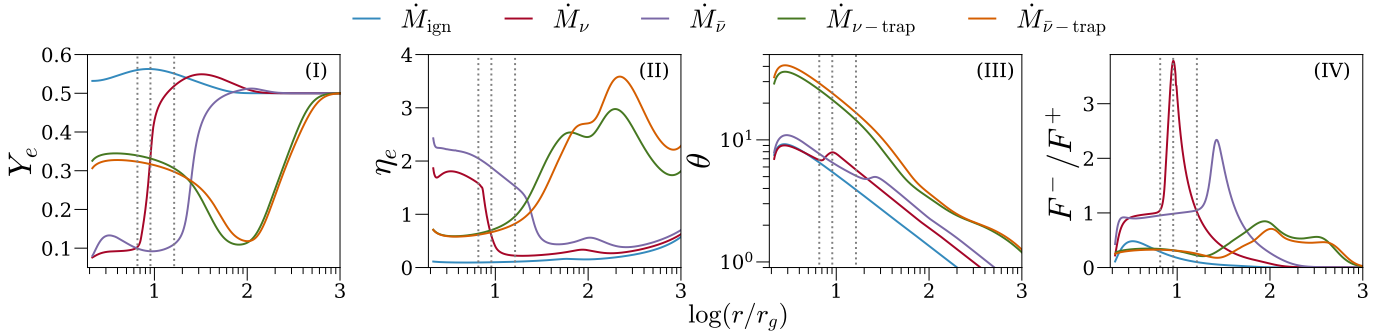


Figure 4. Radial profiles (in units of the gravitational radius r_g) of proton-fraction Y_e , the normalized electron degeneracy parameter $\eta_e = \mu_e/k_B T$, the ratio F^-/F^+ of the rate of neutrino cooling to viscous heating, and the normalized temperature $\theta = k_B T/m_e c^2$ for accretion flows with $\alpha = 0.063$ around a rapidly spinning ($\chi_\bullet = 0.95$) black hole of mass $M_\bullet = 3M_\odot$ at various characteristic accretion rates (Section 3). Vertical dotted lines indicate the radial range, in which the disk composition at $\dot{M} = \dot{M}_\nu$ transitions from the outer proton-rich to the inner neutron-rich regime.

The onset and ‘mechanics’ of the self-regulation mechanism can be directly witnessed over a radial range in the accretion disk. Figure 4 illustrates the situation by vertical dotted lines for an accretion disk around a rapidly spinning $M_\bullet = 3M_\odot$ black hole at $\dot{M} = \dot{M}_\nu$. From right to left, the vertical lines indicate where the efficiency of neutrino cooling relative to viscous heating, F^-/F^+ , transitions from < 1 to > 1 to $\simeq 1$. As the density and temperature of the disk plasma increase with decreasing radius, i.e. as matter gradually falls deeper into the gravitational potential (Figure 4 (IV)), neutrino cooling increases sharply, $F^- \propto \rho T^6$ (Equations (34), (35)); Figure 4 (III)), as does the electron degeneracy (Figure 4 (II)). Once degeneracy is established, $\eta_e \sim 1$ (central vertical dotted line), cooling through electron and positron capture declines heavily due to exponential suppression of e^\pm -pair production. As a result of this negative feedback, F^-/F^+ starts to decrease with decreasing radius after having reached a peak value and approaches $\simeq 1$, a regime, in which positive and neg-

ative feedback on neutrino emission are balanced (left vertical dotted line).

The height of the peak in F^-/F^+ strongly depends on the original proton excess ($Y_e > 0.5$; see also Section 5.4) at the radii where neutrino cooling becomes significant, and thus strongly depends both on \dot{M} (Figure 4 (IV)) and on M_\bullet (Figure 3 (IV)). With a larger proton excess, more electrons are available for capture, and thus higher levels of degeneracy (cf. Figure 4 (II), Figure 3 (II)) can be tolerated before neutrino cooling becomes strongly suppressed.

Once F^-/F^+ decreases to $\simeq 1$ with decreasing radius, the self-regulated regime (with its well defined, small value of Y_e ; see above and Figures 3 (I) and 4 (I)) extends down to $r \simeq r_{\text{ISCO}}$. The existence and extend of this low- Y_e region is of pivotal importance in estimating whether given accretion flow regimes can give rise to r -process nucleosynthesis. The size is indicative of the amount of material unbound in disk winds, which, given the typical accretion disk wind conditions, are promising sites for r -process nucleosynthesis.

The radial range r_{sr} of this self-regulated region is governed by $F^-/F^+ \simeq \text{const.} \simeq 1$, and scales with α , \dot{M} , and M_\bullet . The scaling is identical to that of the ignition radius r_{ign} (Equation (55)) if the pressure at r_{sr} is dominated by radiation and/or relativistic e^\pm pressure. If the pressure is dominated by baryon pressure, however, one must follow the derivation in Section 3.1 with $p \propto \rho T$ to obtain the combined result:

$$\frac{r_{\text{sr}}}{r_g} \propto \begin{cases} \alpha^{-2} M_\bullet^{-\frac{8}{5}} \dot{M}^{\frac{6}{5}}, & p \propto p_{\gamma, e^\pm} \\ \alpha^{-\frac{2}{7}} M_\bullet^{\frac{2}{7}} \dot{M}^0, & p \propto p_b \end{cases} \quad (84)$$

At $r = r_{\text{sr}}$, the accretion flow transitions from the radiation and e^\pm -pressure dominated regime at $r = r_{\text{ign}}$ to an increasingly baryon-pressure dominated regime. One thus expects r_{sr} to scale somewhere in between the corner cases of Equations (84). For example, for the models shown in Figures 3 and 4, with $\alpha = 0.063$ and $\chi_\bullet = 0.95$, we find

$$\frac{r_{\text{sr}}}{r_g} \propto \dot{M}^{0.95 \pm 0.09} M_\bullet^{-0.64 \pm 0.01}, \quad (85)$$

which is indeed within the limits found in Equation (84).

As the accretion rate approaches $\dot{M} \approx \dot{M}_{\nu\text{-trap}}$ and neutrinos become trapped in the inner part of the accretion flow, the reverse reaction in Equation (25) is enhanced relative to that of Equation (26). This is because neutrons are more abundant than protons in the inner part of the accretion flow, which is neutronized at larger radii. The abundance of trapped neutrinos progressively increases the proton-fraction Y_e with increasing \dot{M} , until the latter reaches a typical value of $Y_e \approx 0.3 - 0.4$ at $\dot{M} \gtrsim \dot{M}_{\nu\text{-trap}}$, evidently present in Figures 1 and 4 (I). As the accretion flow neutronizes progressively less in the range $\dot{M}_{\text{ign}} \lesssim \dot{M} \lesssim \dot{M}_{\nu\text{-trap}}$ with increasing M_\bullet , so does Y_e also increase to $0.4 - 0.5$ at $\dot{M} \gtrsim \dot{M}_{\nu\text{-trap}}$ (Figure (1)).

5.3. Implications for nucleosynthesis of neutron-rich nuclei

Outflows from neutrino-cooled accretion disks have been demonstrated to be promising sources of r -process nuclei by three-dimensional GRMHD simulations in the stellar-mass regime $M_\odot \approx 3M_\odot$ (e.g., D. M. Siegel & B. D. Metzger 2017, 2018; R. Fernández et al. 2019; J. M. Miller et al. 2019; X. Li & D. M. Siegel 2021; D. M. Siegel et al. 2019; J. M. Miller et al. 2020). Given the results on neutronization in Section 5.2, here we briefly comment on the prospects for r -process nucleosynthesis more broadly across the vast parameter space of neutrino-cooled accretion onto black holes considered in this paper.

We estimate the relevant parameters determining the nucleosynthetic outcome of the r -process using a simple disk outflow model described in Appendix C. These are Y_e , s , and the expansion timescale τ_{exp} of the outflow at the onset the neutron-capture reactions (i.e. when the flow has cooled to ≈ 5 GK; J. Lippuner & L. F. Roberts 2015). In particular, we consider outflowing plasma ejected from the inner accretion disk at $R_{\text{launch}} = 3r_{\text{ISCO}}$ under the assumption of adiabatic expansion (constant entropy) and neglecting absorption of neutrinos during the launch of the outflows (constant Y_e). We focus on disks accreting at $\dot{M} \approx \dot{M}_\nu$, i.e. when the inner accretion flow is most neutron-rich (Section 5.2). We discard models with $\alpha \gtrsim 0.3$, because these disks do not reach the self-regulated regime.

The proton-fraction Y_e varies strongly with the black hole mass and α -viscosity (see Section 5.4). A larger M_\bullet or α -parameter lifts the equilibrium value reached in the self-regulated regime. For $\chi_\bullet = 0$ and $\alpha = 0.001 - 0.3$, we find $Y_e \approx 0.06 - 0.13$ at $M_\bullet = 3M_\odot$ and $Y_e \approx 0.32 - 0.36$ at $M_\bullet = 3000M_\odot$. For $\chi_\bullet = 0.95$ and $\alpha = 0.001 - 0.3$, instead, we find $Y_e \approx 0.03 - 0.13$ at $M_\bullet = 3M_\odot$ and $Y_e \approx 0.25$ at $M_\bullet = 3000M_\odot$.

The entropy of the outflowing trajectories generally resides in a narrow range of $s \sim 4 - 8k_B$ per baryon for $\alpha = 0.001 - 0.1$, $M_\bullet = 3 - 3000M_\odot$, and $\chi_\bullet = 0 - 0.95$, with only a slight increase with increasing α -viscosity.

The expansion timescale depends on both the ejecta velocity and the distance to the black hole when the r -process takes place (i.e. when the wind reaches $T \sim 5$ GK). The former depends only on Y_e (see Appendix C), and varies between $\sim 0.05 - 0.12c$, while the latter is proportional to the black hole mass and the spin, as these two quantities determine the value of the ISCO, and thus the absolute length scale at which the outflow is launched. For $\chi_\bullet = 0$, we find the expansion timescale approximately follows $\tau_{\text{exp}} \sim 35 \text{ ms} (M_\bullet/3M_\odot)^{0.72} (\alpha/0.063)^{0.13}$, while for $\chi_\bullet = 0.95$, it follows $\tau_{\text{exp}} \sim 18 \text{ ms} (M_\bullet/3M_\odot)^{0.72} (\alpha/0.063)^{0.19}$.

The conditions estimated above are generally conducive to the r -process. The main question remaining is whether only light or also heavy r -process elements (lanthanides and actinides) can be synthesized in the outflows. Comparing to the results of J. Lippuner & L. F. Roberts (2015), we find that, generally, outflows from the inner accretion disks at $\dot{M} \approx \dot{M}_\nu$ for $M_\bullet \lesssim 200M_\odot$ ($\chi_\bullet = 0$) and $\lesssim 500M_\odot$ ($\chi_\bullet = 0.95$) are sufficiently neutron-rich to produce significant mass fractions of lanthanides and actinides. Associated superkilonovae may thus appear ‘red’, with spectra peaking in the infrared due to the large line expansion opacities of the lanthanides and actinides. For larger black

hole masses, we conclude that outflows unlikely synthesize significant mass fractions of lanthanides or actinides. This is because either $Y_e \gtrsim 0.25$, the threshold for lanthanide production, or $Y_e < 0.25$, but the expansion timescales are $\tau_{\text{exp}} \gtrsim 0.5 - 10$ s, when late-time reheating from radioactive decays restarts the r -process at higher Y_e (J. Lippuner & L. F. Roberts 2015). Associated super-kilonovae would then appear as ‘blue’ transients, peaking in the optical.

5.4. The proton-rich regime

In the range of intermediate radii $r_\nu < r \lesssim r_{\text{ign}}$, in which the accreting matter resides in a non-degenerate to weakly degenerate regime, $\eta_e \ll 1$ or $\eta_e \lesssim 1$, but in which neutrino cooling via electron and positron capture (Equations (25) and (26)) still is energetically significant, the accretion flow may become proton rich ($Y_e > 0.5$). This is evident from the pronounced red and orange regions around the \dot{M}_{ign} threshold in Figure 1, as well as in the explicit examples of radial profiles across the $\approx 3 - 3000 M_\odot$ mass range in Figure 3 (I).

Proton excess in this physical regime is a result of the proton-neutron mass difference. In the presence of electron and positron capture under weakly degenerate conditions, $\eta_e \lesssim 1$, and in hot matter $\theta > Q = (m_n - m_p)/m_e \approx 2.531$ (that is, $T > 1.3$ MeV), the proton-fraction Y_e can be analytically estimated from Equations (40) and (41) as (cf. A. M. Beloborodov 2003; D. M. Siegel & B. D. Metzger 2018)

$$Y_e = 0.5 + 0.487 \left(\frac{Q}{2\theta} - \eta_e \right) \approx 0.5 + \frac{0.616}{\theta}, \quad (86)$$

where in the second step, we considered the non-degenerate limit $\eta_e \ll \theta$, in which, under conditions of approximately similar numbers of electrons and positrons, positron capture is energetically favored over electron capture, due to the positive mass difference Q between the neutron and the proton. However, a small degeneracy $\eta_e > Q/(2\theta)$ is sufficient to cause the accretion flow to turn neutron-rich ($Y_e < 0.5$; Section 5.2).

Under similar physical conditions of the accretion flow, i.e. for disks around varying black hole mass, but with accretion rates in a similar regime (e.g. $\dot{M} \approx \dot{M}_{\text{ign}}$ or $\dot{M} \approx \dot{M}_\nu$), the proton-rich regime becomes increasingly pronounced both in radial extent and in absolute value of Y_e with increasing black hole mass. Whereas a proton excess is mild and barely noticeable for stellar-mass black holes around $\sim 3M_\odot$ (cf. Figure 1, Figure 3 (I) and Figure 4 (I)), the corresponding radial region widens and reaches values of up to $Y_e \approx 0.8$ for $3000M_\odot$ black holes.

The increasing proton excess with increasing black hole mass can be understood analytically. For accreting

matter dominated by radiation and relativistic e^\pm pressure, as appropriate in the radial regime under consideration (see Section 5.6), Equations (50) and (51) predict the disk midplane temperature as

$$T \propto J^{\frac{1}{8}} S^{\frac{1}{4}} \left(\frac{H}{r} \right)^{-\frac{1}{4}} \left(\frac{r}{r_g} \right)^{-\frac{5}{8}} \alpha^{-\frac{1}{4}} M_\bullet^{-\frac{1}{2}} \dot{M}^{\frac{1}{4}}, \quad (87)$$

which using Equations (55), (56), (63), (64) translates into

$$T \propto \begin{cases} \alpha^{1/6} M_\bullet^{-1/6} & (\dot{M} \approx \dot{M}_{\text{ign}}, p \propto p_{\gamma, e^\pm}) \\ \alpha^0 M_\bullet^{-1/6} & (\dot{M} \approx \dot{M}_\nu, p \propto p_{\gamma, e^\pm}) \end{cases}. \quad (88)$$

Indeed, at $\dot{M} = \dot{M}_\nu$ the temperatures of our numerical results roughly scale as $\propto M_\bullet^{-1/6}$ in the range $10 \lesssim r/r_g \lesssim 100$ as illustrated in Figure 3 (III). The corresponding proton excess according to Equation (86) then scales as

$$Y_e - 0.5 \propto \begin{cases} \alpha^{-1/6} M_\bullet^{1/6} & (\dot{M} \approx \dot{M}_{\text{ign}}, p \propto p_{\gamma, e^\pm}) \\ \alpha^0 M_\bullet^{1/6} & (\dot{M} \approx \dot{M}_\nu, p \propto p_{\gamma, e^\pm}) \end{cases} \quad (89)$$

At $\dot{M} = \dot{M}_\nu$ and a maximum Y_e of ≈ 0.55 for a $3M_\odot$ black hole, this scaling predicts a range of $Y_e \approx 0.55 - 0.7$ for $M_\bullet = 3 - 3000 M_\odot$. This estimate is in good agreement with the numerical results shown in Figure 3 (I).

5.5. Implications for nucleosynthesis of proton-rich nuclei

The presence of proton-rich regimes in the accretion flow (Sec. 5.4) gives rise to proton-rich disk outflows from these regions. Here, we estimate, using a simplified disk outflow model, whether such outflows can synthesize neutron-deficient nuclei (p -nuclei) via the νp -process.

The νp -process (C. Fröhlich et al. 2006; S. Wanajo 2006) synthesizes neutron-deficient nuclei up to Ag in proton-rich conditions $Y_e \gtrsim 0.5$. In nuclear statistical equilibrium at $T \gtrsim 5$ GK, all neutrons recombine with protons into α particles, which, via further cooling in the range $3 \text{ GK} \lesssim T \lesssim 5 \text{ GK}$, assemble ^{12}C via the triple alpha reaction $\alpha(2\alpha, \gamma)^{12}\text{C}$. The latter are converted in $(p, \gamma) - (\gamma, p)$ equilibrium on much faster timescales into heavier elements, mostly ^{56}Ni , ^{60}Zn , and ^{64}Ge . These elements with increased stability (β -decay lifetimes $\gtrsim 60$ s; equal numbers of neutrons and protons) serve as ‘waiting points’. In the range $1.5 \text{ GK} \lesssim T \lesssim 3 \text{ GK}$, free protons conspire with electron antineutrinos to produce free neutrons, $p + \bar{\nu}_e \rightarrow n + e^+$. Via fast (n, p) and subsequent (γ, p) reactions on the waiting point nuclei, these neutrons then continue the reactions to heavier

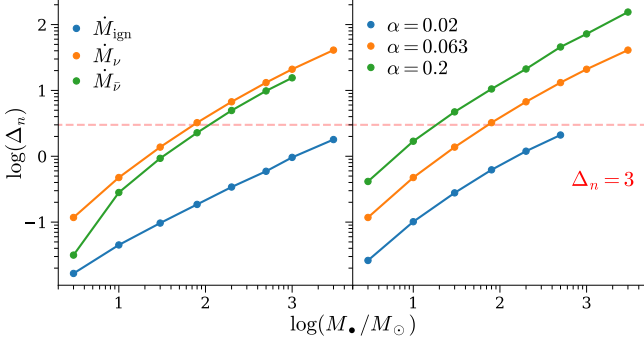


Figure 5. Left: Number of free neutrons per seed nucleus Δ_n created in disk outflows by electron antineutrino absorption under proton-rich conditions, as a function of black hole mass, for models with fiducial viscosity $\alpha = 0.063$, dimensionless black hole spin $\chi_\bullet = 0.95$, and various values of the accretion rate \dot{M} . Right: Analogous to the results in the left panel, but for models with $\dot{M} = \dot{M}_\nu$ and different values for the α -viscosity. The red dashed line marks the minimum threshold of $\Delta_n \approx 3$ for triggering a νp -process.

elements. Cooling below 1 GK terminates the νp -process as the (p, γ) reactions freeze out.

A figure of merit to quantify the potential for a successful νp -process is thus the number of free neutrons created per seed nucleus as the plasma cools through $1 \text{ GK} \lesssim T \lesssim 3 \text{ GK}$ (J. Pruet et al. 2006)

$$\Delta_n = \frac{Y_p}{Y_{\text{heavy}}} \int_{1 < T_9 < 3} \lambda_{\bar{\nu} e p} dt, \quad (90)$$

where Y_p and Y_{heavy} denote the abundance of free protons and seed nuclei heavier than ${}^4\text{He}$, respectively, $\lambda_{\bar{\nu} e p}$ is the rate of capture of antineutrinos onto protons, and T_9 is the temperature of the outflow in units of GK. At least $\Delta_n \sim \text{few} - 10$ is required for the production of νp -process elements heavier than the waiting point nuclei.

Figure 5 shows the results for Δ_n in disk outflows launched from the most proton-rich regions of the disk, for different values of the black hole mass, the accretion rate, and the α -viscosity, and computed with a simplified outflow model described in Appendix C. The values of Δ_n vary between several orders of magnitude, $\Delta_n \sim 10^{-2} - 10^2$, and they are highly dependent on both \dot{M} and α . The latter is expected because these quantities control the efficiency of neutrino cooling and hence also modulate the proton-fraction in the outflow and the antineutrino luminosity. We find that higher values of α or M_\bullet lead to larger Δ_n , while the sensitivity to \dot{M} is more complex, with highest values of Δ_n reached at $\dot{M} \approx \dot{M}_\nu$. These results are consistent with the findings that larger M_\bullet leads to larger proton excess (Figure 3), that the proton excess is generally largest

around $\dot{M} \approx \dot{M}_\nu$ (Figure 4), and that the proton excess at $\dot{M} \approx \dot{M}_\nu$ increases with increasing α (Figure 12).

We compare our results with those of A. Psaltis et al. (2024) to estimate the final nucleosynthesis products as a function of Δ_n . They obtain for neutrino-driven outflows under proton-rich conditions ($Y_e \approx 0.6$) with $s/k_B \sim 50 - 100$ and expansion timescales $\tau_{\text{exp}} \approx 10 - 50 \text{ ms}$ a resulting $\Delta_n \approx 3 - 60$, which leads to the production of elements with atomic number up to $Z \approx 50$. We find that for our models, which have values $Y_e \sim 0.5 - 0.75$, $s/k_B \sim 30 - 100$ and $\tau_{\text{exp}} \sim 40 \text{ ms} - 5 \text{ s}$, black hole masses of $M_\bullet \gtrsim 80$ are required to trigger an νp -process ($\Delta_n \gtrsim \text{few}$), assuming $\dot{M} \approx \dot{M}_\nu$ and the fiducial value of $\alpha \sim 0.06$. For values of the viscosity closer to those found in GRMHD simulations ($\alpha \sim 0.02$), our models just marginally enter the regime at large black hole masses $M_\bullet \gtrsim 500 M_\odot$ ($\Delta_n \sim 2.1$). These results suggest that neutrino-cooled accretion disks around massive black holes could, in principle, be promising sources of p -nuclei. However, given the large uncertainties involved in these estimates, more detailed hydrodynamical modeling and nuclear reaction network calculations may be necessary to assess the prospects for the νp -process more robustly.

5.6. Partial pressure contributions

The analytic scaling relations derived in Section 3 depend on a series of assumptions, particularly on the relation of plasma pressure with temperature. Figures 6 and 7 present examples of radial profiles of the different partial pressures of the accreting plasma considered in the model, while Figure 2 (III) shows the average value of the ratio of radiation and relativistic electron-positron e^\pm pressure versus baryon pressure for different models with $M_\bullet = 3 - 3000 M_\odot$, $\chi_\bullet = 0.95$, $\alpha = 0.063$ and different values of the accretion rate.

The $M_\bullet = 3 M_\odot$ accretion disk for fiducial parameters ($\alpha = 0.063$, $\chi_\bullet = 0.95$) shows a transition from an entirely pair and radiation-pressure dominated disk at accretion rates $\dot{M} \lesssim \dot{M}_{\text{ign}}$, to an increasingly baryon-pressure dominated accreting plasma with increasing accretion rate. This inversion of the hierarchy $p_{e^\pm} \sim p_\gamma \gg p_b \gg p_\nu$ to $p_b \gg p_{e^\pm} \gg p_\gamma \gtrsim p_\nu$ between $\dot{M} \lesssim \dot{M}_{\text{ign}}$ and $\dot{M} \sim \dot{M}_{\bar{\nu}-\text{opaque}}$ occurs gradually as the accretion rate increases and proceeds radially from the inside out. Neutrino pressure remains insignificant at the $\lesssim 1\%$ level. At the ignition threshold, electrons are sufficiently relativistic ($\theta \gtrsim \text{few} - 10$ for $r \lesssim 100 r_g$, Figure 4), such that approximately, $p_{e^\pm} \propto T^4$ (cf. Equation (B64) for the massless (ultra-relativistic) case), as for radiation pressure, $p_\gamma \propto T^4$. The assumption $p \propto T^4$ (Section 3.1) is therefore well justified at $\dot{M} \sim \dot{M}_{\text{ign}}$,

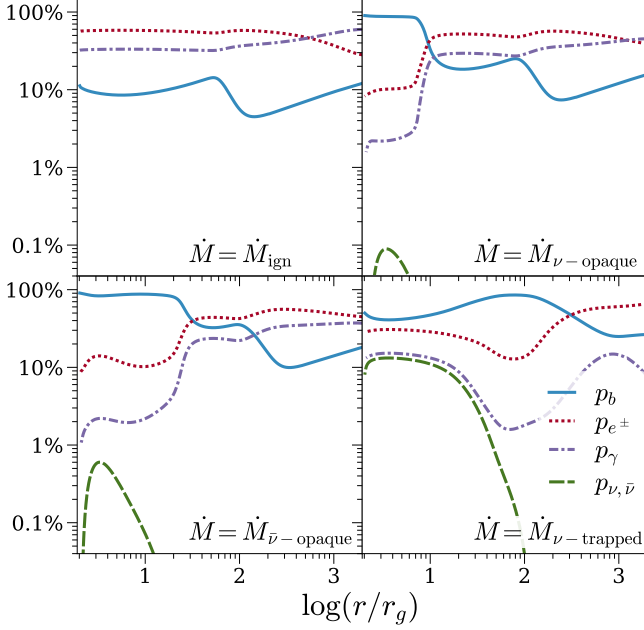


Figure 6. Radial profiles (in units of the gravitational radius r_g) of the percentage of the total pressure contributed by baryons p_b , by electrons and positrons $p_{e\pm}$, by radiation p_γ , and by electron neutrinos and antineutrinos p_ν , for an accretion disk with $M_\bullet = 3M_\odot$, $\chi_\bullet = 0.95$ and $\alpha = 0.063$ at various characteristic accretion rates (same models as in Figure 4).

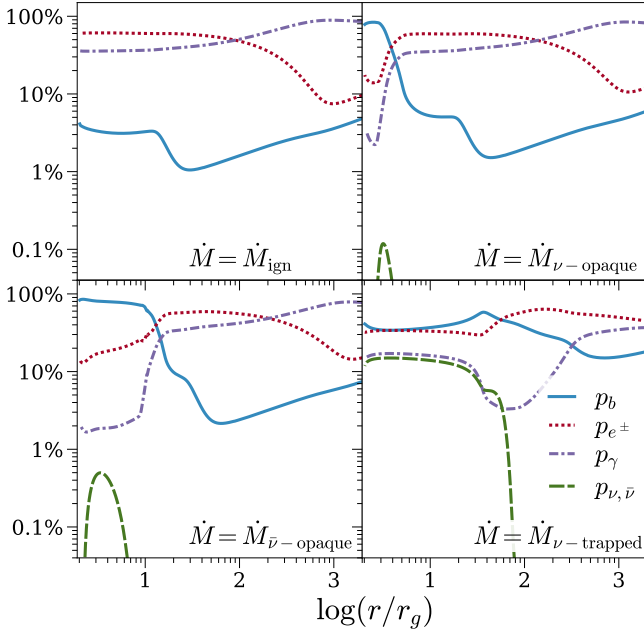


Figure 7. Analogous to Figure 6 but for an accretion disk around a black hole with mass $M_\bullet = 1000M_\odot$.

whereas $p \propto \rho T$ for $r \lesssim 10 - 100 r_g$ is appropriate for $\dot{M}_{\nu\text{-opaque}} \lesssim \dot{M} \lesssim \dot{M}_{\bar{\nu}\text{-opaque}}$. At $\dot{M} \gtrsim \dot{M}_{\nu\text{-trapped}}$, we typically find that $p_b \sim p_{e\pm}$ and neither of the two con-

tributions dominate. Furthermore, the pressure of the trapped neutrinos $p_{\nu,\bar{\nu}} \sim p_\gamma$ increases to the 10% level.

Figure 7 shows models analogous to Figure 6, but for a black hole with mass $M_\bullet = 1000M_\odot$. The general behavior of the pressure hierarchies are remarkably similar to that of the $M_\bullet = 3M_\odot$ case.

The different pressure regimes in the inner accretion disk are particularly evident in Figure 2 (III), throughout the parameter space shown there. In particular, for a given black hole mass the ratio $(p_\gamma + p_{e\pm})/p_b$ sharply decreases from $\gg 1$ at $\dot{M} \approx \dot{M}_{\text{ign}}$ to $\ll 1$, precisely where electrons become degenerate $\eta_e \sim 1$ (Figure 2 (I)), which occurs at $\dot{M}_{\text{ign}} \lesssim \dot{M} \lesssim \dot{M}_\nu$. With further increasing accretion rate, the inner accretion flow returns to a mildly degenerate state ($\eta_e \sim 0.3$) at $\dot{M} \gtrsim \dot{M}_{\nu\text{-trapped}}$ as the pressure ratio approaches order unity, $(p_\gamma + p_{e\pm})/p_b \sim 1$. This is due to a decreasing cooling efficiency as neutrinos become increasingly trapped (Figure 4 (IV)) and a corresponding rise in temperature (Figure 4 (III)) that decreases degeneracy (Figure 4 (II)). Figure 2 (III) also clearly reflects the increase of the pressure ratio with black hole mass, as predicted by Equations (58), (66), and (73).

5.7. Scaling relations of characteristic accretion rates

Figures 8 and 9 summarize results of a numerical exploration of the characteristic accretion rates across the vast parameter space of accretion flows around black holes of $M_\bullet = 3 - 3000 M_\odot$ with α -viscosities between $\alpha = 0.001 - 0.5$. Every data point represents an accretion disk model at a given characteristic accretion rate, numerically identified by exploring the respective neighborhood in parameter space with a targeted set of numerical disk models. To each series of identified models for a fixed α -viscosity parameter (Figure 8) or fixed black hole mass (Figure 9) and given characteristic accretion rate $\dot{M}_{\text{char}} = \{\dot{M}_{\text{ign}}, \dot{M}_\nu, \dot{M}_{\bar{\nu}}, \dot{M}_{\nu\text{-trap}}, \dot{M}_{\bar{\nu}\text{-trap}}\}$, power-law segments of the form

$$\dot{M}_{\text{char}} = C_{\text{char}} \left(\frac{M_\bullet}{3M_\odot} \right)^\beta \left(\frac{\alpha}{0.01} \right)^\gamma \quad (91)$$

were fitted, the inferred parameters of which are listed in Table 5.7. Figures 8, 9, and Table 5.7 show that all characteristic accretion rates $\dot{M}_{\text{char}} = \{\dot{M}_{\text{ign}}, \dot{M}_\nu, \dot{M}_{\bar{\nu}}, \dot{M}_{\nu\text{-trap}}, \dot{M}_{\bar{\nu}\text{-trap}}\}$ can be well described by power-law segments of this form throughout the parameter space probed. Broken power laws are a result of the critical accretion rates sweeping through different pressure regimes as ‘avoided crossings’ of characteristic accretion rates occur (see below).

In terms of the ignition threshold, the average coefficients obtained through fits to the numerical results are

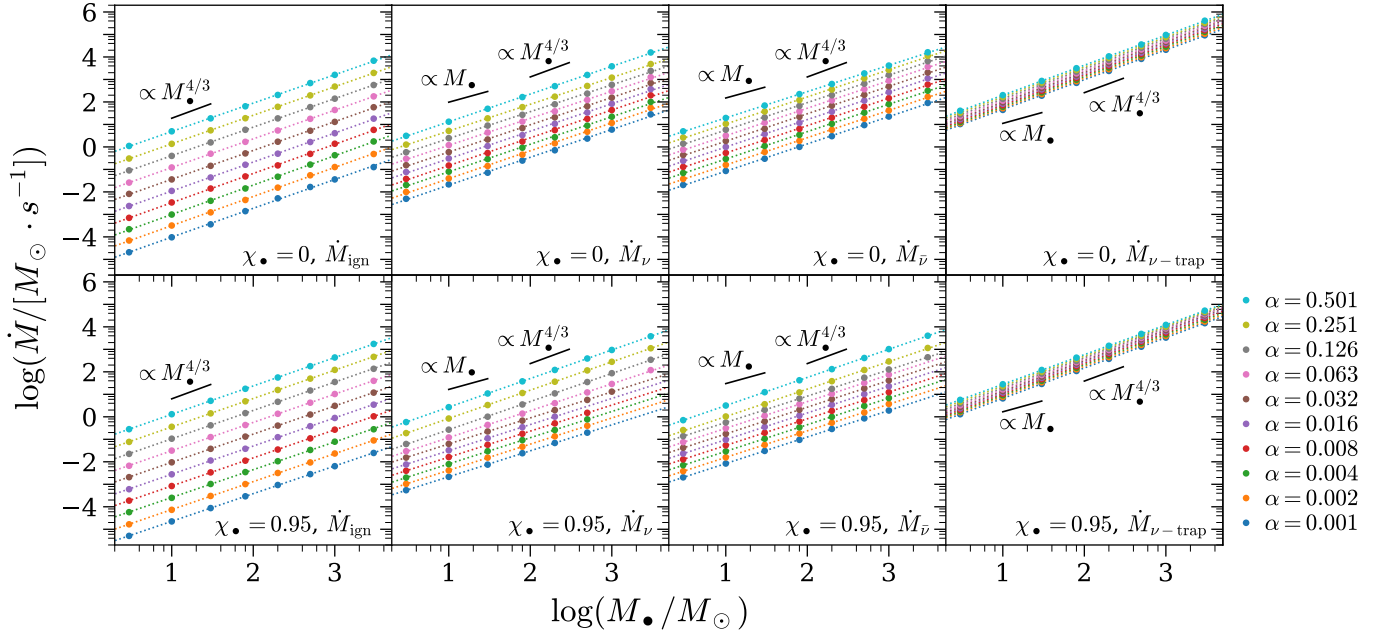


Figure 8. Characteristic accretion rates as numerically extracted from disk models as a function of black hole mass M_\bullet for different values of the α -viscosity and different spin parameters χ_\bullet . Dotted lines represent the best power-law fits $\dot{M} \propto M_\bullet^\beta$ to the set of disk models at a given value of α . Black lines represent the expected slopes of the approximate analytical power laws derived in Section 3.

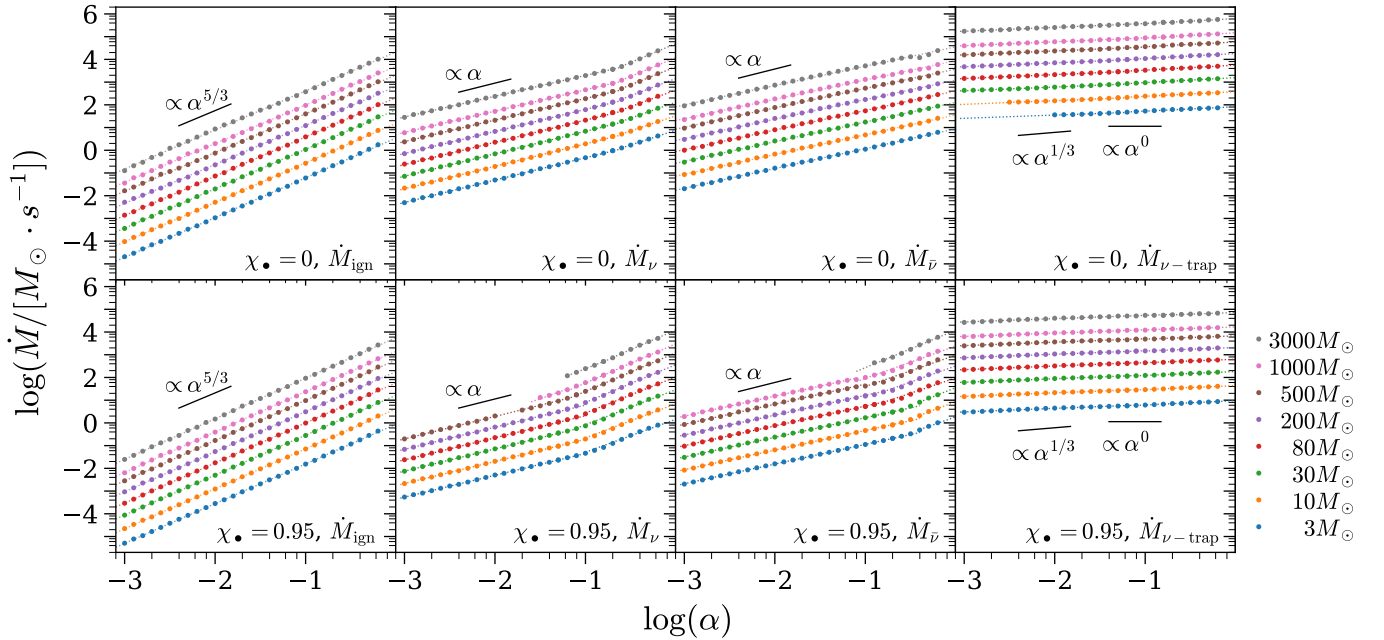


Figure 9. Characteristic accretion rates as numerically extracted from disk models as a function of the α -viscosity for different black hole masses and spin parameters χ_\bullet . Dotted lines represent the best power-law fit $\dot{M} \propto \alpha^\gamma$ to each set of models at a given black hole mass. Black lines represent the expected slope of the approximate analytical power laws derived in Section 3.

Threshold	Prediction $\dot{M} \propto M_{\bullet}^{\beta} \alpha^{\gamma}$	Spin χ_{\bullet}	Dominant Pressure	C_{char} [$M_{\odot} \text{s}^{-1}$]	Average fit values	
					β	γ
Ignition	$(p \propto p_{\gamma, e \pm}) \quad M_{\bullet}^{\frac{4}{3}} \alpha^{\frac{5}{3}}$	0.0	$p_{\gamma, e \pm}$	0.0011	1.28	1.73
		0.95	$p_{\gamma, e \pm}$	0.0003	1.25	1.77
ν -opaque	$(p \propto p_{\text{b}}) \quad M_{\bullet} \alpha$	0.0	p_{b}	0.0490	1.23	0.96
			$p_{\gamma, e \pm}$	1.6877*	1.23	1.49
	$(p \propto p_{\gamma, e \pm}) \quad M_{\bullet}^{\frac{4}{3}} \alpha$	0.95	p_{b}	0.0051	1.17	0.97
			$p_{\gamma, e \pm}$	0.2830*	1.26	1.65
$\bar{\nu}$ -opaque	$(p \propto p_{\text{b}}) \quad M_{\bullet} \alpha$	0.0	p_{b}	0.1629	1.21	0.86
			p_{b}	0.0158	1.18	0.86
	$(p \propto p_{\gamma, e \pm}) \quad M_{\bullet}^{\frac{4}{3}} \alpha$	0.95	$p_{\gamma, e \pm}$	0.3318*	1.21	1.57
ν -trapped	$(p \propto p_{\text{b}}) \quad M_{\bullet} \alpha^0$	0.0	$p_{\gamma, e \pm} \sim p_{\text{b}}$	15.468	1.34	0.24
	$(p \propto p_{\gamma, e \pm}) \quad M_{\bullet}^{\frac{4}{3}} \alpha^{\frac{1}{3}}$	0.95	$p_{\gamma, e \pm} \sim p_{\text{b}}$	2.1407	1.35	0.21
$\bar{\nu}$ -trapped	$(p \propto p_{\text{b}}) \quad M_{\bullet} \alpha^0$	0.0	$p_{\gamma, e \pm} \sim p_{\text{b}}$	36.291	1.29	0.19
	$(p \propto p_{\gamma, e \pm}) \quad M_{\bullet}^{\frac{4}{3}} \alpha^{\frac{1}{3}}$	0.95	$p_{\gamma, e \pm} \sim p_{\text{b}}$	4.4729	1.31	0.15

Table 1. Numerical results for the parameters C_{char} , β , and γ that characterize the scalings of the various characteristic accretion rates with black hole mass and α -viscosity, $\dot{M}_{\text{char}} = C_{\text{char}}(M_{\bullet}/3M_{\odot})^{\beta}(\alpha/0.01)^{\gamma}$ (Equation (91)). The values of β and γ represent, respectively, averages of the fits to the numerical accretion disk results for all values of α and M_{\bullet} considered. The corresponding analytic approximations computed in Section 3 are also listed, together with the assumed respective dominant pressure component. We distinguish between different segments that arise due to a change in the dominant pressure regime at ‘avoided crossings’ of the neutrino opaque and ignition thresholds at some value α_{c} , which depends on χ_{\bullet} and M_{\bullet} (see the text for details). Asterisks * refer to cases with avoided crossings normalized to $\alpha = 0.3$.

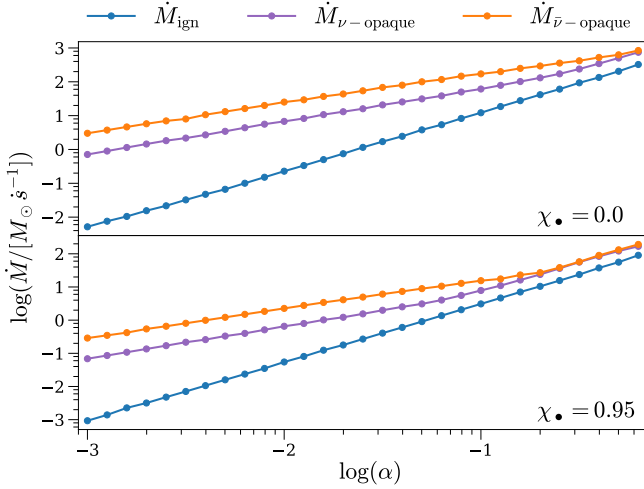


Figure 10. Characteristic accretion rates as a function of α -viscosity for non-rotating ($\chi_{\bullet} = 0.0$) and rapidly spinning ($\chi_{\bullet} = 0.95$) black holes of mass $M_{\bullet} = 200M_{\odot}$, illustrating the occurrence of ‘avoided crossings’ of the ignition and opaque accretion thresholds.

remarkably close to the analytic predictions for a radiation and e^{\pm} -pressure dominated plasma, $\beta \approx 4/3$ and $\gamma \approx 5/3$, throughout the parameter space probed here. This is consistent with a weak and opposing dependence of $p_{\gamma}/p_b \propto \alpha^{-1/6} M_{\bullet}^{1/6}$ at $\dot{M} = \dot{M}_{\text{ign}}$ (see Equation (58)) and is remarkable in light of the several simplifying assumptions adopted in the analytic calculations. A similar conclusion holds for the neutrino trapping thresholds, for which $\beta \approx 4/3$ and $\gamma \lesssim 1/3$ throughout the parameter space. This is consistent with a predominantly radiation and e^{\pm} -pressure dominated regime even at small values of α and M_{\bullet} (see also Figure 2 (III)) and an increasing but weak dependence $p_{\gamma}/p_b \propto \alpha^{1/6} M_{\bullet}^{1/6}$ at $\dot{M} = \dot{M}_{\nu\text{-trap}}$ (see Equation (73)).

The scaling behavior of the neutrino opaque thresholds is somewhat more complicated. At sufficiently small values of α , $\dot{M}_{\nu,\bar{\nu}}$ scales with $\gamma \approx 1$, as predicted by either pressure regime (Equation (64)). At some value α_c , which depends on χ_{\bullet} and M_{\bullet} , the scaling approaches $\gamma \approx 5/3$, i.e. that of the ignition threshold (see also Figure 10). Since the ratio p_{γ}/p_b is not expected to scale with α in either pressure regime (Equation (66)), this transition into a new segment is not due to a change of pressure regimes. It is rather due to an ‘avoided crossing’ of the ignition and opaque thresholds (Figure 10). Due to the weaker dependence of $\dot{M}_{\nu,\bar{\nu}}$ on both α and M_{\bullet} relative to that of \dot{M}_{ign} , the two thresholds are predicted to cross at some α_c . As a result of $\dot{M}_{\nu,\bar{\nu}}$ approaching \dot{M}_{ign} from above, the conditions at $\dot{M}_{\nu,\bar{\nu}}$ become necessarily dominated by radiation and e^{\pm} pressure (see discussion above), and thus the scaling with M_{\bullet} changes

from $\beta \gtrsim 1$ to $\approx 4/3$ (Equation (64)), which can be noticed in Figure 8 for some $\alpha \gtrsim \alpha_c$ that depends on χ_{\bullet} and M_{\bullet} . The additional change in the scaling of $\dot{M}_{\nu,\bar{\nu}}$ with α to $\gamma \approx 5/3$ becomes necessary as $\dot{M}_{\nu,\bar{\nu}}$ must not cross below \dot{M}_{ign} . Whereas in principle the accreting plasma can become dense enough to be optically thick to $\sim \text{MeV}$ neutrinos at the ignition threshold, this cannot arise in practice, as the disk temperatures first need to approach the proton-neutron mass difference near the ignition threshold to generate neutrinos that can be thermalized in the flow. We call this phenomenon an ‘avoided crossing’ of the critical accretion threshold levels.

5.8. Disk composition at the characteristic thresholds

The results presented in Figures 3 and 4 illustrate that neutrino-cooled accretion disks around black holes can have a very heterogeneous composition as a function of radius. This is a consequence of different radial regions residing in different accretion regimes according to the characteristic radii r_{ign} , $r_{\nu,\bar{\nu}}$, $r_{\nu,\bar{\nu}\text{-trap}}$. Therefore, disk outflows originating in different radial regimes of a neutrino-cooled accretion disk may also possess different composition. Below we discuss the rest-mass averaged composition of the innermost 20 gravitational radii of the disk at the characteristic accretion rates. We argue that this inner region is most indicative of the outflow composition insofar as realistic neutrino-cooled accretion disks in collapsars are truncated at an accretion shock at radii of $\sim 10 - 100r_g$ as the core of the progenitor star collapses onto the equatorial plane and circularizes at increasing radii with time, determined by angular momentum conservation as successively outer layers start to collapse (A. I. MacFadyen & S. E. Woosley 1999; D. M. Siegel et al. 2022). Outflows from the innermost accretion disk are also most likely to be unbound from the system, perhaps with the help of a magnetically dominated jet that may form in the polar regions and help to unbind the outer stellar layers in polar regions.

5.8.1. The ignition threshold and the breakdown of protonization

Figure 11 summarizes results from a sweep over parameter space for the mass-averaged Y_e at $\dot{M} = \dot{M}_{\text{ign}}$. As expected from the discussion in Section 5.4, the inner disk is proton-rich with $\langle Y_e \rangle \approx 0.5 - 0.7$ as a result of neutrino cooling under radiation and e^{\pm} -pressure dominated conditions as well as mild to vanishing electron degeneracy. Slightly neutron-rich conditions can only be achieved for non-rotating or slowly rotating black holes of mass $M_{\bullet} \lesssim \text{few} \times M_{\odot}$ at large values of $\alpha \gtrsim 0.1$, as a result of the onset of degeneracy $\langle \eta_e \rangle \gtrsim 0.3$. At sufficiently large viscosities $\alpha \gtrsim 0.1$, the opposing scaling

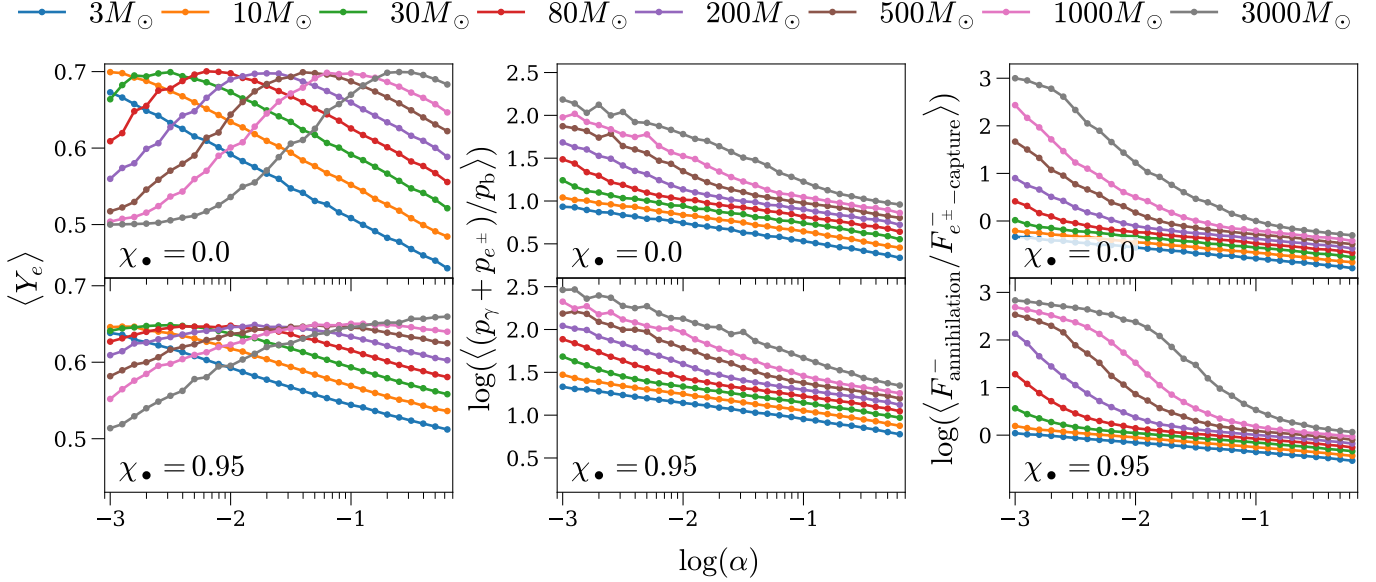


Figure 11. Left: Average disk electron/proton-fraction $\langle Y_e \rangle$ within $r \leq 20r_g$ as a function of the α -viscosity parameter for various black hole masses M_\bullet at the ignition threshold ($\dot{M} = \dot{M}_{\text{ign}}$) and different values χ_\bullet of the black hole spin. Center: Corresponding pressure ratios of radiation and e^\pm pressure to baryon pressure for the same set of models. Right: Corresponding ratio of the neutrino cooling fluxes due to pair annihilation and pair-capture

$(Y_e - 0.5) \propto \alpha^{-1/6} M_\bullet^{1/6}$ with α and M_\bullet as predicted by Equation (88) is evident. This trend is reversed, however, toward smaller values of the viscosity and large black hole masses, due to cooling via e^\pm -pair annihilation starting to dominate over e^\pm capture in the increasingly radiation and e^\pm -pressure dominated accretion flows. Neutrinos created by pair annihilation under non-degenerate conditions do not change the composition and thus $\langle Y_e \rangle$ approaches ≈ 0.5 for $M_\bullet \gtrsim 1000M_\odot$ at $\alpha = 0.001$. Associated with this is the drop in temperature $T \propto \alpha^{1/6} M^{-1/6}$ (Equation (88)) with decreasing viscosity and increasing black hole mass below the proton-neutron mass difference of $\approx 1.3\text{ MeV}$ and the dissociation threshold, which gradually suppresses the e^\pm -capture reactions. This marks the breakdown of protonization at small α -viscosities $\alpha \sim 0.001$ and large black hole masses $M_\bullet \gtrsim \text{few} \times 1000M_\odot$.

5.8.2. The opaque threshold and the breakdown of neutronization

The overall capability of neutronization of the inner accretion disks is well traced by the physical conditions at $\dot{M} \approx \dot{M}_{\nu,\bar{\nu}}$. Our results shown in Figure 1 indicate that neutrino-cooled disks must reach accretion rates $\dot{M}_{\text{ign}} \lesssim \dot{M} \lesssim \dot{M}_\nu$ in order to efficiently neutronize the nucleon plasma (see also Section 5.2). This is a necessary but not sufficient condition. Figure 1 displays a striking rise in the ‘valley floor’ of the rest-mass density averaged Y_e within $r \leq 20r_g$ at $\dot{M} \sim \dot{M}_{\nu,\bar{\nu}}$ from $\langle Y_e \rangle \approx 0.1$ for stellar mass black holes $M_\bullet \lesssim 10M_\odot$ to

$\langle Y_e \rangle \gtrsim 0.45$ at $M_\bullet \gtrsim \text{few} \times 1000M_\odot$, depending on the spin of the black hole. The disk composition, however, also depends on the α -viscosity, and a more comprehensive coverage of the parameter space in terms of $\langle Y_e \rangle$ near $\dot{M} \sim \dot{M}_{\nu,\bar{\nu}}$ is provided by Figure 12. In this section, we focus mainly on the composition around $\dot{M} \sim \dot{M}_{\nu,\bar{\nu}}$, as this corresponds to the most neutron-rich part of the parameter space, at least at sufficiently small values of α ($\alpha \lesssim 0.1 - 0.2$). In principle, neutronization can break down as it is based on a number of assumptions: i) the dominance of baryon pressure over radiation and e^\pm pressure, ii) the capture of relativistic electrons and positrons on free nucleons dominates neutrino cooling, and iii) local turbulence through the MRI described by an effective α -viscosity dominates over instabilities due to self-gravity in setting the accretion rate. We explore the breakdown of neutronization in the ‘neutron-rich valley’ around $\dot{M} \sim \dot{M}_{\nu,\bar{\nu}}$ in more detail in the following.

As evident from Figure 12, neutronization in the inner accretion disk becomes increasingly suppressed with increasing values of α , starting at values $\alpha \gtrsim 0.2$ for non-rotating black holes and $\alpha \gtrsim 0.1$ for $\chi_\bullet = 0.95$. We identify the reason for this behavior as an avoided crossing of the opaque and the ignition thresholds, which occurs precisely around the respective values of α (see Figure 9). As a result of this, the inner accretion flow becomes necessarily dominated by radiation and e^\pm pressure with increasing α (Section 5.7), which is clearly illustrated by the bottom panel of Figure 12. The ratio of cooling through e^\pm capture relative to pair annihila-

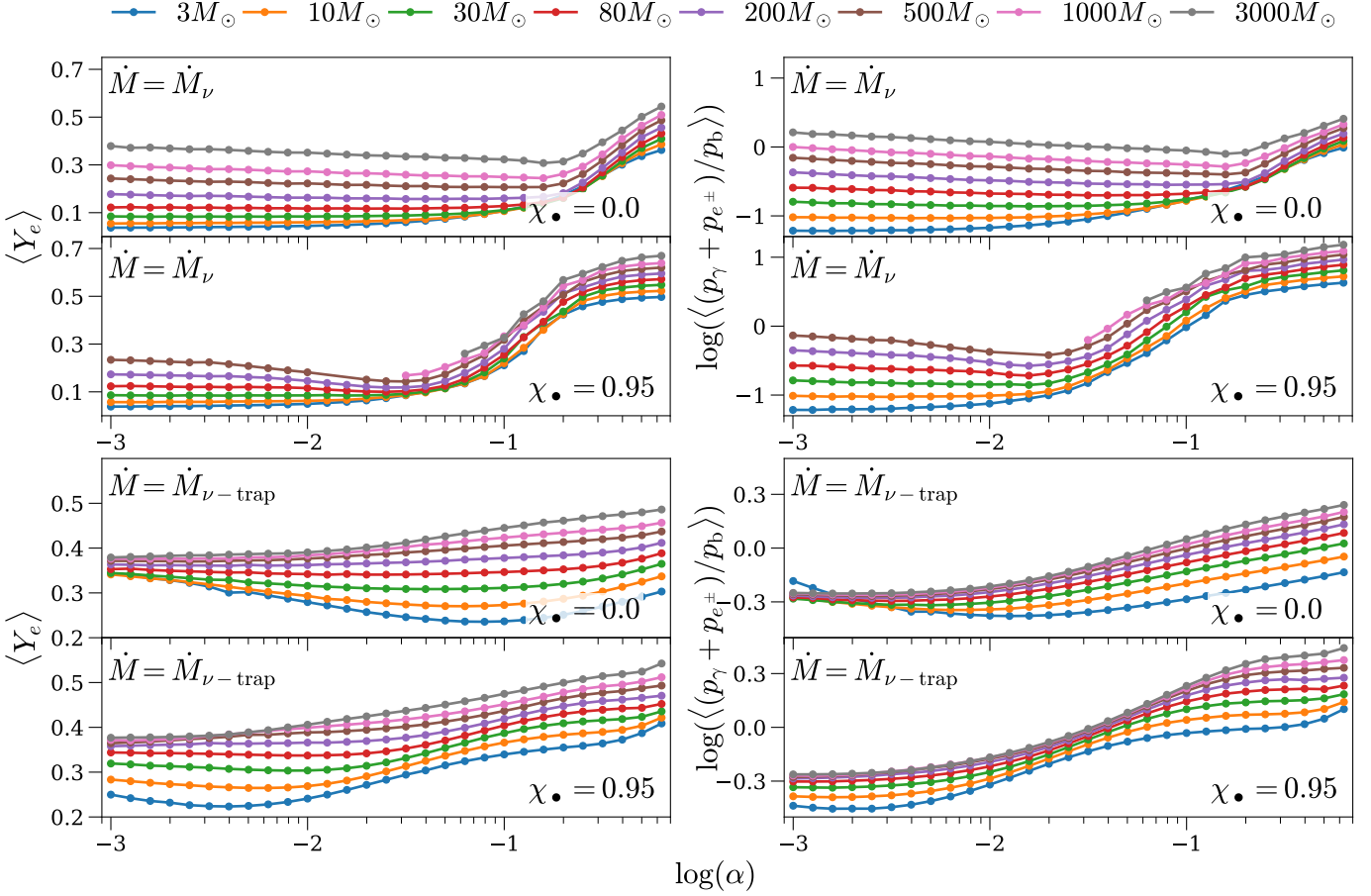


Figure 12. Top: Analogous to the left and center columns of Figure 11, for disks at the neutrino-opaque threshold ($\dot{M} = \dot{M}_\nu$). Bottom: Idem for disks at the neutrino-trapped threshold ($\dot{M} = \dot{M}_{\nu\text{-trap}}$).

tion scales proportionally (see Equation (82)), and thus fewer and fewer emitted neutrinos are associated with neutronization. This results in an increase of Y_e with increasing α to a composition comparable to that at the ignition threshold, as expected for an avoided crossing.

At sufficiently small values of the effective viscosity ($\alpha \lesssim 0.2$ for $\chi_\bullet = 0$ and $\alpha \lesssim 0.1$ for rapidly rotating black holes with $\chi_\bullet = 0.95$), the composition at $\dot{M} = \dot{M}_\nu$ approaches a nearly constant value for any given black hole mass. This is mainly regulated by the pressure ratio $p_{\gamma, e^\pm}/p_b$, which also approaches an approximately constant value at small α for a given black hole mass (bottom panel of Figure 12). This is expected from Equation (66), regardless of which pressure component dominates. With increasing black hole mass, the pressure ratio increases as $\propto M_\bullet$ in the baryon-pressure dominated regime for stellar-mass black holes and gradually transitions into the weaker scaling of $\propto M_\bullet^{1/6}$ once disks at $\simeq 1000M_\odot$ transition into the radiation and e^\pm -pressure dominated regime (essentially independent of the black hole spin χ_\bullet). Note that the temperature in the baryon-pressure dominated regime is approx-

imately independent of α and M_\bullet (see Equation (60)) and decreases moderately with black hole mass $\propto M_\bullet^{-1/6}$ (Equation (88)) once the disks become radiation and e^\pm -pressure dominated. As $p_{\gamma, e^\pm}/p_b$ increases to an order unity fraction at $M_\odot \gtrsim 100M_\odot$ (roughly independent of the black hole spin), the ratio of cooling through e^\pm capture relative to pair annihilation (see Equation (82)) reaches the percent level and Y_e starts to increase markedly as a result of fewer neutrinos participating in neutronization via the charged current interactions (Equations (25) and (26)).

Much of the parameter space for large black hole masses and accretion rates corresponds to gravitationally unstable disks $Q_{\text{grav}} < 1$ (see Figure 2), for which our assumption of stationarity and that of a pure Kerr background spacetime does not hold anymore. Gravitationally unstable disks tend to self-regulate to restore $Q_{\text{grav}} \approx 1$ by enhancing angular momentum transport through gravitationally driven turbulence (C. F. Gammie 2001). This corresponds to an increase in the effective α -viscosity parameter, which, at least in a stationary sense, starts to suppress neutronization at val-

ues $\alpha \gtrsim 0.1 - 0.2$ (see above; Figure 12). The average composition of the inner accretion disk reported here thus likely reflects a lower limit in the gravito-turbulent regime.

5.8.3. The trapping thresholds

Except for very light black holes with $M_\bullet \lesssim 3M_\odot$ and $\alpha \approx \text{few} \times 10^{-3}$ ($\chi_\bullet = 0.95$) or $\alpha \approx 0.1$ ($\chi_\bullet = 0$), the inner accretion flow at $\dot{M} = \dot{M}_{\nu\text{-trap}}$ reaches an average composition of $\langle Y_e \rangle > 0.25$ (Figure 12), which closes off the ‘valley floor’ of neutronization toward high accretion rates (Figure 1). This increase in Y_e relative to \dot{M}_ν is the result of an overall suppression of lepton number emission through electron capture under degenerate conditions due to the onset of neutrino trapping and an increase in the ratio of pair annihilation relative to e^\pm captures related to an increase in radiation and e^\pm pressure (Equation (82); Figure 12).

6. DISCUSSION

6.1. Comparison with 3D GRMHD simulations

We find good agreement between the predictions of our model and the exploration of the ignition threshold across $M_\bullet \sim 80 - 3000M_\odot$ with three-dimensional GRMHD simulations of isolated collapsar disks by A. Agarwal et al. (2025). For technical reasons, the ignition threshold in A. Agarwal et al. (2025) was defined by the criterion $\langle \eta_e \rangle = 0.5$ when averaged between $(1 - 3) \times r_{\text{ISCO}}$. In both studies, the expected approximate scaling $\dot{M}_{\text{ign}} \propto M_\bullet^{4/3} \alpha^{5/3}$ is well reflected by the respective numerical results.

To further test the absolute normalization of the scaling relation, we analyzed models with the above mentioned criterion $\langle \eta_e \rangle = 0.5$ using the parameters $\alpha = 0.009$ for the self-consistent, effective GRMHD viscosity, $\chi_\bullet = 0.8$, and $M_\bullet = (80, 500, 1000)M_\odot$ reported by A. Agarwal et al. (2025). We find that the predictions of our model of $\dot{M}_{\text{ign}} \approx (0.05, 0.34, 1.28)M_\odot \text{ s}^{-1}$ for these black hole masses either agree within error bars with those of A. Agarwal et al. (2025), or are up to a factor of ≈ 2 smaller than their uncertainty range in A. Agarwal et al. (2025). This level of agreement is remarkable given that the accretion disks in A. Agarwal et al. (2025) do not have infinite spatial extent (they are rather compact) and ‘sweep across’ the ignition threshold (i.e. they are not truly stationary).

Finally, we also find that the breakdown of neutronization at the ignition threshold and effective $\alpha \approx 0.009$ of A. Agarwal et al. (2025) is consistent with the predictions of our model (see Figure 1 for a rough comparison).

6.2. PISN events and their super-kilonova signatures

Figure 1 shows example trajectories of the accretion process in massive collapsars with rapidly rotating progenitor stars just above the pair-instability supernova mass gap ($\gtrsim 130M_\odot$) at the onset of core-collapse, as in D. M. Siegel et al. 2022. We generated these trajectories with the semi-analytical collapsar model of D. M. Siegel et al. 2022, assuming $\alpha = 0.06$ for disk viscosity as appropriate for Figure 1. We used the progenitor models of M. Renzo et al. 2020 with initial He-core mass of $200M_\odot$ (red line), $220M_\odot$ (light blue line), and $250M_\odot$ (pink line), the latter being the exact same model 250.25 of D. M. Siegel et al. 2022 (see their Figure 3). All progenitor models are endowed with a parametrized (broken power-law) angular momentum profile at the time of core-collapse as in D. M. Siegel et al. 2022, assuming the fiducial parameter choices as in their Figure 1.

These rapidly rotating progenitors give rise to collapsar systems, which populate the pair-instability supernova mass gap between $\approx 50 - 130 M_\odot$ with black holes ‘from above’, due to substantial mass loss (typically up to tens of solar masses) through disk outflows during the accretion process. Here, the models yield final black hole masses between $\approx 80 - 100M_\odot$ (Figure 1).

Based on analogous scaling relations to those derived in Section 3, obtained for Newtonian accretion disks, D. M. Siegel et al. 2022 predict the possibility of massive, neutron-rich disk outflows that can escape the collapsing star, carry up to several solar masses of r -process generating material, and can thus produce “super-kilonovae”, scaled-up versions of kilonovae. Although we find slight modifications of the scaling relations to be appropriate in this context (see Section 5.7; dominating baryon pressure at $\dot{M} \sim \dot{M}_{\nu,\bar{\nu}}$ as compared to radiation and e^\pm pressure dominance), our present numerical results show that such super-collapsar accretion histories can indeed transition through a neutron-rich regime, with the inner accretion disk being dominated by a well-defined, asymptotic, low- Y_e value of $Y_e \lesssim 0.1$ throughout an extensive part of the entire accretion process (Figure 1). Whereas direct comparison with the accretion history of the time-dependent models of D. M. Siegel et al. 2022 is intrinsically difficult, for the black hole spin evolves during the collapse process, comparison with the inner structure of the accretion disks of our present stationary models confirms the basic assumptions of neutronization underlying the semi-analytic model for super-kilonovae of D. M. Siegel et al. 2022.

6.3. Implications for r -process in GRB221009A

The long-duration gamma-ray burst (GRB) GRB221009A is the brightest GRB ever detected in

terms of peak flux and fluence and has the highest isotropic equivalent total energy ($E_{\text{iso}} \simeq 1.0 \times 10^{55}$ erg) detected so far as well as an exceptionally large (in the 99th percentile of GRBs) isotropic equivalent peak luminosity of $L_{\text{iso}} \simeq 1.0 \times 10^{54}$ erg s $^{-1}$ (E. Burns et al. 2023; S. Lesage et al. 2023; M. A. Williams et al. 2023). If the gamma-ray luminosity of the jet tracks the accretion rate onto the black hole, $L_{\gamma} = \eta \dot{M} c^2$ with some efficiency $\eta \ll 1$, the large accretion rate implied by GRB221009A suggests that it surpassed the ignition threshold to produce r -process elements in disk outflows (D. M. Siegel et al. 2019). Whereas this together with its proximity (redshift of $z = 0.151$, D. B. Malesani et al. 2025) makes GRB221009A, in principle, a promising target to search for r -process nucleosynthesis, no such r -process signatures were identified in this event (P. K. Blanchard et al. 2024).

Should GRB221009A have a wide jet opening angle $\theta_j \simeq 27^\circ$ as inferred by D. A. Kann et al. (2023), we estimate the accretion rate during the GRB phase to

$$\dot{M} = 6.2 M_{\odot} \text{s}^{-1} \left(\frac{L_{\gamma, \text{iso}}}{10^{54} \text{erg s}^{-1}} \right) \left(\frac{\eta}{0.01} \right)^{-1} \left(\frac{\theta_j}{27^\circ} \right)^2, \quad (92)$$

and thus, with the results of Section 5.7,

$$\frac{\dot{M}}{\dot{M}_{\nu\text{-trap}}} \simeq 3 \left(\frac{L_{\gamma, \text{iso}}}{10^{54} \text{erg s}^{-1}} \right) \left(\frac{\eta}{0.01} \right)^{-1} \times \left(\frac{\theta_j}{27^\circ} \right)^2 \left(\frac{M_{\bullet}}{3M_{\odot}} \right)^{-1.35} \left(\frac{\alpha}{0.01} \right)^{-0.21} \quad (93)$$

Here, we have assumed a rapidly spinning black hole ($\chi_{\bullet} = 0.95$) as typical for collapsar black holes. Given the presence of an associated typical Type Ic-BL supernova (P. K. Blanchard et al. 2024), we also normalized to a typical black hole mass during the early GRB phase of an ordinary collapsar (D. M. Siegel et al. 2019). Finally, we normalize to a typical value of the α -viscosity as obtained from three-dimensional GRMHD simulations (S. A. Balbus & J. F. Hawley 1998; J. F. Hawley & S. A. Balbus 2002; R. F. Penna et al. 2013; D. M. Siegel et al. 2019; S. De & D. M. Siegel 2021; A. Agarwal et al. 2025).

This estimate suggests that collapsar accretion disks in GRBs as luminous as GRB221009A may have surpassed the neutrino trapping threshold, such that the average electron-fraction in the inner disk increases beyond $\langle Y_e \rangle \gtrsim 0.25 - 0.3$ (see Section 5.2; Figure 12), preventing significant production of lanthanides in the disk outflows. Even if $\langle Y_e \rangle$ is moderately lower, the strong irradiation of the outflows by neutrinos from the inner accretion disk in the regime $\dot{M} \gtrsim \dot{M}_{\nu}$ may suppress lanthanide production. More neutron-rich out-

flows at larger radii $r > r_{\nu\text{-trap}}$ may still synthesize lanthanides; however, collapsar accretion disks in the early GRB phase are expected to be very compact, as the progenitor layers collapse inside out, and thus it remains unclear whether and how much disk material from $r > r_{\nu\text{-trap}}$ can be unbound from the system at these early stages in the collapse process. A red excess relative to the supernova at late times in the light curves or significantly reddened spectra, as predicted for high-opacity, lanthanide-bearing collapsar outflows by D. M. Siegel et al. 2019 and D. M. Siegel et al. 2022, are thus not expected for exceptionally bright GRBs such as GRB221009A. Nevertheless, a search for spectral features of light r -process elements such as strontium as in kilonovae from neutron-star mergers (D. Watson et al. 2019; A. Snepken et al. 2024) may be promising.

7. CONCLUSIONS

We present a one-dimensional, general-relativistic, viscous-hydrodynamic model of accretion disks around black holes, targeted at accretion flows in which weak interactions are ignited and neutrino emission cools the plasma. We focus on the compositional properties of the plasma in the inner accretion disk within tens of gravitational radii and explore the self-protonization and self-neutronization of the flow at sufficiently high accretion rates when ordinary nuclei are dissociated into a nucleon plasma, across the vast parameter space of accretion rates $\dot{M} \sim 10^{-6} - 10^6 M_{\odot} \text{s}^{-1}$, black hole masses of $M_{\bullet} \sim 1 - 10^5 M_{\odot}$ and dimensionless spins of $\chi_{\bullet} \in [0, 1]$, as well as α -viscosity values of $\alpha \sim 10^{-3} - 1$.

Such accretion flows can arise in ordinary collapsars, thought to be the progenitors of long GRBs (D. M. Siegel et al. 2019), in massive collapsars above the PISN mass gap, which may populate the PISN mass gap with black holes and give rise to super-kilonovae (D. M. Siegel et al. 2022), as well as during the collapse of supermassive stars (A. Agarwal et al. 2025). Although we assume equal numbers of neutrons and protons ($Y_e = 0.5$) as an outer radial boundary condition of the accreting plasma, targeted to collapsars, the physics of the inner accretion flow becomes largely insensitive to this, and the model (with adapted boundary condition) as well as the concrete properties of the accretion flows discussed here are also broadly applicable to accretion disks that form in the aftermath of neutron-star mergers.

The compositional properties of the accretion flows explored here can provide some indication for the prospects and expected outcomes of r -process nucleosynthesis in disk outflows. The predictions made here need to be checked with multi-dimensional simulations and detailed neutrino transport in future work. Our

model allows for a computationally efficient scan of the vast parameter space, currently impossible to cover for multi-dimensional GRMHD or viscous hydrodynamic simulations, which can at most focus on a few selected parameter choices at a time (O. Just et al. 2022; C. Dean & R. Fernández 2024; D. Issa et al. 2025; M. Shibata et al. 2025; A. Agarwal et al. 2025). Furthermore, our model serves as a useful basis for the interpretation and analysis of the physics and dynamics of more detailed, non-stationary, three-dimensional GRMHD simulations by means of a relatively simple physical model. Our main conclusions may be summarized as follows.

1. For a given black hole and self-consistent description of turbulence (α -viscosity), the accretion state is mainly determined by the accretion rate onto the black hole. We find (Figures 1 and 2) that a characterization of the accretion state relative to certain critical thresholds is useful: the minimum accretion rates required to efficiently cool the inner flow (\dot{M}_{ign}), to render the inner flow opaque to electron neutrinos and antineutrinos (\dot{M}_ν and $\dot{M}_{\bar{\nu}}$), and to trap neutrinos and antineutrinos in the inner flow ($\dot{M}_{\nu\text{-trap}}$ and $\dot{M}_{\bar{\nu}\text{-trap}}$).
2. The accretion flow self-neutronizes due to the onset of electron degeneracy at $\dot{M}_{\text{ign}} \lesssim \dot{M} \lesssim \dot{M}_\nu$ and enters a self-regulation regime based on electron degeneracy that balances viscous heating and neutrino cooling (Figures 3 (IV), 4 (IV)), entering a ‘valley floor’ with a well defined, small value of $Y_e \lesssim 0.1$ at around $\dot{M} \sim \dot{M}_{\nu,\bar{\nu}}$ that can be analytically estimated (Equation (83); Figures 1, 3 (I), 4 (I)).
3. The inner accretion flow at $\dot{M} \lesssim \dot{M}_{\text{ign}}$ as well as the flow in a radial range around the neutronized inner flow at $\dot{M} > \dot{M}_{\text{ign}}$ protonizes as $(Y_e - 0.5) \propto \alpha^{-1/6} M_\bullet^{1/6}$ (Equation (89)) due to the proton-neutron mass difference skewing the balance of the charged current interactions toward positron capture onto neutrons in mildly to non-degenerate conditions (Figures 1 and 11). The resulting $Y_e \approx 0.5 - 0.8$ can be well estimated analytically in these regions (Equation (86)). A breakdown of protonization at \dot{M}_{ign} is observed according to the above scaling for $M_\odot \lesssim 3M_\odot$ and $\alpha \lesssim 1$; a gradual breakdown also occurs at $M_\odot \gtrsim 3000M_\odot$ for $\alpha \lesssim 0.001$ (Figure 11) due to $T \propto \alpha^{1/6} M_\odot^{-1/6}$ dropping below $\simeq 1$ MeV required for dissociation and e^\pm -capture and increasing dominance of radiation and e^\pm pressure.
4. With expansion speeds of $\approx 0.03 - 0.12c$ set by the recombination of nucleons into α -particles and entropies of $\sim 10k_B$ per baryon (e.g., Figure 2), disk outflows from the neutron-rich parts of the accretion disks can synthesize r -process elements (Section 5.3). Disks around black holes as massive as $\sim 10^3 M_\odot$ can give rise to neutron-rich winds; however, the production of lanthanides is disfavored for black holes with $\chi_\bullet = 0 - 0.95$ heavier than $\sim 200 - 500 M_\odot$, due to increasing proton-fractions ($Y_e \gtrsim 0.25$) and/or increasing expansion timescales ($\tau \gtrsim 0.5$ s) that lead to late-time reheating of the ejecta and a restart of the r -process at higher Y_e . Associated super-kilonovae may thus appear ‘red’, peaking in the infrared, for $M_\bullet \lesssim 200 - 500 M_\odot$ corresponding to $\chi_\bullet = 0 - 0.95$, and ‘blue’, peaking in the optical wavelength range, for larger black hole masses.
5. Using a simple disk outflow model (Appendix C), we find that outflows from the proton-rich parts of the accretion disks may give rise to the synthesis of proton-rich isotopes via the νp -process, specifically for large black hole masses $M_\bullet \gtrsim 100 M_\odot$ and accretion rates $\dot{M} \approx \dot{M}_\nu$ (Figure 5). Given the large uncertainties in our estimates, further investigation is required in this direction to assess in more detail the contribution of such disks to the nucleosynthesis of neutron-deficient p-nuclei.
6. The characteristic threshold accretion rates approximately follow power laws of the form $\dot{M}_{\text{char}} \propto M_\bullet^\beta \alpha^\gamma$ (Figures 8 and 9), with exponents (Table 5.7) in good agreement with approximate analytic scaling relations derived in Section 3. For the opaque thresholds, broken power laws apply due to the presence of ‘avoided crossings’ with the ignition threshold, which enforce a transition from baryon to radiation and e^\pm -pressure dominated plasma (Figure 10).
7. The onset of a breakdown of neutronization in the low- Y_e valley floor around $\dot{M} \sim \dot{M}_\nu$ is observed at $\alpha \gtrsim 0.1 - 0.2$, depending on the black hole spin (Figure 12). This is a result of an avoided crossing of the opaque and ignition thresholds (Section 5.8.1). The nearly constant ‘valley floor’ for a given black hole mass at $\alpha \lesssim 0.1 - 0.2$ increases from $Y_e \lesssim 0.1$ at $M_\bullet \approx \text{few} \times M_\odot$ to $Y_e \approx 0.5$ at several thousand M_\odot as a result of the disks becoming increasingly radiation and e^\pm -pressure dominated.

8. The predictions of our model for both the absolute normalization and relative scaling of the onset of degeneracy in the inner disk ($\langle \eta_e \rangle = 0.5$) are in good agreement with the 3D GRMHD simulations of collapsar accretion disks across $M_\odot = 80 - 3000 M_\odot$ by A. Agarwal et al. (2025) (their ‘ignition threshold’). Our results are also consistent with the 3D GRMHD simulations of post-merger accretion disks of S. De & D. M. Siegel (2021), who report an ignition threshold at $\approx 10^{-3} M_\odot \text{ s}^{-1}$ for a remnant black hole of $M_\bullet = 3 M_\odot$ and an effective α -viscosity of $\alpha \approx 1 \times 10^{-2}$.
9. Our results confirm the neutronization of accretion disks around black holes of tens of M_\odot at $\dot{M} \gtrsim \dot{M}_{\text{ign}}$ as realized in models of massive collapsars. These findings thus support the basic assumptions of neutronization underlying the semi-analytic model for super-kilonovae of D. M. Siegel et al. (2022).
10. We estimate that the accretion flow in the collapsar triggering the brightest GRB of all times, GRB221009A, likely resided in the neutrino-trapped regime while the GRB was powered (Equation (93)), suppressing the production of lanthanides (Figure 12). Reddening of the supernova lightcurves at late times due to high-opacity, lanthanide-bearing collapsar outflows as predicted

by D. M. Siegel et al. (2019) and D. M. Siegel et al. (2022) may thus not be expected for exceptionally bright GRBs such as GRB221009A.

ACKNOWLEDGEMENTS

The authors thank Geoffrey Ryan for valuable discussions during the early stages of this project and for providing optimized code to compute Fermi-Dirac integrals (`fdlo`, G. Ryan 2022). We thank Aman Agarwal for providing the trajectories of collapsar accretion histories in Figure 1. We also thank N. C. Stone and Y. Lerner for discussion and feedback on the disk model, and B. D. Metzger for comments on the manuscript. JHM acknowledges the Perimeter Institute for Theoretical Physics for providing the research environment to start this project through their Perimeter Scholars International Program. The authors gratefully acknowledge the computing time made available to them on the high-performance computer “Lise” at the NHR Center NHR@ZIB and “Emmy” at the NHR Center NHR@Göttingen. These centers are jointly supported by the Federal Ministry of Education and Research and the state governments participating in the NHR (www.nhr-verein.de/unsere-partner).

Software: `Matplotlib` (J. D. Hunter 2007), `NumPy` (C. R. Harris et al. 2020), `SciPy` (P. Virtanen et al. 2020), `hdf5` (The HDF Group 2025) and `fdlo` (G. Ryan 2022).

APPENDIX

A. DISK EQUATIONS

In this appendix, we derive all relevant structure equations of an axisymmetric, neutrino-cooled, thin accretion disk in Kerr spacetime. Following the nomenclature of I. D. Novikov & K. S. Thorne (1973), D. N. Page & K. S. Thorne (1974), and W.-X. Chen & A. M. Beloborodov (2007), we define the following dimensionless auxiliary functions

$$\begin{aligned} \mathcal{A} &= 1 + \frac{\chi_\bullet^2}{x^4} + \frac{2\chi_\bullet^2}{x^6}, & \mathcal{B} &= 1 + \frac{\chi_\bullet}{x^3}, & \mathcal{C} &= 1 - \frac{3}{x^2} + \frac{2\chi_\bullet}{x^3}, \\ \mathcal{D} &= 1 - \frac{2}{x^2} + \frac{\chi_\bullet^2}{x^4}, & \mathcal{F} &= 1 - \frac{2\chi_\bullet}{x^3} + \frac{\chi_\bullet^2}{x^4}, & \mathcal{G} &= 1 - \frac{2}{x^2} + \frac{\chi_\bullet}{x^3}, \end{aligned} \quad (\text{A1})$$

$$J = \frac{x^4 - 4\chi_\bullet x - 3\chi_\bullet^2}{x^4 + 2\chi_\bullet x - 3x^2}, \quad S = \frac{\mathcal{C}^{3/2} \mathcal{D}}{\mathcal{B} \mathcal{D}^2}, \quad (\text{A2})$$

as well as

$$\begin{aligned} \mathcal{Q} &= \frac{\mathcal{B}}{\mathcal{C}^{1/2}} \frac{1}{x} \left[x - x_0 - \frac{3}{2} \chi_\bullet \ln \left(\frac{x}{x_0} \right) - \frac{3(x_1 - \chi_\bullet)^2}{x_1(x_1 - x_2)(x_1 - x_3)} \ln \left(\frac{x - x_1}{x_0 - x_1} \right) \right. \\ &\quad \left. - \frac{3(x_2 - \chi_\bullet)^2}{x_2(x_2 - x_1)(x_2 - x_3)} \ln \left(\frac{x - x_2}{x_0 - x_2} \right) - \frac{3(x_3 - \chi_\bullet)^2}{x_3(x_3 - x_1)(x_3 - x_2)} \ln \left(\frac{x - x_3}{x_0 - x_3} \right) \right], \end{aligned}$$

where $x = (r/M_\bullet)^{1/2}$ is a normalized radial coordinate, $\chi_\bullet = a_\bullet/M_\bullet \in [0, 1)$ the dimensionless black hole spin, and

$$x_0 = (r_{\text{ISCO}}/M_\bullet)^{1/2}, \quad x_1 = 2 \cos \left[\frac{1}{3} \arccos(\chi_\bullet) - \frac{\pi}{3} \right], \quad (\text{A3})$$

$$x_2 = 2 \cos \left[\frac{1}{3} \arccos(\chi_\bullet) + \frac{\pi}{3} \right], \quad x_3 = -2 \cos \left[\frac{1}{3} \arccos(\chi_\bullet) \right]. \quad (\text{A4})$$

We transform the Kerr metric $g_{\mu\nu}$ from Boyer-Lindquist coordinates (Equation (1)) into cylindrical coordinates $x^\mu = (t, r, \phi, z)$. Since we consider thin accretion disks ($H/r \ll 1$), we only retain leading-order terms in z/r . The vertical structure equation requires us to consider metric components up to second order in z/r , which we obtain as

$$\begin{aligned} g_{tt} &= - \left[1 - \frac{2}{x^2} + \frac{z_\bullet^2}{x^6} \left(1 + \frac{2\chi_\bullet^2}{x^4} \right) \right], & g_{rr} &= \frac{1}{\mathcal{D}} \left[1 - \frac{z_\bullet^2}{x^6} \left(2 + \frac{1}{\mathcal{D}} \right) \left(1 - \frac{\chi_\bullet^2}{x^2} \right) \right], \\ g_{t\phi} &= - \frac{\chi_\bullet M_\bullet}{x^2} \left[2 - \frac{z_\bullet^2}{x^4} \left(3 + \frac{2\chi_\bullet^2}{x^4} \right) \right], & g_{rz} &= - \frac{z_\bullet}{x^2} \left(1 - \frac{1}{\mathcal{D}} \right), \\ g_{\phi\phi} &= M_\bullet^2 \left[\mathcal{A} x^4 - \frac{\chi_\bullet^2 z_\bullet^2}{x^4} \left(1 + \frac{5}{x^2} + \frac{2\chi_\bullet^2}{x^6} \right) \right], & g_{zz} &= 1 + \frac{z_\bullet^2}{\mathcal{D} x^6} \left[2 - \frac{\chi_\bullet^2}{x^4} \left(2 - \frac{\chi_\bullet^2}{x^2} \right) \right], \end{aligned} \quad (\text{A5})$$

with all other components equal to zero. Here, we have introduced $z_\bullet = z/M_\bullet$. The Christoffel symbols relevant for the below derivation, expanded up to first order in z/r , read:

$$\begin{aligned} \Gamma_{tt}^r &= \frac{\mathcal{D}}{x^4 M_\bullet}, & \Gamma_{tt}^z &= \frac{z_\bullet}{x^6 M_\bullet} \left(\mathcal{D} + \frac{2\chi_\bullet^2}{x^4} \right), \\ \Gamma_{t\phi}^r &= - \frac{\chi_\bullet \mathcal{D}}{x^4}, & \Gamma_{t\phi}^z &= - \frac{\chi_\bullet z_\bullet}{x^6} \left(2 + \mathcal{D} + \frac{2\chi_\bullet^2}{x^4} \right), \\ \Gamma_{\phi\phi}^r &= - \mathcal{D} x^2 M_\bullet \left(1 - \frac{\chi_\bullet^2}{x^6} \right), & \Gamma_{\phi\phi}^z &= \frac{z_\bullet M_\bullet}{x^2} \left[2 + \frac{\chi_\bullet^2}{x^4} \left(4 + \mathcal{D} + \frac{2\chi_\bullet^2}{x^4} \right) \right]. \end{aligned} \quad (\text{A6})$$

The energy-momentum tensor of accreting matter in this background spacetime is given by

$$T^{\mu\nu} = h\rho u^\mu u^\nu + pg^{\mu\nu} + t^{\mu\nu} + u^\mu q^\nu + u^\nu q^\mu, \quad (\text{A7})$$

where $h = (\rho + e + p)/\rho$ is the relativistic specific enthalpy, with e the internal energy density and p the pressure, and u^μ is the time-like 4-velocity of the fluid, $u_\mu u^\mu = -1$. The radiative energy flux vector of neutrinos is denoted by q^μ . Furthermore,

$$t^{\mu\nu} = -(2\eta\sigma^{\mu\nu} + 3\zeta\mathcal{P}^{\mu\nu}\Theta) = -\eta[\mathcal{P}^{\mu\alpha}\nabla_\alpha u^\nu + \mathcal{P}^{\nu\beta}\nabla_\beta u^\mu] + \mathcal{P}^{\mu\nu}(2\eta - 3\zeta)\Theta \quad (\text{A8})$$

denotes the viscous stress tensor as measured in the local rest frame of the baryonic fluid. Here, η and ζ are the shear and bulk viscosity, respectively (L. D. Landau & E. M. Lifshitz 2004), $\sigma^{\mu\nu} = \mathcal{P}^{\mu\alpha}\mathcal{P}^{\nu\beta}[\frac{1}{2}(\nabla_\alpha u_\beta + \nabla_\beta u_\alpha) - g_{\alpha\beta}\Theta]$ is the shear tensor, $\Theta = \frac{1}{3}\nabla_\mu u^\mu$ is the expansion, $\mathcal{P}^{\alpha\beta} = u^\alpha u^\beta + g^{\alpha\beta}$ is the projection tensor onto the dimensions orthogonal to u^μ . Both $t^{\mu\nu}$ and q^μ are orthogonal to the 4-velocity, i.e. $u_\mu t^{\mu\nu} = 0$ and $u_\mu q^\mu = 0$.

We make repeated use of the following properties or assumptions:

- (i) Due to the axisymmetric and stationary nature of the background spacetime, we neglect all azimuthal and temporal derivatives and set $\partial_\phi(\cdot) = 0$, $\partial_t(\cdot) = 0$.
- (ii) Due to the height-integrated nature of our one-dimensional disk model, we do not consider vertical fluid motion and set the four-velocity to $u^\mu = (u^t, u^r, u^\phi, 0)$.
- (iii) We assume quasi-circular motion, $|u^r| \ll |u^\phi|$, $|u^t|$, which implies $|u_z| \simeq |u^r|$. Together with (i), the expansion then vanishes to zero order in small quantities ($\Theta \simeq 0$).
- (iv) We assume the accretion flow to be rest-mass energy dominated, $\rho \gg e, p, |t^\mu{}_\nu|, |q^\mu|$.
- (v) Due to the thin nature of the disk, we neglect lateral neutrino radiation transport within the disk and only consider neutrino flux escaping from the disk in the z -direction. We thus set $q^\mu = (q^t, 0, 0, q^z)$, with $q^\mu q_\mu = 0$.

(vi) The normalization of u^μ and the orthogonality of $S^{\mu\nu}$ and q^μ with u^μ directly imply the following relations

$$\nabla_\mu(u_\nu u^\nu) = 0 \implies u_\nu \nabla_\mu u^\nu = 0, \quad (\text{A9})$$

$$\nabla_\mu(u_\nu t^{\mu\nu}) = 0 \implies t^{\mu\nu} \nabla_\mu u_\nu = -u_\nu \nabla_\mu t^{\mu\nu}, \quad (\text{A10})$$

$$\nabla_\mu(u_\nu q^\nu) = 0 \implies q_\nu \nabla_\mu u^\nu = -u_\nu \nabla_\mu q^\nu. \quad (\text{A11})$$

Furthermore, we compute stresses in the co-moving frame of the accreting fluid, which we approximate by the circular, geodesic motion with four-velocity $u^\phi = (u^t, 0, u^\phi, 0)$, where u^t and u^ϕ are given by Equation (A36). The tetrad vectors then read (I. D. Novikov & K. S. Thorne 1973)

$$e_{\hat{t}} = u^\mu, \quad e_{\hat{r}} = \mathcal{D}^{1/2} \partial_r, \quad e_{\hat{\phi}} = \frac{\mathcal{F}}{\mathcal{C}^{1/2} \mathcal{D}^{1/2} x} \partial_t + \left(\frac{\mathcal{B} \mathcal{D}^{1/2}}{\mathcal{A} \mathcal{C}^{1/2} x^2 M_\bullet} + \frac{\mathcal{F}}{\mathcal{A} \mathcal{C}^{1/2} \mathcal{D}^{1/2}} \frac{2\chi_\bullet}{x^7 M_\bullet} \right) \partial_\phi, \quad e_{\hat{z}} = \partial_z, \quad (\text{A12})$$

and the corresponding one-forms are

$$e^{\hat{t}} = \frac{\mathcal{G}}{\mathcal{C}^{1/2}} dt - \frac{\mathcal{F}}{\mathcal{C}^{1/2}} M_\bullet x d\phi, \quad e^{\hat{r}} = \frac{1}{\mathcal{D}^{1/2}} dr, \quad e^{\hat{\phi}} = -\frac{\mathcal{D}^{1/2}}{\mathcal{C}^{1/2} x} dt + \frac{\mathcal{B} \mathcal{D}^{1/2}}{\mathcal{C}^{1/2}} M_\bullet x^2 d\phi, \quad e^{\hat{z}} = dz. \quad (\text{A13})$$

Hats denote components relative to the co-moving frame; they are raised and lowered with the Minkowski metric $\eta_{\hat{\mu}\hat{\nu}} = \text{diag}(-1, 1, 1, 1)$. The tetrad frame is orthonormal in the sense that $e_{\hat{\alpha}}^\mu e_{\hat{\mu}}^\beta = \delta_{\hat{\alpha}}^{\hat{\beta}}$.

A.1. Baryon number conservation

In the absence of disk winds, baryon number is strictly conserved in the accretion disk,

$$\nabla_\mu(n_b u^\mu) = 0 \iff \partial_\mu(\sqrt{-g} n_b u^\mu) = 0. \quad (\text{A14})$$

Multiplying the latter expression by the baryon mass m_b and integrating over a spacetime volume $r \in [r, r + \Delta r]$, $\phi \in [0, 2\pi]$, $z \in [-H, H]$, and $t \in [t, \Delta t]$, one obtains

$$\dot{M} \equiv -4\pi H r \rho u^r = \text{const}. \quad (\text{A15})$$

The sign convention adopted here ensures that a positive accretion rate \dot{M} corresponds to matter falling into the black hole.

A.2. Lepton number conservation

Due to the loss of neutrinos via neutrino cooling, the lepton number is not strictly conserved in the accretion disk. We represent this loss of neutrinos by a sink term and express the conservation law of lepton number as

$$\nabla_\mu(n_b Y_{\text{lep}} u^\mu) = R, \quad (\text{A16})$$

where

$$Y_{\text{lep}} = \frac{n_{e^-} - n_{e^+} + n_{\nu_e} - n_{\bar{\nu}_e}}{n_b} = Y_e + \frac{n_{\nu_e} - n_{\bar{\nu}_e}}{n_b} \quad (\text{A17})$$

is the lepton number and R is the radiated lepton number per unit volume per unit time in the rest frame of the fluid. Furthermore, n_{e^+} and n_{e^-} are the number densities of positrons and electrons (Equation (18)), respectively, and n_{ν_e} and $n_{\bar{\nu}_e}$ are the number densities of thermalized electron neutrinos and antineutrinos within the disk (Equation (27)).

In terms of disk-height integrated quantities,

$$R = -\frac{1}{H}(\dot{n}_{\nu_e} - \dot{n}_{\bar{\nu}_e}), \quad (\text{A18})$$

where H is the half-thickness of the disk as usual and \dot{n}_{ν_e} and $\dot{n}_{\bar{\nu}_e}$ are the (height-integrated) radiated number fluxes of electron neutrinos and antineutrinos per unit area from one face of the disk (Equation (49)). The minus sign is chosen such that positive emissivities imply a sink term for the lepton number in Equation (A16). Expanding Equation (A14) as

$$\nabla_\mu(n_b u^\mu) = n_b \nabla_\mu u^\mu + u^r \partial_r n_b = 0, \quad (\text{A19})$$

the left-hand side of Equation (A16) can be rewritten as

$$\nabla_\mu (n_b Y_{\text{lep}} u^\mu) = u^\mu \nabla_\mu (n_b Y_e) + n_b Y_e \nabla_\mu u^\mu + u^\mu \nabla_\mu (n_{\nu_e} - n_{\bar{\nu}_e}) + (n_{\nu_e} - n_{\bar{\nu}_e}) \nabla_\mu u^\mu \quad (\text{A20})$$

$$= n_b u^r \partial_r Y_e + u^r \partial_r (n_{\nu_e} - n_{\bar{\nu}_e}) - \frac{n_{\nu_e} - n_{\bar{\nu}_e}}{n_b} u^r \partial_r n_b \quad (\text{A21})$$

$$= u^r \left[\frac{\rho}{m_p} \frac{dY_e}{dr} - (n_{\nu_e} - n_{\bar{\nu}_e}) \frac{1}{\rho} \frac{d\rho}{dr} + \frac{d(n_{\nu_e} - n_{\bar{\nu}_e})}{dr} \right]. \quad (\text{A22})$$

Therefore, the total lepton number balance, i.e. the equation of lepton number conservation height-integrated according to Equation (2), reads

$$H u^r \left[\frac{\rho}{m_p} \frac{dY_e}{dr} - (n_{\nu_e} - n_{\bar{\nu}_e}) \frac{1}{\rho} \frac{d\rho}{dr} + \frac{d(n_{\nu_e} - n_{\bar{\nu}_e})}{dr} \right] = (\dot{n}_{\bar{\nu}_e} - \dot{n}_{\nu_e}). \quad (\text{A23})$$

A.3. Energy-momentum conservation

We project the conservation law of energy and momentum, $\nabla_\nu T^{\mu\nu} = 0$, onto u^μ to obtain an energy balance equation as seen by a comoving observer,

$$u_\mu \nabla_\nu T^{\mu\nu} = 0, \quad (\text{A24})$$

as well as orthogonal to u^μ using the projection tensor $\mathcal{P}^{\alpha\beta} = u^\alpha u^\beta + g^{\alpha\beta}$ to obtain the momentum balance equation for the dimensions ($i = 1, 2, 3$) orthogonal to u^μ ,

$$(u^i u^\nu + g^{i\nu}) \nabla_\mu T^\mu{}_\nu = 0. \quad (\text{A25})$$

A.3.1. Energy conservation

Using baryon number conservation (A14) as well as the identities (A9) and (A11), we obtain from Equation (A24) the relation

$$u^\mu \nabla_\mu e + (e + p) \nabla_\mu u^\mu - u_\nu \nabla_\mu t^{\mu\nu} + \nabla_\mu q^\mu + q^\nu u^\mu \nabla_\mu u_\nu = 0. \quad (\text{A26})$$

Again making use of baryon number conservation, and assuming quasi-geodesic motion (acceleration $a^\nu \equiv u^\mu \nabla_\mu u^\nu \simeq 0$ to leading order), neglecting radial neutrino flux gradients (consistent with vertical transport only, see (v) above), one finds in an axisymmetric and stationary context

$$u^r \left(\partial_r e - \frac{e + p}{\rho} \partial_r \rho \right) + t^{\mu\nu} \nabla_\mu u_\nu + \frac{1}{\sqrt{|g|}} \partial_z (\sqrt{|g|} q^z) = 0. \quad (\text{A27})$$

We introduce the cooling rate per area of the disk as

$$F^- \equiv \int_0^H \frac{1}{\sqrt{|g|}} \partial_z (\sqrt{|g|} q^z) \sqrt{g_{zz}} dz = \int_0^H \partial_z q^z dz = q^z(z = H). \quad (\text{A28})$$

Furthermore, we write

$$u_\nu \nabla_\mu t^{\mu\nu} = -\frac{1}{2} t^{\mu\nu} (\nabla_\mu u_\nu + \nabla_\nu u_\mu) = -t^{\mu\nu} \sigma_{\mu\nu} = -t^{\hat{\mu}\hat{\nu}} \sigma_{\hat{\mu}\hat{\nu}} = -2t^{\hat{r}\hat{\phi}} \sigma_{\hat{r}\hat{\phi}}, \quad (\text{A29})$$

where hats denotes the components in the co-moving tetrad of the accreting fluid (cf. Equation (A12)). The shear tensor for quasi-geodesic motion is given by $\sigma_{\mu\nu} = \frac{1}{2} (\nabla_\mu u_\nu + \nabla_\nu u_\mu)$. In the co-moving tetrad frame, covariant derivatives reduce to partial derivatives, and one obtains with Equations (A12) and (A13) the only non-vanishing components

$$\sigma_{\hat{r}\hat{\phi}} = \sigma_{\hat{\phi}\hat{r}} = \frac{1}{2} \partial_{\hat{r}} u_{\hat{\phi}} = \frac{1}{2} e_{\hat{r}}^\mu e_{\hat{\phi}}^\nu \partial_\mu u_\nu = \frac{1}{2} e_{\hat{r}}^r e_{\hat{\phi}}^\phi \partial_r u^\nu = \gamma^2 r \mathcal{A} \partial_r \Omega = -\frac{3}{4} \frac{M^{1/2}}{r^{3/2}} \frac{\mathcal{D}}{\mathcal{C}}, \quad (\text{A30})$$

where $\gamma = \sqrt{-g_{tt}} u^t = \mathcal{D}^{1/2} \mathcal{A}^{-1/2} u^t$ is the Lorentz factor and where we have used Equation (A37) for the angular velocity. We can thus write viscous heating per unit area of the disk as

$$F^+ \equiv - \int_0^H t^{\mu\nu} \sigma_{\mu\nu} \sqrt{g_{zz}} dz = \frac{3}{2} \frac{M^{1/2}}{r^{3/2}} \frac{\mathcal{D}}{\mathcal{C}} \int_0^H t^{\hat{r}\hat{\phi}} dz. \quad (\text{A31})$$

Therefore, integrating Equation (A27) over height, we find

$$u^r \left[\frac{d(He)}{dr} - \frac{e + p}{\rho} \frac{d(\rho H)}{dr} \right] = F^+ - F^-. \quad (\text{A32})$$

A.3.2. *Radial momentum balance*

Direct evaluation of radial momentum balance ($i = 1$ in Equation (A25)) leads to leading order in velocity components

$$h\rho u^\mu \nabla_\mu u^r + g^{r\mu} \partial_\mu p + \nabla_\mu t^{\mu r} + q^\mu \nabla_\mu u^r = 0. \quad (\text{A33})$$

To leading order in small quantities, and neglecting radial pressure as well as shear gradients, consistent with quasi-circular motion, one thus finds

$$u^\mu \nabla_\mu u^r = 0 \quad \Longleftrightarrow \quad u^\mu (\partial_\mu u^r + \Gamma_{\mu\nu}^r u^\nu) = 0. \quad (\text{A34})$$

Again, to leading order in velocity components, this leads to the local balance equation

$$\Gamma_{\mu\nu}^r u^\mu u^\nu = 0, \quad (\text{A35})$$

which is identical to its height-integrated version. Together with $u_\mu u^\mu = -1$ to leading order in velocity components, and using the expressions for the Christoffel symbols in Equation (A6), yields explicit expressions for the velocity components,

$$u^t = \frac{\mathcal{B}}{\mathcal{C}^{1/2}}, \quad u^\phi = \frac{1}{x^3 M_\bullet \mathcal{C}^{1/2}}. \quad (\text{A36})$$

Therefore, the angular velocity is given by

$$\Omega = \frac{u^\phi}{u^t} = \frac{1}{x^3 M_\bullet \mathcal{B}} = \left(\frac{r^{3/2}}{M_\bullet^{1/2}} + \chi_\bullet M_\bullet \right)^{-1}. \quad (\text{A37})$$

A.3.3. *Vertical momentum balance*

Vertical momentum balance ($i = 3$ in Equation (A25)) reads

$$h\rho u^\mu \nabla_\mu u^z + g^{z\nu} \partial_\nu p + \nabla_\mu t^{\mu z} + q^z \nabla_\mu u^\mu + u^\mu \nabla_\mu q^z + q^\mu \nabla_\mu u^z = 0. \quad (\text{A38})$$

To lowest order in small quantities, and neglecting radial pressure gradients and shear gradients as above, one obtains

$$g^{zz} \partial_z p + \Gamma_{\mu\nu}^z u^\mu u^\nu = 0. \quad (\text{A39})$$

With the expressions (A6) and (A36), this simplifies to linear order in z/r to

$$\frac{\partial p}{\partial z} = -\frac{\rho z J}{x^6 M^2}. \quad (\text{A40})$$

Upon vertical integration across one half-disk using $p(z = H) = 0$, we find the midplane pressure $p_{1/2}$ due to one half-disk as

$$p_{1/2}(z = 0) = \frac{1}{2} \frac{J \rho H^2}{x^3 M_\bullet^2}. \quad (\text{A41})$$

The other half-disk contributes equally to the pressure in the midplane. Thus one obtains the equation of vertical balance as

$$\left(\frac{H}{r} \right)^2 = \frac{p}{\rho} \frac{r}{J M_\bullet}. \quad (\text{A42})$$

A.3.4. *Azimuthal momentum balance*

Azimuthal momentum balance is expressed by the $i = 2$ component of Equation (A25), from which we obtain

$$u_\phi u^r \partial_r p + h\rho u^\mu \nabla_\mu u_\phi + \nabla_\mu t^\mu_\phi + u_\phi u_\nu \nabla_\nu t^{\mu\nu} + q^\mu \nabla_\mu u_\phi + u^\mu \nabla_\mu q_\phi - u_\phi q^\nu u^\mu \nabla_\mu u_\nu = 0. \quad (\text{A43})$$

Neglecting radial pressure gradients as above, one has to leading order in small quantities

$$0 = \rho u^\mu \nabla_\mu u_\phi + \nabla_\mu t^\mu_\phi + u_\phi u_\nu \nabla_\nu t^{\mu\nu} \simeq \rho u^r \partial_r l + \frac{1}{r} \partial_r (r t^r_\phi) + l u_\nu \nabla_\mu t^{\mu\nu}. \quad (\text{A44})$$

Identifying $l = u_\phi$ as the specific angular momentum (angular momentum per unit rest-mass) and $r\rho u^r \equiv -\dot{m}/(2\pi) = \text{const.}$ as the accreted mass per height (which follows directly from Equation (A14)), expressing

$$t^r_\phi = e^r_{\hat{r}} e^{\hat{\phi}}_{\hat{\phi}} t_{\hat{r}\hat{\phi}} = r \mathcal{B} \mathcal{C}^{-1/2} \mathcal{D} t_{\hat{r}\hat{\phi}} \quad (\text{A45})$$

in terms of the stress components in the tetrad co-moving with the mean fluid flow (cf. Equations (A12) and (A13)), as well as re-expressing $u_\nu \nabla_\mu t^{\mu\nu}$ as in Equation (A29), we obtain the differential equation

$$\partial_r \left(r^2 \frac{\mathcal{B} \mathcal{D}}{\sqrt{\mathcal{C}}} t_{\hat{r}\hat{\phi}} - \frac{\dot{m}}{2\pi} l \right) + \frac{3}{2} \sqrt{\frac{M}{r}} \frac{\mathcal{D}}{\mathcal{C}} l t_{\hat{r}\hat{\phi}} = 0. \quad (\text{A46})$$

This equation is mathematically equivalent to the height-integrated equation (5.6.13) of I. D. Novikov & K. S. Thorne (1973). The solution can thus be obtained from the result in closed form of D. N. Page & K. S. Thorne (1974) by translating that to the present case,

$$t_{\hat{r}\hat{\phi}} = \frac{\dot{m}}{2\pi} \frac{M_\bullet^{1/2}}{r^{3/2}} \frac{\mathcal{C}^{1/2}}{\mathcal{B} \mathcal{D}} \mathcal{Q}. \quad (\text{A47})$$

Furthermore, adopting the usual α -viscosity ansatz for accretion disks, $\nu \equiv \eta/\rho = \frac{2}{3} \alpha c_s H$, where $c_s \equiv \sqrt{p/\rho}$ is the isothermal sound speed, we also obtain from Equation (A8) using vertical balance (A42)

$$t_{\hat{r}\hat{\phi}} = -2\eta \sigma_{\hat{r}\hat{\phi}} = \frac{3}{2} \eta \frac{M_\bullet^{1/2}}{r^{3/2}} \frac{\mathcal{D}}{\mathcal{C}} = \alpha p \frac{\mathcal{D}}{J^{1/2} \mathcal{C}}. \quad (\text{A48})$$

Equating the above two expressions for $t_{\hat{r}\hat{\phi}}$, we obtain

$$u^r = -\alpha c_s \sqrt{\frac{p}{\rho}} \frac{r^{1/2}}{M_\bullet^{1/2}} \frac{\mathcal{B} \mathcal{D}^2}{J^{1/2} \mathcal{C}^{3/2} \mathcal{Q}} = -\alpha c_s \frac{H}{r} S^{-1}. \quad (\text{A49})$$

Furthermore, integrating Equation (A47) over height using Equation (A15), the viscous heating per unit area of the disk (Equation (A31)) is given by the following closed expression:

$$F^+ = \frac{3}{2} \frac{M_\bullet}{r^3} \frac{\mathcal{Q}}{\mathcal{B} \mathcal{C}^{1/2}} \int_0^H (-r\rho u^r) \sqrt{g_{zz}} dz = \frac{3\dot{M} M_\bullet}{8\pi r^3} \frac{\mathcal{D}^2}{\mathcal{C}^2} S. \quad (\text{A50})$$

B. EQUATION OF STATE AND THERMODYNAMIC QUANTITIES

In this appendix, we compute the contributions to the plasma pressure, internal energy density, and the entropy from all species considered here (baryons, photons, electrons and positrons, as well as electron neutrinos and antineutrinos).

B.1. Baryons

The Helmholtz free energy of a multi-species ideal fluid can be written as (cf. L. D. Landau & E. M. Lifshitz 1980)

$$\mathcal{F}_b = -k_B T \sum_i N_i \ln \left[\frac{eV}{N_i} \frac{(2\pi m_i k_B T)^{3/2}}{h^3} Z_{\text{int},i} \right], \quad (\text{B51})$$

where $Z_{\text{int},i} = \sum_k g_{ik} \exp(-\epsilon_{ik}/k_B T)$ is the internal partition function of particle species i (the nuclear partition function in this case). Here, V denotes volume, N_i the number of particles of species i , and m_i their mass. Assuming a mix of free nucleons and α -particles ($i = \text{nuc}, \alpha$), each having one energy level (ground state), the spin statistical weights $g_i = 2I_i + 1$ are $g_{\text{nuc}} = 2$ (fermions) and $g_\alpha = 1$ (ground state, $I_\alpha = 0$). Choosing the zero-energy state to be the free nucleon state ($\epsilon_{\text{nuc}} = 0$, $\epsilon_\alpha = -E_{\text{bind}} = -(2m_p + 2m_n - m_\alpha)c^2 \simeq -28.30 \text{ MeV}$), we find the baryon pressure as

$$p_b = - \left(\frac{\partial \mathcal{F}_b}{\partial V} \right)_{T, N_i} = \frac{m_e c^2}{m_b} \rho \theta \left(X_f + \frac{1 - X_f}{4} \right). \quad (\text{B52})$$

The entropy per baryon in units of k_B reads

$$s_b = - \left(\frac{\partial \mathcal{F}_b}{\partial T} \right)_{V, N_i} = X_f \left\{ \frac{5}{2} - \ln \left[\frac{X_f \rho}{2m_b} \frac{h^3}{(2\pi m_b m_e c^2 \theta)^{3/2}} \right] \right\} + \frac{1 - X_f}{4} \left\{ \frac{5}{2} - \ln \left[\frac{(1 - X_f) \rho}{4m_b} \frac{h^3/4}{(2\pi m_\alpha m_e c^2 \theta)^{3/2}} \right] \right\} \quad (\text{B53})$$

The energy density is given by

$$e_b = \frac{1}{V}(\mathcal{F}_b + TS_b) = \frac{3}{2} \frac{m_e c^2}{m_b} \rho \theta \left(X_f + \frac{1 - X_f}{4} \right) - E_{\text{bind}} \frac{\rho}{m_b} \frac{1 - X_f}{4}, \quad (\text{B54})$$

where S_b denotes entropy.

B.2. Radiation

For photons in thermal equilibrium $\mu = 0$, the Helmholtz free energy equals the grand canonical potential $\mathbf{\Omega}$, and one can write (cf. L. D. Landau & E. M. Lifshitz 1980)

$$\mathcal{F}_\gamma = k_B T \frac{V}{\pi^2 c^3} \int_0^\infty d\omega \omega^2 \ln \left(1 - e^{-\hbar\omega/k_B T} \right) = -\frac{1}{3} a_r V T^4, \quad (\text{B55})$$

where $a_r = \pi^2 k_B^4 / (15 c^3 \hbar^3)$ is the radiation constant.

The entropy per baryon in units of k_B is given by

$$s_\gamma = -\frac{1}{V} \frac{m_b}{\rho} \left(\frac{\partial \mathcal{F}_\gamma}{\partial T} \right)_V = \frac{4}{3} \frac{a_r m_b m_e^3 c^6}{k_B^4} \frac{\theta^3}{\rho}, \quad (\text{B56})$$

the pressure reads

$$p_\gamma = - \left(\frac{\partial \mathcal{F}_\gamma}{\partial V} \right)_T = \frac{1}{3} \frac{a_r m_e^4 c^8}{k_B^4} \theta^4, \quad (\text{B57})$$

and the radiation energy density is given by

$$e_\gamma = \frac{1}{V} (\mathcal{F}_\gamma + TS_\gamma) = 3p_\gamma. \quad (\text{B58})$$

B.3. Leptons

Since a wide range of physical regimes are realized in different spatial parts of an accretion disk and across the wide parameter space considered here, we need to take arbitrary levels of relativity and degeneracy of leptons into account, without resorting to limiting cases. The Helmholtz free energy $\mathcal{F} = \mathbf{\Omega} + \mu N$ is most easily obtained via the grand canonical potential (cf. L. D. Landau & E. M. Lifshitz 1980)

$$\mathbf{\Omega} = -k_B T \frac{gV}{2\pi^2 \hbar^3} \int_0^\infty dp p^2 \ln \left[1 + e^{-(\epsilon - \mu)/k_B T} \right], \quad (\text{B59})$$

where $\epsilon = \sqrt{p^2 c^2 + m c^4}$ is the relativistic particle energy, g is the statistical weight ($g = 2$ for electrons and positrons, $g = 1$ for neutrinos), and m is the lepton mass. Introducing $\lambda_e \equiv \pi^{2/3} \hbar / m_e c$, and noting that $\mathbf{\Omega} = -pV$, one finds for electrons and positrons

$$p_{e^\pm} = \frac{1}{3} \frac{m_e c^2}{\lambda_e^3} \int_0^\infty d\xi \xi^4 (\xi^2 + 1)^{-1/2} f(\sqrt{\xi^2 + 1}, \mp \eta_e, \theta). \quad (\text{B60})$$

The number densities are given by

$$n_{e^\pm} = -\frac{1}{V} \left(\frac{\partial \mathbf{\Omega}_{e^\pm}}{\partial \mu_{e^\pm}} \right)_{T,V} = \frac{1}{\lambda_e^3} \int_0^\infty d\xi \xi^2 f(\sqrt{\xi^2 + 1}, \mp \eta_e, \theta), \quad (\text{B61})$$

the corresponding energy density by

$$e_{e^\pm} = \frac{m_e c^2}{\lambda_e^3} \int_0^\infty d\xi \xi^2 (\xi^2 + 1)^{1/2} f(\sqrt{\xi^2 + 1}, \mp \eta_e, \theta), \quad (\text{B62})$$

and the entropy per baryon in units of k_B is

$$s_{e^\pm} = \frac{m_b}{\rho} \left(\frac{e_{e^\pm} + p_{e^\pm}}{m_e c^2 \theta} \pm n_{e^\pm} \eta_e \right). \quad (\text{B63})$$

For electron neutrinos and antineutrinos, it is necessary to distinguish between the transparent (free-streaming) and opaque (thermalized) regimes. In the thermalized regime, neutrinos and antineutrinos are modeled by a massless ideal Fermi gas, for which one obtains from Equation (B59), together with $\Omega = -pV$, the pressure as

$$p_{\nu_e, \bar{\nu}_e}^{\text{opaque}} = \frac{1}{6} \frac{m_e c^2}{\lambda_e^3} \theta^4 \int_0^\infty d\xi \frac{\xi^3}{\exp(\xi \mp \eta_\nu) + 1}. \quad (\text{B64})$$

Here, the upper sign refers to electron neutrinos, whereas the lower sign to the antineutrinos. The corresponding energy densities are given by

$$e_{\nu_e, \bar{\nu}_e}^{\text{opaque}} = 3p_{\nu_e, \bar{\nu}_e}^{\text{opaque}}, \quad (\text{B65})$$

and the number densities are obtained as

$$n_{\nu_e, \bar{\nu}_e}^{\text{opaque}} = -\frac{1}{V} \left(\frac{\partial \Omega_{\nu_e, \bar{\nu}_e}^{\text{opaque}}}{\partial \mu_{\nu_e, \bar{\nu}_e}} \right)_{T, V} = \frac{1}{2} \frac{\theta^3}{\lambda_e^3} \int_0^\infty d\xi \frac{\xi^2}{\exp(\xi \mp \eta_\nu) + 1}. \quad (\text{B66})$$

We include the internal energy density of the thermalized neutrinos and anti-neutrinos in the equation of state as

$$e_\nu = x_\nu e_{\nu_e}^{\text{opaque}}, \quad e_{\bar{\nu}} = x_{\bar{\nu}} e_{\bar{\nu}_e}^{\text{opaque}}, \quad (\text{B67})$$

where x_ν and $x_{\bar{\nu}}$ are transition parameters defined in Equation (31). The latter smoothly interpolate between zero (transparent regime) and unity (optically thick regime) for the two species. The consistent partial pressures for the equation of state are then given by $p_{\nu, \bar{\nu}} = e_{\nu, \bar{\nu}}/3$.

C. DISK OUTFLOW MODEL

Here, we construct a simplified accretion disk outflow model. It is mainly used to estimate the number of neutrons Δ_n created per seed during a potential νp -process (see Equation (90)).

First, we estimate as a function of time the distance R_{ej} to the disk, the temperature T_{ej} , and the density ρ_{ej} of a fluid element ejected from the disk with the initial distance to the black hole R_0 , initial (local disk) temperature T_0 , and (local disk) density at ejection ρ_0 . We assume that the outflows, once unbound from the black hole-disk potential, approach roughly spherical expansion. The continuity equation $\nabla \cdot (\rho \mathbf{v}) = 0$ for the outflow with velocity \mathbf{v} then implies $\rho_{\text{ej}} \propto R_{\text{ej}}^{-2}$ for $v = v_{\text{ej}} = \text{const.}$. We assume adiabatic expansion, implying $T_{\text{ej}} \propto \rho_{\text{ej}}^{1/3}$ if relativistic particles (e^\pm, γ) dominate the specific entropy (Equations (B56) and (B63) with (B64)) or $T_{\text{ej}} \propto \rho_{\text{ej}}^{2/3}$ if baryons dominate the specific entropy (Equation (B53)).

We assume a constant ejection speed $v_{\text{ej}} = v_\infty$, given by the asymptotic Lorentz factor $\Gamma_\infty = -hu_0$. In launching the disk outflows, we follow the results of numerical simulations (R. Fernández & B. D. Metzger 2013; D. M. Siegel & B. D. Metzger 2018; A. Agarwal et al. 2025) and assume that the disk winds are typically marginally unbound at launch ($hu_0 \simeq -1$) and that the outflow speeds are primarily set by α -particle recombination, i.e. we set (compare Appendix B) $h = 1 + \epsilon_{\text{bind}}$, with $\epsilon_{\text{bind}} = E_{\text{bind}}(1 - X_{f, \text{rec}})/(4m_b)$ once the outflows are launched. The mass fraction $X_{f, \text{rec}}$ of free nucleons remaining after recombination is determined by the number of neutrons under neutron-rich conditions and by the number of protons under proton-rich conditions, leading to $X_{f, \text{rec}} = |1 - 2Y_{e0}|$, where we take Y_{e0} as the local disk electron-fraction. For values of $Y_{e0} \sim 0.1 - 0.7$, one obtains ejecta velocities in the range of $v_{\text{ej}} = v_\infty \simeq 0.05 - 0.12c$. The corresponding expansion timescale is given by $\tau \approx R_{\text{ej}}/v_{\text{ej}}$.

To compute Δ_n , one needs to determine the ratio Y_p/Y_{heavy} , the reaction rate $\lambda_{\bar{\nu}_e p}$, and the time window in which the ejecta stays in the temperature regime between 1 – 3 GK.

At the end of the recombination process and assuming proton-rich conditions, $X_p = Y_p = X_{f, \text{rec}} = |1 - 2Y_{e0}|$, since all neutrons are either integrated into α -particles or into heavier nuclei. Therefore, we can replace the ratio in Equation (90) by

$$\frac{Y_p}{Y_{\text{heavy}}} = \bar{A} \frac{X_p}{X_{\text{heavy}}}, \quad (\text{C68})$$

where $\bar{A} \approx 60$ is the average mass of the heavy seed particles formed after α recombination (Section 5.5; C. Fröhlich et al. 2006; J. Pruet et al. 2006). The ratio X_p/X_{heavy} , in turn, strongly depends on entropy ($\propto s^3$; R. D. Hoffman et al. 1997). Given the typical entropies of $\langle s \rangle \gtrsim 100$ in regions with $Y_e > 0.5$ (Figures 1 and 2), $X_{\text{heavy}} \approx 0.01(1 - X_p)$

provides a good approximation to the mass fraction of seeds at the onset of the νp -process. This estimate is based on results from nucleosynthesis calculations performed with nuclear reaction networks, which show that for entropies $s \sim 100$, only $\lesssim 1\%$ of the mass is in atoms heavier than ${}^4\text{He}$ (α -rich freeze-out'; R. D. Hoffman et al. 1997).

In order to estimate the reaction rate $\lambda_{\bar{\nu}_e p}$, we model the accretion disk as a neutrino ‘light bulb’ that irradiates the outflows using the approximation (Y.-Z. Qian & S. E. Woosley 1996)

$$\lambda_{\bar{\nu}_e p} \approx \frac{1 + 3g_a^2}{4\pi^2} \frac{G_F^2}{(\hbar c)^4} \frac{L_{\bar{\nu}_e}}{R_{\text{ej}}^2} \left(1.2 \langle E_{\bar{\nu}_e} \rangle - 2Q + \frac{Q^2}{\langle E_{\bar{\nu}_e} \rangle} \right) \quad (\text{C69})$$

$$\approx 0.06 \left(\frac{L_{\bar{\nu}_e}}{10^{52} \text{ erg s}^{-1}} \right) \left(\frac{R_{\text{ej}}}{10^8 \text{ cm}} \right)^{-2} \left(\frac{\langle E_{\bar{\nu}_e} \rangle}{10 \text{ MeV}} - 0.216 \right), \quad (\text{C70})$$

where $L_{\bar{\nu}_e}$ is the antineutrino luminosity of the disk and $\langle E_{\bar{\nu}_e} \rangle$ is the corresponding average antineutrino energy.

The average antineutrino energy is given by $\langle E_{\bar{\nu}_e} \rangle = F_{\bar{\nu}_e}^- / \dot{n}_{\bar{\nu}_e}$, where the energy and number flux $F_{\bar{\nu}_e}^-$ and $\dot{n}_{\bar{\nu}_e}$ are given by the electron antineutrino expressions of Equations (30) and (49), respectively. We compute the total disk contribution to the above expression by radial integration,

$$L_{\bar{\nu}_e} \left(1.2 \langle E_{\bar{\nu}_e} \rangle - 2Q + \frac{Q^2}{\langle E_{\bar{\nu}_e} \rangle} \right) = \int_{r_{\text{ISCO}}}^{r_{\text{out}}} 2\pi r \left[1.2 \frac{(F_{\bar{\nu}_e}^-(r))^2}{\dot{n}_{\bar{\nu}_e}(r)} - 2Q F_{\bar{\nu}_e}^-(r) + Q^2 \dot{n}_{\bar{\nu}_e}(r) \right] dr,$$

where we take r_{out} as the outer boundary of the disk. Our results are insensitive to the choice of r_{out} as long as $r_{\text{out}} \gg r_g$ so that it encompasses the regions that dominate the neutrino flux.

To estimate the prospects for a successful νp -process, we take ejecta conditions in the most optimistic scenario for a νp -process: We follow fluid elements ejected at $R_{\text{launch}} = r(Y_e = \max(Y_e))$ from the disk, i.e. launched from the region in the disk with the most proton-rich conditions. We use the previously described outflow model to determine the time window in which the ejecta reside between $T = 3 \text{ GK}$ and $T = 1.5 \text{ GK}$, together with the corresponding distances R_{ej} . These time limits are used to solve the integral in Equation (90) and the corresponding trajectory $R_{\text{ej}}(t)$ is used in Equation (C69).

REFERENCES

- Abbott, B. P., Abbott, R., Abbott, T. D., & et al. 2017, ApJL, 848, L12, doi: [10.3847/2041-8213/aa91c9](https://doi.org/10.3847/2041-8213/aa91c9)
- Abbott, R., Abbott, T. D., Abraham, S., & et al. 2020, PhRvL, 125, 101102, doi: [10.1103/PhysRevLett.125.101102](https://doi.org/10.1103/PhysRevLett.125.101102)
- Agarwal, A., Siegel, D. M., Metzger, B. D., & et al. 2025, arXiv:2503.15729, doi: [10.48550/arXiv.2503.15729](https://doi.org/10.48550/arXiv.2503.15729)
- Anand, S., Barnes, J., Yang, S., & et al. 2024, The Astrophysical Journal, 962, 68, doi: [10.3847/1538-4357/ad11df](https://doi.org/10.3847/1538-4357/ad11df)
- Arcones, A., & Thielemann, F.-K. 2022, The Astronomy and Astrophysics Review, 31, 1, doi: [10.1007/s00159-022-00146-x](https://doi.org/10.1007/s00159-022-00146-x)
- Balbus, S. A., & Hawley, J. F. 1998, Rev. Mod. Phys., 70, 1, doi: [10.1103/RevModPhys.70.1](https://doi.org/10.1103/RevModPhys.70.1)
- Barkat, Z., Rakavy, G., & Sack, N. 1967, Physical Review Letters, 18, 379, doi: [10.1103/PhysRevLett.18.379](https://doi.org/10.1103/PhysRevLett.18.379)
- Barnes, J., & Duffell, P. C. 2023, The Astrophysical Journal, 952, 96, doi: [10.3847/1538-4357/acdb67](https://doi.org/10.3847/1538-4357/acdb67)
- Barnes, J., Duffell, P. C., Liu, Y., & et al. 2018, ApJ, 860, 38, doi: [10.3847/1538-4357/aabf84](https://doi.org/10.3847/1538-4357/aabf84)
- Barnes, J., & Kasen, D. 2013, ApJ, 775, 18, doi: [10.1088/0004-637X/775/1/18](https://doi.org/10.1088/0004-637X/775/1/18)
- Barnes, J., & Metzger, B. D. 2022, ApJ, 939, L29, doi: [10.3847/2041-8213/ac9b41](https://doi.org/10.3847/2041-8213/ac9b41)
- Batziou, E., Glas, R., Janka, H.-T., & et al. 2024, arXiv:2412.02756, doi: [10.48550/arXiv.2412.02756](https://doi.org/10.48550/arXiv.2412.02756)
- Beloborodov, A. M. 1999, ASP Conf. Ser., 161, 295, <https://arxiv.org/abs/astro-ph/9901108>
- Beloborodov, A. M. 2003, ApJ, 588, 931, doi: [10.1086/374217](https://doi.org/10.1086/374217)
- Beloborodov, A. M., Abramowicz, M. A., & Novikov, I. D. 1997, ApJ, 491, 267, doi: [10.1086/304956](https://doi.org/10.1086/304956)
- Beniamini, P., Hotokezaka, K., & Piran, T. 2016, ApJ, 832, 149, doi: [10.3847/0004-637X/832/2/149](https://doi.org/10.3847/0004-637X/832/2/149)
- Berger, E., Fong, W., & Chornock, R. 2013, ApJL, 774, L23, doi: [10.1088/2041-8205/774/2/L23](https://doi.org/10.1088/2041-8205/774/2/L23)
- Blanchard, P. K., Villar, V. A., Chornock, R., & et al. 2024, Nature Astronomy, 8, 774, doi: [10.1038/s41550-024-02237-4](https://doi.org/10.1038/s41550-024-02237-4)
- Bond, J. R., Arnett, W. D., & Carr, B. J. 1984, ApJ, 280, 825, doi: [10.1086/162057](https://doi.org/10.1086/162057)

- Bonetti, M., Perego, A., Dotti, M., & et al. 2019, MNRAS, 490, 296, doi: [10.1093/mnras/stz2554](https://doi.org/10.1093/mnras/stz2554)
- Burbidge, E. M., Burbidge, G. R., Fowler, W. A., & et al. 1957, Rev. Mod. Phys., 29, 547, doi: [10.1103/RevModPhys.29.547](https://doi.org/10.1103/RevModPhys.29.547)
- Burns, E., Svinkin, D., Fenimore, E., & et al. 2023, ApJL, 946, L31, doi: [10.3847/2041-8213/acc39c](https://doi.org/10.3847/2041-8213/acc39c)
- Burrows, A., Reddy, S., & Thompson, T. A. 2006, Nuclear Physics A, 777, 356, doi: [10.1016/j.nuclphysa.2004.06.012](https://doi.org/10.1016/j.nuclphysa.2004.06.012)
- Cameron, A. G. W. 1957, Publ. Astron. Soc. Pac., 69, 201, doi: [10.1086/127051](https://doi.org/10.1086/127051)
- Cantiello, M., Jermyn, A. S., & Lin, D. N. C. 2021, ApJ, 910, 94, doi: [10.3847/1538-4357/abdf4f](https://doi.org/10.3847/1538-4357/abdf4f)
- Chandrasekhar, S. 1964, Astrophys. J., 140, 417
- Chen, H.-Y., Landry, P., Read, J. S., & et al. 2025, ApJ, 985, 154, doi: [10.3847/1538-4357/add0af](https://doi.org/10.3847/1538-4357/add0af)
- Chen, W.-X., & Beloborodov, A. M. 2007, ApJ, 657, 383, doi: [10.1086/508923](https://doi.org/10.1086/508923)
- Cheong, P. C.-K., Pitik, T., Longo Micchi, L. F., & et al. 2025, ApJL, 978, L38, doi: [10.3847/2041-8213/ada1cc](https://doi.org/10.3847/2041-8213/ada1cc)
- Christie, I. M., Lalakos, A., Tchekhovskoy, A., & et al. 2019, MNRAS, 490, 4811, doi: [10.1093/mnras/stz2552](https://doi.org/10.1093/mnras/stz2552)
- Combi, L., & Siegel, D. M. 2023, PhRvL, 131, 231402, doi: [10.1103/PhysRevLett.131.231402](https://doi.org/10.1103/PhysRevLett.131.231402)
- Combi, L., Thompson, C., Siegel, D. M., & et al. 2025, ApJ, 987, 71, doi: [10.3847/1538-4357/addc57](https://doi.org/10.3847/1538-4357/addc57)
- Côté, B., Lugaro, M., Reifarh, R., & et al. 2019, ApJ, 878, 156, doi: [10.3847/1538-4357/ab21d1](https://doi.org/10.3847/1538-4357/ab21d1)
- Cowan, J. J., Sneden, C., Lawler, J. E., & et al. 2021, Rev. Mod. Phys., 93, 015002, doi: [10.1103/RevModPhys.93.015002](https://doi.org/10.1103/RevModPhys.93.015002)
- De, S., & Siegel, D. M. 2021, The Astrophysical Journal, 921, 94, doi: [10/gpb5w6](https://doi.org/10/gpb5w6)
- Dean, C., & Fernández, R. 2024, PhRvD, 110, 083024, doi: [10.1103/PhysRevD.110.083024](https://doi.org/10.1103/PhysRevD.110.083024)
- Dessart, L., Burrows, A., Livne, E., & et al. 2006, ApJ, 645, 534
- Dittmann, A. J., Cantiello, M., & Jermyn, A. S. 2021, ApJ, 916, 48, doi: [10.3847/1538-4357/ac042c](https://doi.org/10.3847/1538-4357/ac042c)
- Farmer, R., Renzo, M., de Mink, S. E., & et al. 2019, ApJ, 887, 53, doi: [10.3847/1538-4357/ab518b](https://doi.org/10.3847/1538-4357/ab518b)
- Fernández, R., & Metzger, B. D. 2013, MNRAS, 435, 502, doi: [10.1093/mnras/stt1312](https://doi.org/10.1093/mnras/stt1312)
- Fernández, R., Tchekhovskoy, A., Quataert, E., & et al. 2019, MNRAS, 482, 3373, doi: [10.1093/mnras/sty2932](https://doi.org/10.1093/mnras/sty2932)
- Fröhlich, C., Martínez-Pinedo, G., Liebendörfer, M., & et al. 2006, Physical Review Letters, 96, 142502, doi: [10.1103/PhysRevLett.96.142502](https://doi.org/10.1103/PhysRevLett.96.142502)
- Fryer, C. L., Woosley, S. E., & Heger, A. 2001, ApJ, 550, 372, doi: [10.1086/319719](https://doi.org/10.1086/319719)
- Fujibayashi, S., Kiuchi, K., Nishimura, N., & et al. 2018, ApJ, 860, 64, doi: [10.3847/1538-4357/aabafd](https://doi.org/10.3847/1538-4357/aabafd)
- Fujibayashi, S., Shibata, M., Wanajo, S., & et al. 2020, PhRvD, 101, 083029, doi: [10.1103/PhysRevD.101.083029](https://doi.org/10.1103/PhysRevD.101.083029)
- Gammie, C. F. 2001, ApJ, 553, 174, doi: [10.1086/320631](https://doi.org/10.1086/320631)
- Gottlieb, O., Renzo, M., Metzger, B. D., & et al. 2024, ApJL, 976, L13, doi: [10.3847/2041-8213/ad8563](https://doi.org/10.3847/2041-8213/ad8563)
- Haemmerlé, L., Woods, T. E., Klessen, R. S., & et al. 2018, The Astrophysical Journal Letters, 853, L3, doi: [10.3847/2041-8213/aaa462](https://doi.org/10.3847/2041-8213/aaa462)
- Hansen, T. T., Simon, J. D., Marshall, J. L., & et al. 2017, ApJ, 838, 44, doi: [10.3847/1538-4357/aa634a](https://doi.org/10.3847/1538-4357/aa634a)
- Harris, C. R., Millman, K. J., van der Walt, S. J., & et al. 2020, Nature, 585, 357, doi: [10.1038/s41586-020-2649-2](https://doi.org/10.1038/s41586-020-2649-2)
- Hawley, J. F., & Balbus, S. A. 2002, The Astrophysical Journal, 573, 738, doi: [10.1086/340765](https://doi.org/10.1086/340765)
- Heger, A., Woosley, S. E., & Spruit, H. C. 2005, Astrophys. J., 626, 350, doi: [10.1086/429868](https://doi.org/10.1086/429868)
- Hoffman, R. D., Woosley, S. E., & Qian, Y. Z. 1997, ApJ, 482, 951, doi: [10.1086/304181](https://doi.org/10.1086/304181)
- Horowitz, C. J., Arcones, A., Côté, B., & et al. 2019, J. Phys. G: Nucl. Part. Phys., 46, 083001, doi: [10.1088/1361-6471/ab0849](https://doi.org/10.1088/1361-6471/ab0849)
- Hotokezaka, K., Piran, T., & Paul, M. 2015, Nature Phys., 11, 1042, doi: [10.1038/nphys3574](https://doi.org/10.1038/nphys3574)
- Hunter, J. D. 2007, Computing in Science & Engineering, 9, 90, doi: [10.1109/MCSE.2007.55](https://doi.org/10.1109/MCSE.2007.55)
- Issa, D., Gottlieb, O., Metzger, B. D., & et al. 2025, ApJL, 985, L26, doi: [10.3847/2041-8213/adc694](https://doi.org/10.3847/2041-8213/adc694)
- Janiuk, A. 2014, Astronomy and Astrophysics, 568, A105, doi: [10.1051/0004-6361/201423822](https://doi.org/10.1051/0004-6361/201423822)
- Jermyn, A. S., Dittmann, A. J., Cantiello, M., & et al. 2021, ApJ, 914, 105, doi: [10.3847/1538-4357/abfb67](https://doi.org/10.3847/1538-4357/abfb67)
- Ji, A. P., Frebel, A., Chiti, A., & et al. 2016, Nature, 531, 610, doi: [10.1038/nature17425](https://doi.org/10.1038/nature17425)
- Just, O., Aloy, M. A., Obergaulinger, M., & et al. 2022, ApJL, 934, L30, doi: [10.3847/2041-8213/ac83a1](https://doi.org/10.3847/2041-8213/ac83a1)
- Kann, D. A., Agayeva, S., Aivazyan, V., & et al. 2023, The Astrophysical Journal Letters, 948, L12, doi: [10.3847/2041-8213/acc8d0](https://doi.org/10.3847/2041-8213/acc8d0)
- Kasen, D., Badnell, N. R., & Barnes, J. 2013, ApJ, 774, 25, doi: [10.1088/0004-637X/774/1/25](https://doi.org/10.1088/0004-637X/774/1/25)
- Kawanaka, N., & Mineshige, S. 2007, ApJ, 662, 1156, doi: [10.1086/517985](https://doi.org/10.1086/517985)
- Kimura, K., Hosokawa, T., Sugimura, K., & et al. 2023, ApJ, 950, 184, doi: [10.3847/1538-4357/acda8e](https://doi.org/10.3847/1538-4357/acda8e)
- Kirby, E. N., Ji, A. P., & Kovalev, M. 2023, ApJ, 958, 45, doi: [10.3847/1538-4357/acf309](https://doi.org/10.3847/1538-4357/acf309)
- Kobayashi, C., Mandel, I., Belczynski, K., & et al. 2023, ApJL, 943, L12, doi: [10.3847/2041-8213/acad82](https://doi.org/10.3847/2041-8213/acad82)

- Komissarov, S. S., & Barkov, M. V. 2010, *MNRAS*, 402, L25, doi: [10.1111/j.1745-3933.2009.00792.x](https://doi.org/10.1111/j.1745-3933.2009.00792.x)
- Landau, L. D., & Lifshitz, E. M. 1980, *Statistical Physics*. Pt.2 (Oxford Pergamon Press, 1980)
- Landau, L. D., & Lifshitz, E. M. 2004, *Fluid Mechanics*, Course of Theoretical Physics, Volume 6 (Oxford: Elsevier Butterworth-Heinemann)
- Lerner, Y., Stone, N. C., & Ofengeim, D. D. 2025, arXiv:2505.21617, doi: [10.48550/arXiv.2505.21617](https://doi.org/10.48550/arXiv.2505.21617)
- Lesage, S., Veres, P., Briggs, M. S., & et al. 2023, *ApJL*, 952, L42, doi: [10.3847/2041-8213/ace5b4](https://doi.org/10.3847/2041-8213/ace5b4)
- Li, L.-X., & Paczyński, B. 1998, *ApJL*, 507, L59, doi: [10.1086/311680](https://doi.org/10.1086/311680)
- Li, X., & Siegel, D. M. 2021, *PhRvL*, 126, 251101, doi: [10.1103/PhysRevLett.126.251101](https://doi.org/10.1103/PhysRevLett.126.251101)
- Lippuner, J., Fernández, R., Roberts, L. F., & et al. 2017, *MNRAS*, 472, 904, doi: [10.1093/mnras/stx1987](https://doi.org/10.1093/mnras/stx1987)
- Lippuner, J., & Roberts, L. F. 2015, *ApJ*, 815, 82, doi: [10.1088/0004-637X/815/2/82](https://doi.org/10.1088/0004-637X/815/2/82)
- MacFadyen, A. I., & Woosley, S. E. 1999, *ApJ*, 524, 262, doi: [10.1086/307790](https://doi.org/10.1086/307790)
- Malesani, D. B., Levan, A. J., Izzo, L., & et al. 2025, arXiv:2302.07891, doi: [10.48550/arXiv.2302.07891](https://doi.org/10.48550/arXiv.2302.07891)
- Marchant, P., & Moriya, T. J. 2020, *A&A*, 640, L18, doi: [10.1051/0004-6361/202038902](https://doi.org/10.1051/0004-6361/202038902)
- Matteucci, F., Romano, D., Arcones, A., & et al. 2014, *MNRAS*, 438, 2177, doi: [10.1093/mnras/stt2350](https://doi.org/10.1093/mnras/stt2350)
- Mészáros, P., & Rees, M. J. 2010, *ApJ*, 715, 967, doi: [10.1088/0004-637X/715/2/967](https://doi.org/10.1088/0004-637X/715/2/967)
- Metzger, B. D. 2020, *Living Rev. Relativity*, 23, 1, doi: [10.1007/s41114-019-0024-0](https://doi.org/10.1007/s41114-019-0024-0)
- Metzger, B. D., Hui, L., & Cantiello, M. 2024, *ApJL*, 971, L34, doi: [10.3847/2041-8213/ad6990](https://doi.org/10.3847/2041-8213/ad6990)
- Metzger, B. D., Martínez-Pinedo, G., Darbha, S., & et al. 2010, *MNRAS*, 406, 2650, doi: [10.1111/j.1365-2966.2010.16864.x](https://doi.org/10.1111/j.1365-2966.2010.16864.x)
- Metzger, B. D., Piro, A. L., & Quataert, E. 2008a, *MNRAS*, doi: [10.1111/j.1365-2966.2008.13789.x](https://doi.org/10.1111/j.1365-2966.2008.13789.x)
- Metzger, B. D., Piro, A. L., & Quataert, E. 2009, *MNRAS*, 396, 304, doi: [10.1111/j.1365-2966.2008.14380.x](https://doi.org/10.1111/j.1365-2966.2008.14380.x)
- Metzger, B. D., Thompson, T. A., & Quataert, E. 2008b, *ApJ*, 676, 1130, doi: [10.1086/526418](https://doi.org/10.1086/526418)
- Meyer, B. S. 1994, *ARA&A*, 32, 153, doi: [10.1146/annurev.aa.32.090194.001101](https://doi.org/10.1146/annurev.aa.32.090194.001101)
- Miller, J. M., Ryan, B. R., Dolence, J. C., & et al. 2019, *PhRvD*, 100, 023008, doi: [10.1103/PhysRevD.100.023008](https://doi.org/10.1103/PhysRevD.100.023008)
- Miller, J. M., Sprouse, T. M., Fryer, C. L., & et al. 2020, *ApJ*, 902, 66, doi: [10.3847/1538-4357/abb4e3](https://doi.org/10.3847/1538-4357/abb4e3)
- Nagele, C., Umeda, H., Takahashi, K., & et al. 2022, *MNRAS*, 517, 1584, doi: [10.1093/mnras/stac2495](https://doi.org/10.1093/mnras/stac2495)
- Naidu, R. P., Ji, A. P., Conroy, C., & et al. 2022, *ApJL*, 926, L36, doi: [10.3847/2041-8213/ac5589](https://doi.org/10.3847/2041-8213/ac5589)
- Nedora, V., Bernuzzi, S., Radice, D., & et al. 2019, *ApJ*, 886, L30, doi: [10.3847/2041-8213/ab5794](https://doi.org/10.3847/2041-8213/ab5794)
- Novikov, I. D., & Thorne, K. S. 1973, in *Black Holes (Les Astres Occlus)*, 343–450
- Paczynski, B. 1978, *Acta Astron.*, 28, 91
- Page, D. N., & Thorne, K. S. 1974, *ApJ*, 191, 499, doi: [10.1086/152990](https://doi.org/10.1086/152990)
- Penna, R. F., Sadowski, A., Kulkarni, A. K., & et al. 2013, *MNRAS*, 428, 2255, doi: [10.1093/mnras/sts185](https://doi.org/10.1093/mnras/sts185)
- Piro, A. L., & Pfahl, E. 2007, *ApJ*, 658, 1173, doi: [10.1086/511672](https://doi.org/10.1086/511672)
- Pruet, J., Hoffman, R. D., Woosley, S. E., & et al. 2006, *The Astrophysical Journal*, 644, 1028, doi: [10.1086/503891](https://doi.org/10.1086/503891)
- Psaltis, A., Jacobi, M., Montes, F., & et al. 2024, *The Astrophysical Journal*, 966, 11, doi: [10.3847/1538-4357/ad2dfb](https://doi.org/10.3847/1538-4357/ad2dfb)
- Qian, Y.-Z., & Woosley, S. E. 1996, *ApJ*, 471, 331, doi: [10.1086/177973](https://doi.org/10.1086/177973)
- Rastinejad, J. C., Fong, W., Kilpatrick, C. D., & et al. 2025, *ApJ*, 979, 190, doi: [10.3847/1538-4357/ad9c77](https://doi.org/10.3847/1538-4357/ad9c77)
- Rastinejad, J. C., Fong, W., Levan, A. J., & et al. 2024, *ApJ*, 968, 14, doi: [10.3847/1538-4357/ad409c](https://doi.org/10.3847/1538-4357/ad409c)
- Renzo, M., Farmer, R., Justham, S., & et al. 2020, *Astronomy and Astrophysics*, 640, A56, doi: [10.1051/0004-6361/202037710](https://doi.org/10.1051/0004-6361/202037710)
- Riffert, H., & Herold, H. 1995, *The Astrophysical Journal*, 450, 508, doi: [10.1086/176161](https://doi.org/10.1086/176161)
- Ryan, G. 2022, *Geoffryan/Fdlo*,
- Shakura, N. I., & Sunyaev, R. A. 1973, *A&A*, 24, 337
- Shapiro, S. L., & Teukolsky, S. A. 1983, *Black Holes, White Dwarfs, and Neutron Stars* (New York: John Wiley & Sons)
- Shibata, M., Fujibayashi, S., Wanajo, S., & et al. 2025, arXiv:2502.02077, doi: [10.48550/arXiv.2502.02077](https://doi.org/10.48550/arXiv.2502.02077)
- Siegel, D. M. 2019, *Eur. Phys. J. A*, 55, 203, doi: [10.1140/epja/i2019-12888-9](https://doi.org/10.1140/epja/i2019-12888-9)
- Siegel, D. M. 2022, *Nature Rev. Phys.*, 4, 306, doi: [10.1038/s42254-022-00439-1](https://doi.org/10.1038/s42254-022-00439-1)
- Siegel, D. M., Agarwal, A., Barnes, J., & et al. 2022, *ApJ*, 941, 100, doi: [10.3847/1538-4357/ac8d04](https://doi.org/10.3847/1538-4357/ac8d04)
- Siegel, D. M., Barnes, J., & Metzger, B. D. 2019, *Nature*, 569, 241, doi: [10.1038/s41586-019-1136-0](https://doi.org/10.1038/s41586-019-1136-0)
- Siegel, D. M., & Metzger, B. D. 2017, *PhRvL*, 119, 231102, doi: [10/gcpc2p](https://doi.org/10/gcpc2p)
- Siegel, D. M., & Metzger, B. D. 2018, *The Astrophysical Journal*, 858, 52, doi: [10/ggh94g5](https://doi.org/10/ggh94g5)

- Simon, J. D., Brown, T. M., Mutlu-Pakdil, B., & et al. 2023, *ApJ*, 944, 43, doi: [10.3847/1538-4357/aca9d1](https://doi.org/10.3847/1538-4357/aca9d1)
- Skúladóttir, Á., Hansen, C. J., Salvadori, S., & et al. 2019, *A&A*, 631, A171, doi: [10.1051/0004-6361/201936125](https://doi.org/10.1051/0004-6361/201936125)
- Sneppen, A., Watson, D., Damgaard, R., & et al. 2024, *Astronomy & Astrophysics*, doi: [10.1051/0004-6361/202450317](https://doi.org/10.1051/0004-6361/202450317)
- Suwa, Y., & Ioka, K. 2010, *ApJ*, 726, 107, doi: [10.1088/0004-637X/726/2/107](https://doi.org/10.1088/0004-637X/726/2/107)
- Tanaka, M., & Hotokezaka, K. 2013, *ApJ*, 775, 113, doi: [10.1088/0004-637X/775/2/113](https://doi.org/10.1088/0004-637X/775/2/113)
- Tanvir, N. R., Levan, A. J., Fruchter, A. S., & et al. 2013, *Nature*, 500, 547, doi: [10.1038/nature12505](https://doi.org/10.1038/nature12505)
- The HDF Group. 2025, Hierarchical Data Format, Version 5,
- The LIGO Scientific Collaboration, the Virgo Collaboration, & the KAGRA Collaboration. 2025, arXiv:2507.08219, doi: [10.48550/arXiv.2507.08219](https://doi.org/10.48550/arXiv.2507.08219)
- Thielemann, F.-K., Wehmeyer, B., & Wu, M.-R. 2020, *Journal of Physics: Conference Series*, 1668, 012044, doi: [10.1088/1742-6596/1668/1/012044](https://doi.org/10.1088/1742-6596/1668/1/012044)
- Thompson, T. A., Chang, P., & Quataert, E. 2004, *ApJ*, 611, 380, doi: [10.1086/421969](https://doi.org/10.1086/421969)
- Toomre, A. 1964, *ApJ*, 139, 1217, doi: [10.1086/147861](https://doi.org/10.1086/147861)
- Tsujimoto, T., Matsuno, T., Aoki, W., & et al. 2017, *ApJL*, 850, L12, doi: [10.3847/2041-8213/aa9886](https://doi.org/10.3847/2041-8213/aa9886)
- Umeda, H., & Nomoto, K. 2002, *ApJ*, 565, 385, doi: [10.1086/323946](https://doi.org/10.1086/323946)
- van de Voort, F., Pakmor, R., Grand, R. J. J., & et al. 2020, *MNRAS*, 494, 4867, doi: [10.1093/mnras/staa754](https://doi.org/10.1093/mnras/staa754)
- Virtanen, P., Gommers, R., Oliphant, T. E., & et al. 2020, *Nature Methods*, 17, 261, doi: [10.1038/s41592-019-0686-2](https://doi.org/10.1038/s41592-019-0686-2)
- Wallner, A., Faestermann, T., Feige, J., & et al. 2015, *Nature Communications*, 6, 5956, doi: [10.1038/ncomms6956](https://doi.org/10.1038/ncomms6956)
- Wanajo, S. 2006, *The Astrophysical Journal*, 647, 1323, doi: [10.1086/505483](https://doi.org/10.1086/505483)
- Watson, D., Hansen, C. J., Selsing, J., & et al. 2019, *Nature*, 574, 497, doi: [10.1038/s41586-019-1676-3](https://doi.org/10.1038/s41586-019-1676-3)
- Wehmeyer, B., Pignatari, M., & Thielemann, F.-K. 2015, *MNRAS*, 452, 1970, doi: [10.1093/mnras/stv1352](https://doi.org/10.1093/mnras/stv1352)
- Williams, M. A., Kennea, J. A., Dichiaro, S., & et al. 2023, *ApJL*, 946, L24, doi: [10.3847/2041-8213/acbcd1](https://doi.org/10.3847/2041-8213/acbcd1)
- Winteler, C., Käppeli, R., Perego, A., & et al. 2012, *ApJL*, 750, L22, doi: [10.1088/2041-8205/750/1/L22](https://doi.org/10.1088/2041-8205/750/1/L22)
- Woosley, S. E. 1993, *ApJ*, 405, 273, doi: [10.1086/172359](https://doi.org/10.1086/172359)
- Woosley, S. E., & Bloom, J. S. 2006, *ARA&A*, 44, 507, doi: [10.1146/annurev.astro.43.072103.150558](https://doi.org/10.1146/annurev.astro.43.072103.150558)
- Woosley, S. E., & Heger, A. 2021, arXiv:2103.07933, <https://arxiv.org/abs/2103.07933>
- Woosley, S. E., Heger, A., & Weaver, T. A. 2002, *Reviews of Modern Physics*, 74, 1015, doi: [10.1103/RevModPhys.74.1015](https://doi.org/10.1103/RevModPhys.74.1015)
- Woosley, S. E., & Zhang, W. 2007, *Royal Society of London Philosophical Transactions Series A*, 365, 1129, doi: [10.1098/rsta.2006.1997](https://doi.org/10.1098/rsta.2006.1997)
- Yoon, S.-C., Kang, J., & Kozyreva, A. 2015, *ApJ*, 802, 16, doi: [10.1088/0004-637X/802/1/16](https://doi.org/10.1088/0004-637X/802/1/16)
- Zenati, Y., Siegel, D. M., Metzger, B. D., & et al. 2020, *MNRAS*, 499, 4097, doi: [10.1093/mnras/staa3002](https://doi.org/10.1093/mnras/staa3002)
- Zevin, M., Kremer, K., Siegel, D. M., & et al. 2019, *ApJ*, 886, 4, doi: [10.3847/1538-4357/ab498b](https://doi.org/10.3847/1538-4357/ab498b)